Hybrid Organic/Quantum Dot Thin Film Structures and Devices

By

Seth Coe-Sullivan

M.S. in Electrical Engineering and Computer Science
Massachusetts Institute of Technology, 2002

Sc.B. in Electrical Engineering
Brown University, 1999

Submitted to the Department of Electrical Engineering
and Computer Science in Partial Fulfillment
of the requirements for the Degree of
Ph.D. in Electrical Engineering and Computer Science

at the

Massachusetts Institute of Technology
June, 2005

Signature of Author .....
Department of Electrical Engineering and Computer Science
April 29, 2005

Certified by .....
Vladimir Bulović
Associate Professor of Electrical Engineering and Computer Science
Thesis Supervisor

Certified by ....
Terry Orlando
Professor of Electrical Engineering and Computer Science
Thesis Supervisor

Accepted by .....
Arthur C. Smith
Chairman, Department Committee on Graduate Students

Hybrid Organic/Quantum Dot Thin Film Structures and Devices

By

Seth Coe-Sullivan

Submitted to the Department of Electrical Engineering
and Computer Science on April 29, 2005 in
Partial Fulfillmentof the requirements for the Degree of
Ph.D. in Electrical Engineering and Computer Science

ABSTRACT

Organic light emitting diodes have undergone rapid advancement over the course of the past decade. Similarly, quantum dot synthesis has progressed to the point that room temperature highly efficient photoluminescence can be realized. It is the purpose of this work to utilize the beneficial properties of these two material sets in a robust light emitting device. New deposition techniques are necessary to the realization of this goal, enabling QD organic hybrids to be created in a quick and reliable manner compatible with known device fabrication methods. With these techniques, quantum dot light emitting devices are fabricated, measured, and analyzed. The devices are of high efficiency and color saturation, and provide us with a test bed for understanding the interactions between inorganic QDs and organic thin films.

Thesis Supervisor: Vladimir Bulović
Title: Associate Professor of Electrical Engineering and Computer Science

Thesis Supervisor: Terry Orlando
Title: Professor of Electrical Engineering and Computer Science

Acknowledgments

I would like to thank: Vladimir Bulović for being who he is. Over five years together he has been my advisor and boss, mentor, teacher, advocate, co-founder, and friend. From him I have learned much about being a good scientist, and more about being a good person. I leave MIT happy, knowing that we will continue to work together after I leave.

Moungi Bawendi for his wisdom and support, and for always being right.

Wing Woo for getting us started, his excellence and attitude, forgiveness and friendship.

Jonathan Steckel for his chemistry brilliance, approach to life, and universal optimism. Of all the collaborations I've had in life, ours was the most productive, balanced, mutually beneficial, and fun.

LeeAnn Kim and Polina Anikeeva for being incredibly productive in a short time in lab, and for allowing me to utilize their most recent results in this thesis.

Conor Madigan, Ryan Tabone, Alexi Arango, David Oertel, John Halpert, Jean-Michel Caruge, Debbie Mascaro and John Kymissis who all played an active role in helping with this work, whether in experiment, analysis, or advice.

Yaakov Tischler for his co-narration of the grad school experience. Our talks always left me with a smile and a better understanding of who I am.

The entire Bulović and Bawendi Groups for their help in keeping the lab up and running, and for putting up with all of my habits and flaws.

My Mom and Dad for their constant, unconditional, and unquestioning support of all of my endeavors, even when they are incomprehensible. For enabling me to get to where I am today, and allowing me to be who I am, I am forever grateful and indebted to you.

My grandpa for always making sure I would "keep up the good work."

And finally, this thesis is dedicated to my beloved Emily, for without her it would not exist. I have depended on her love, support, guidance, inspiration, wisdom, and pep talks on a daily basis for 5 years. We met only months before I started at MIT, and she has comforted me through every failure and celebrated each success. I love her one million bajillion, and more so every day.

Biographical Note

Seth Coe-Sullivan graduated with honors from the class of 1999 at Brown University with an Sc.B. in electrical engineering. He was awarded top student honors within his electrical engineering class, and was selected for both the Sigma Xi and Tau Beta Pi honor societies. His research while at Brown focused on both computer vision algorithms for recognizing shape from shading, and the use of whispering gallery modes to generate single mode lasing in organic dye/ polymer systems. He then spent a year as a Staff Engineer at the Boston based research company Foster-Miller, Inc., in the Emerging Technology division of the Materials Technology Group before starting at MIT.

Seth will receive his Electrical Engineering Ph.D. from the Massachusetts Institute of Technology in June 2005 and completed an M.S. in Electrical Engineering as of June, 2002. Seth's research has focused on incorporating Quantum Dots into hybrid organic/inorganic LEDs. This has led to work on new fabrication techniques, and the design of a completely integrated thin film deposition system. He won the Materials Research Society gold medal Graduate Student Award as well as the Best Poster Award in Spring of 2003. Seth is also the 2004 Winner of the Nikon Small World Microphotography Contest. His work has been published in various peer reviewed journals, has led to multiple patent applications and has been the subject of presentations at MRS, SPIE, and SID conferences.

Table of Contents

List of Figures

List of Tables

1 Introduction

1.1 Thesis Overview

In this chapter, the history of light emitters and their applications is reviewed in order to motivate the creation of quantum dot based light emitters. This includes a synopsis of organic light emitting device structures and operation, description of quantum dots as a novel material, and the pre-existing deposition techniques available for both of these material sets. Chapter 2 outlines the structure of our integrated materials growth system which enabled the fabrication of hybrid devices of these two materials. Chapter 3 discusses the design of quantum dot light emitting devices (QD-LEDs). Chapters 4 and 5 then discuss two new fabrication methods that were invented in order to realize these device designs. Chapter 6 analyzes the resulting device performance and investigates the physical processes underlying QD-LED operation. The final sections of the thesis analyze the commercialization potential of QD-LED technology, discuss future avenues of research and the new opportunities stemming from the projected developments.

1.2 Pre-history of the light emitting device

Light emitting devices have existed in one form or another since the year 1800 when Humphry Davy experimented with electric batteries, some wire, and a piece of carbon[1]. Over the next 110 years, what eventually became known as the incandescent light bulb was improved upon until it was in a form much like the light bulbs we still use today. It was this basic invention that converted lighting from a chemoluminescent based approach, *i.e.* chemical energy in → light out, such as candles, to an optoelectronic approach, *i.e.* electrical energy in → light out. The implications of this paradigm shift were impossible to recognize at the time, and are largely taken for granted today. The

indoor light bulb was the 'killer app' that drove the distribution of electrical power into every home in the developed world (one could argue that a 'developed country' is defined by the presence of distributed electrical power) in much the same way that email drove the distribution of the internet into our homes. Light bulbs, and by extension light emitting devices, have played a critical role in defining the world's technologies and economies. Figure 1-1 shows artificial lighting as imaged from space, demonstrating the connections between lighting and human population.

Figure 1-1: Satellite photography of the world during nighttime hours. Bright spots indicate the prevalent use of artificial lighting.

Since 1910, the development of new light emitting device technologies resulted in the advent of fluorescent lighting, inorganic semiconductor light emitting diodes, and most recently organic light emitting devices[2]. Overall, generation of light is estimated to consume between 20 and 30% of the world's electrical power, emphasizing the large positive impact the development of new and efficient light sources could have. What was a "killer app" in 1900 remains one to this day. Remarkably, the incandescent light bulb, modified in only small ways since the year 1800, is still the dominant lighting technology in indoor, residential lighting applications due to its color quality. Tailoring the emission

spectrum to match that of a black body emitter has been the dominant challenge of the emerging lighting technologies.

1.3 Applications of light emitting devices

General lighting is not the only application of light emitting devices. Television displays and indicator lights are also major applications which require an input of electrical energy to be converted into light output. While incandescent bulbs could meet the needs of indicator lighting, a different technology was required to produce a television screen, as a two-dimensional array of emitters is required. This array must be individually addressable, so that an image can be produced. The image dissector device, later renamed the iconoscope and eventually cathode ray tube (CRT) television, solved this problem[3]. By steering a single beam of electrons across a fluorescent surface faster than the human eye can perceive, a two-dimensional image is produced. Development of long-lasting, bright and efficient three color phosphors enabled the color television to become dominant in this application space.

Such CRT based TVs met the need of consumers for generations, and it was not until the advent of personal computers that there was any real need to develop an alternate technology. Computer display monitors initially had very similar specification requirements to TVs, and as such CRTs were the dominant technology for this new application as well. However, as the semiconductor industry made computers that were more and more powerful in smaller and smaller packages, the idea of a portable computer became viable. Soon it was the CRT monitor that was the most cumbersome portion of a computer, both in volume and weight. Logic devices and information storage had moved from discrete filamentary devices (vacuum tubes) to integrated solid state devices with

the advent of solid state semiconductors. A similar step was desirable in the realm of display technology, consumers now demanded a technology to enable the creation of flat panel displays, or FPDs.

1.4 Liquid Crystal Displays

Since the 1970's the dominant FPD technology has been liquid crystal displays (LCDs). This thin film device functions as a voltage driven light valve, allowing light to pass or not depending on the voltage applied across the cell. The light itself is produced by what is essentially a fluorescent light bulb. For the past 20-30 years, LCD technology continues to improve, driven by a strong consumer demand for such portable displays. While other technologies have been promised, few have succeeded in competing with LCDs in the open market. Today, the FPD industry has a market size of roughly $35B, and LCDs account for 87% of this total revenue. Other technologies such as plasma, organic light emitting devices (OLEDs), and vacuum fluorescence comprise the rest of the market.

Liquid crystalline materials were first discovered in 1888, by Austrian botanist Friedrich Reinitzer[4]. Reinitzer observed that when he melted a particular cholesterol-like substance (cholesteryl benzoate), it first became a cloudy liquid and then cleared up as its temperature rose. Eighty years passed before RCA made the first experimental LCD in 1968. Since then, LCD researchers have steadily developed ingenious variations and improvements on the technology, taking the LCD to amazing levels of technical complexity and performance.

Liquid crystals occupy a state that is between that of a crystalline solid and an isotropic liquid. They exhibit fluidity, but maintain a high degree of order. This

intermediate phase is called a mesophase, and compounds that exhibit this phase are called mesogens. Being fluid, LCs change their shape in response to an electric or magnetic field.[5] LC molecules can also be designed to have a large anisotropy in their permittivity. The collective order of these molecules with high anisotropy gives rise to rotations in the polarization of light passing through a cell of LC. This controlled rotation is switched on and off by application of electric field across the LC cell, and since the cell is sandwiched between polarizers, only one of these two states is light conducting, i.e. 'on', the other being light absorbing 'off'. Any transmitted light then passes through the color filter array, creating the sub-pixilation required for a full three color display technology. Clearly, spectrally broad band filters have higher throughput of light, but this is traded off against the resulting reduction in color saturation.

A cross section of a typical LCD cell is shown in Figure 1-2.

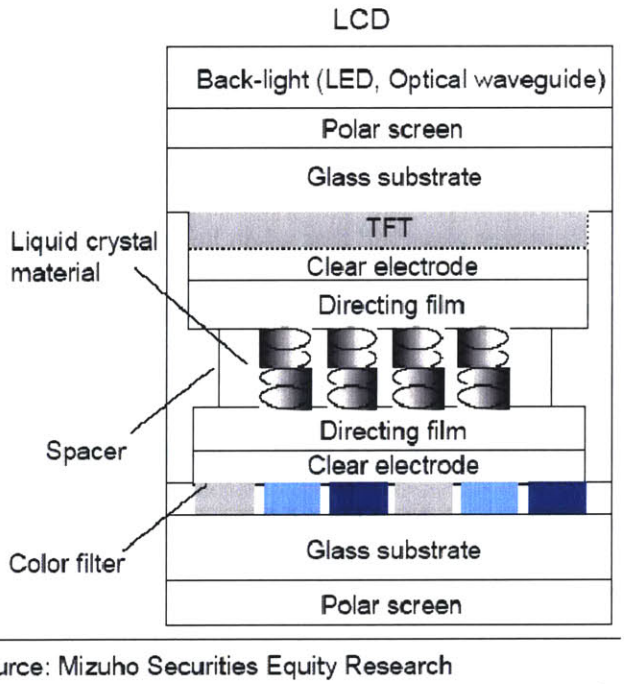

Source: Mizuho Securities Equity Research

Figure 1-2: Cross-section of a typical liquid crystal flat panel display. Light is generated by the back light unit (which is usually cold cathode fluorescence based) and is polarized before passing into the optical switching (liquid crystal) cell itself. The liquid crystal is oriented by two directing films (rubbed polymer layers), and then any transmitted light is partially absorbed by the color filter layer to allow for the definition of sub-pixels (red, green, blue).

1.5 Inorganic light emitting diodes

Inorganic light emitting diodes or (ILEDs) are also an important background technology to this work, because of their use in numerous applications. ILEDs are devices fabricated by epitaxially growing single crystals of inorganic semiconductors on top of a lattice matched crystal. Because of the material perfection inherent to these high purity, single crystal structures, they are highly stable structures capable of very high performance: ILEDs can be extremely bright, efficient, and stable emitters of light at many wavelengths of interest. However, ILEDs have been limited to point source applications due to the cost of producing such emitters. (An exception to this is extremely large area billboard displays, where it becomes cost effective to have >10m long arrays of ILEDs packaged adjacent to each other.) Indicator lights, backlights for small area LCD FPDs, and in the near future general lighting are all applications where ILEDs are useful.

The simplest structure of an ILED is a p-n diode of direct band gap II-VI and III-V inorganic semiconductors such as CdSe, and GaAs respectively. The p-type material is a crystalline inorganic semiconductor that is doped to have a high concentration of positive mobile charge carriers, while the n-type material has excess negative charge carriers. Under forward bias these free charge carriers undergo a net motion due to both drift and diffusion. Motion of electrons in a periodic lattice is a well understood phenomenon that we will not detail here. The result is that some minority charge carriers are injected into the region of the crystal where there is an excess of majority charge carriers, giving rise to a probability that the two charge carriers will recombine, resulting in the emission of light[6]. The light emitted will be at the energy of the band gap of the material, and thus tertiary and quarternary semiconductors can be used to gain access to a wider range of

emission wavelengths. However, the need to grow epitaxial layers does limit the range of semiconductor combinations that are compatible with each other. For most relevant inorganic semiconductors, the binding force between the electron and hole is lower in energy than k_BT at room temperature, and thus the concept of the e-h pair first forming an exciton before recombining is not operative. This is an important distinction between the radiation processes of bulk inorganic semiconductors and that of quantum dots and organic semiconductors.

1.6 Organic light emitting devices

In 1987, both ILEDs and LCDs were far less sophisticated then they are today. It was still unclear to what extent their cost could be driven down, and their performance improved. At this time, researchers at Kodak released papers on both light emitting devices[2] and solar cells[7] utilizing amorphous films of organic small molecules. The potential of this technology was apparent– the performance of these initial devices was high (close to 1% LED external quantum efficiency, and 1% solar cell external power conversion efficiency), and the materials did not require the expensive growth techniques inherent to any crystalline material set.

Since these initial works, much work has focused on the use of organic materials for optoelectronic applications. Optically pumped lasers[8] and efficient photodetectors[9] have been created, and OLEDs can now be realized in their transparent[10], flexible[11], metal-free[12], or phosphorescent[13] forms. Parallel work on polymeric materials[14] has led to similar performance of polymer OLEDs. The research efforts have been devoted to enhancing the performance of OLEDs[15] by increasing their efficiency[16-18] narrowing[19] or broadening[20] their emission spectra, polarizing their emission[21],

increasing the device lifetime[22, 23], lowering operating voltages[24, 25], understanding the basic physics of how they operate[26], and developing new means of depositing[27-29] and patterning[30] these novel materials.

Concurrently with all of these research advances, organic materials have also been introduced into the commercial sector. OLED displays are available on commercial cell phones, car stereos, digital cameras, and PDAs[31]. Full color flat panel polymeric OLED displays with an up to 40" diagonal have been demonstrated, though they are not yet available for commercial consumption. It is clear that commercial organic optoelectronics will be widespread in just a few years time. While these initial commercial displays have external quantum efficiencies (EQE) of near 1%, laboratory pixels have been demonstrates with EQE of ~20% corresponding to an internal quantum efficiency of ~100%[13]. Table 1-1 compares the operational performance of OLED displays to those of LCDs.

	Organic EL Low molecular	Organic EL High molecular	LCD CGS	LCD Low-temperature polysilicon	LCD Amorphous	LCD STN	LCD FS
	2 inch	2 inch	2 inch	2 inch	2 inch	2 inch	2 inch
Brightness	Good	Good	Very good	Very good	Very good	Good	Very good
(cd/m^2)	100	120	150	150	150	100	150
Contrast	Very good	Very good	Good	Good	Good	Average	Good
	500:1	500:1	300:1	300:1	300:1	30:1	150:1
High- definition	Good	Average	Very good	Very good	Average	Poor	Very good
	QVGA	QCIF	QVGA VGA	QVGA -VGA	QCIF		QCIF
(ppi)	180	130	200 -300	200 -300	200	180	150
Color reproducibility	Good	Uncertain	Average	Average	Average	Poor	Very good
(%)	60-70		30-40	30-40	30-40	20-30	90-100
Response speed	Very good	Very good	Good	Good	Good	Poor	Good
(ms)	<0.01	<0.01	20-25	20-25	20-25	100-200	0.3-13.5
Thickness	Very good	Very good	Good	Good	Good	Poor	Good
(mm)	1.5-2.0	1.5-2.0	3.0-3.5	3.0-3.5	4.0-5.0	3.5-5.0	3.0-4.0
Power consumption	Average	Very good	Average	Average	Good	Good	Good
(mW)	270	150	250	250	180	180	180
Life	Average	Poor	Very good	Very good	Very good	Very good	Very good
(hr)	8,000	1,000	50,000	50,000	50,000	50,000	50,000

Source: Mizuho Securities Equity Research

Table 1-1: Comparison of specifications of OLED and LCD 2" displays.

1.6.1 Challenges of OLED technology

It has become clear in recent years of OLED development that there are several basic physical problems that will continue to be difficult to overcome with any organic material. Most prominent is the relatively short operating lifetime of most organic electroluminescent (EL) devices. Lifetimes have been extended using new chemistry to prevent crystallization, and more sophisticated packaging schemes[32] to prevent water and oxygen from degrading the emitting molecules. Such techniques have extended the lifetimes of small area commercial displays into the range of 10,000 hours[31]. However, the packaging methods are difficult to extend to flexible substrates, and the chemistry optimization must be repeated with each new emitter (minimum of three for a full color display) that goes into the device. In addition, the packaging schemes and complex syntheses are expensive, and mitigate some of the inherent advantages that OLEDs were predicted to achieve.

Such constraints have delayed the development of high efficiency blue and red OLEDs that have lifetimes long enough to make large area commercial displays. Human perception of luminous intensity peaks sharply in the green (Figure 1-3), making blue and red devices much more difficult to create at the same efficiency. In addition, broadband blue emitting devices will either look green-blue to the human eye, or emit a large amount of UV light, which we cannot perceive at all. Thus, creation of efficient emitters at the visible spectrum's extremes requires a narrowband source. Organic molecules tend to have steric flexibility (in contrast to a covalently bonded inorganic crystalline semiconductor), which functions to broaden the characteristic emission of an amorphous solid relative to a crystal (using organic crystals is an alternative approach, to date limited by deposition techniques as well as the low emission efficiency of most organic

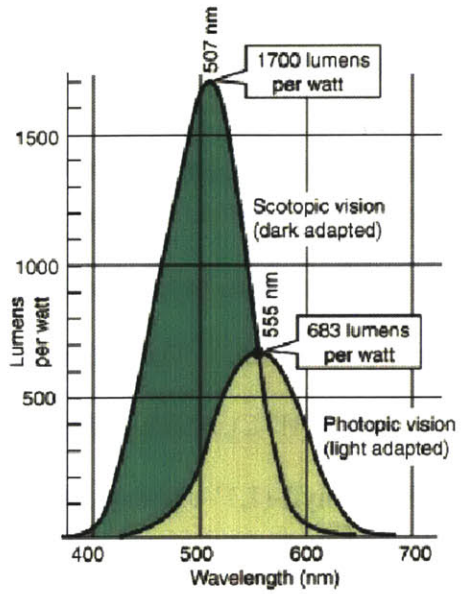

Figure 1-3: Plot showing the human eye's ability to perceive light intensity at various visible wavelengths. Shown are both the photopic (daylight) and scotopic (low light) responses. The photopic response is peaked at 555nm light, which is why green emitters of equal power output (to red, blue) are perceived as brighter by human viewers.

crystals [33]). While attempts have been made to use chemistry to "bridge" some of these steric freedoms, and hence create more rigid, narrowband emitters, the attempts have met with only limited success[34]. The problem is fundamental to the material set, and hence we must look to other materials to find solutions.

A final problem that is unsolved in the industry is how to laterally pattern red, green and blue materials on a substrate to create full color displays in a truly manufacturable process. Lithographic processes which are well developed in the semiconductor electronics world are not compatible with OLED materials, due to the similarities between the organic photoresist materials and the organic emissive layers themselves. OLEDs cannot survive the photoresist spin, bake, develop and strip cycles that are used to laterally pattern features on Silicon wafers. Thus new techniques must be developed, and to date none have been proven effective for the large areas and high throughputs demanded by the FPD industry. One patterned deposition process that does

have promise is inkjet printing of organic materials directly onto the display backplane – which has led to Epson's demonstration of a 40" full color polymer OLED display.

1.6.2 OLED Device Structure and Operating Principles

Due to the similarity between OLED device structure and that of QD-LEDs, a brief overview of OLED devices and the physics behind how they work are necessary. Figure 1-4 shows a typical heterostructure OLED. The indium tin oxide (ITO) anode injects holes into the hole transport layer (HTL), which in this case in the small molecule N, N'-diphenyl-N, N'-bis (3-methylphenyl)-(1,1'-biphenyl)-4,4'-diamine (TPD). Holes are transported via hopping transport within the TPD until they reach the tris-(8-hydroxyquinoline) aluminum (Alq_3) interface, where they buildup at the band edge mismatch.

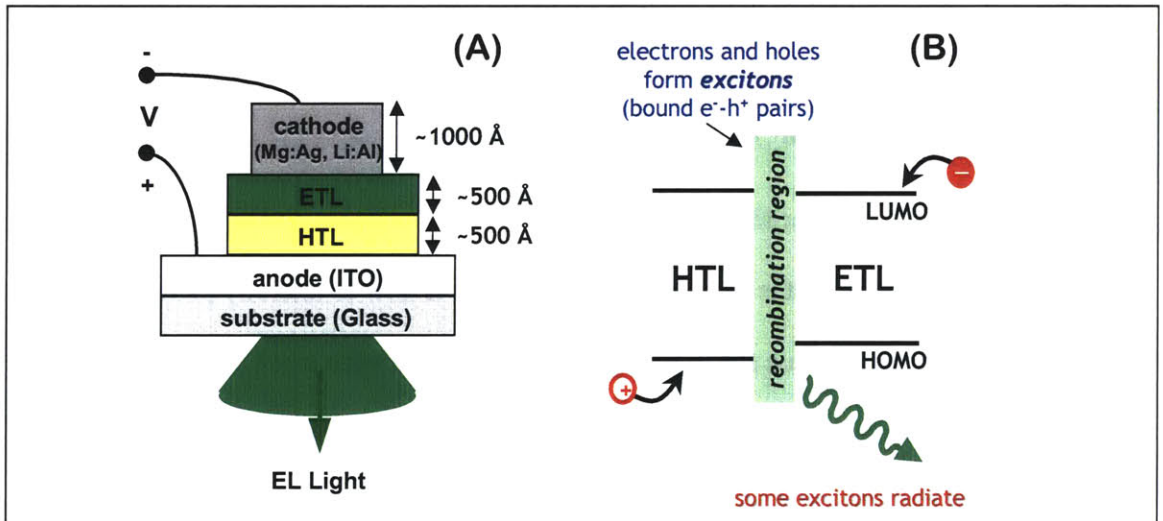

Figure 1-4: (A) Basic OLED structure. A glass substrate is coated with a thin film (150nm) of the transparent inorganic conductor indium tin oxide (ITO). This is then coated with ~50nm of a hole transporting amorphous organic semiconductor layer (HTL) and electron transport layer (ETL), followed by a metallic conductor cathode such as magnesium, calcium or aluminum. (B) Principle of operation of a typical OLED. Electrons and holes in their respective transport layers travel towards the recombination region at the interface between the two films. In this region, an electron and hole may occupy the same molecule (becomes an exciton). This exciton may then recombine radiatively, created a photon of light at the characteristic wavelength of that molecule.

Simultaneously, electrons are being injected into the Alq_3 from the cathode which is a low work function metal, such as Mg:Ag or Li:Al alloys. These electrons are transported through the Alq_3 to the same heterojunction, where they also accumulate. Statistically, a fraction of the built-up holes or electrons can cross the heterojunction interface leading to the creation of tightly bound electron-hole pairs on individual molecules of either TPD or Alq_3. These tightly bound e-h pairs are referred to as excitons, and may be thought of as single particles. They can relax either radiatively, emitting light characteristic of the optical bandgap of whichever material that they were residing on, or non-radiatively, losing the energy to phonons or heat. Prior to relaxation, excitons may diffuse from molecule to molecule via energy transfer processes. In this TPD/Alq_3 device, all of the excitons will transfer their energy to the Alq_3 molecules prior to relaxing, and hence no TPD emission will be observed. Such a device may have an external quantum efficiency as high as $\eta_{ex} = 1\%$, which is to say that for every 100 electrons injected into the device, one photon may be observed by a detector external to the device. η_{ex} is the product of several factors that are determined by the materials, and optical and electrical properties of the device. This product may be written as $\eta_{ex} = \chi \cdot \eta_{PL} \cdot \eta_r \cdot \eta_e$ where χ is the fraction of charge carrier recombinations resulting in singlet excitons, η_{PL} is the photoluminescence efficiency of the material in the solid state, η_r is the fraction of injected electrons that form excitons, and η_e is the fraction of emitted photons that are coupled out of the device[13]. For a typical Alq_3 device, $\chi \sim 1/4$, $\eta_e \sim 1/5$, and $\eta_{PL} \sim 0.40$, resulting in a theoretical maximum η_{ex} of 2%.

To improve the LED luminescence efficiency, the exciton-generating region is often doped with dyes of high PL quantum efficiency[35]. The host excitons can then

transfer their energy to luminescent dopants via either Förster or Dexter energy transfer. Similarly, the energy level structure of the dopant might render it an electron or a hole trap for mobile carriers, which can also lead to exciton formation directly on the dopant in a process known as direct carrier injection. Even small doping concentrations (from a fraction of a percent to a few percent) in the electrically pumped host layer are sufficient to change the luminescence spectra, often completely quenching the host luminescence. Low dopant concentration implies a large average distance between these molecules, which reduces exciton quenching from dopant-dopant interactions and yields highly efficient luminescence. The lifetime and efficiency of doped OLEDs have been found to depend on the nature and concentration of dopant molecules in the light emitting layer[36]. Figure 1-5 shows some examples of doped Alq_3 OLEDs. For comparison, the luminescence spectrum of undoped Alq_3 is also shown. Förster energy transfer in Alq_3:(2%) DCM2 ([2-methyl-6-[2-(2,3,6,7-tetrahydro-1H, 5H-benzo [ij] quinolizin-9-yl) ethenyl]-4H-pyran-4-ylidene]propane-dinitrile) OLEDs leads to orange EL with forward external emission efficiency of $\eta_{ex}^{(forward)} \sim 0.5\%$ photons per injected carrier[35, 37]. Dexter energy transfer in Alq_3:(6%) PtOEP (2,3,7,8,12,13,17,18-octaethyl-21H,23H-porphine platinum (II)) OLEDs leads to highly efficient, $\eta_{ex}^{(forward)} \sim 4\%$, saturated red phosphorescence[13]. In these doped OLEDs, different molecules perform the functions of electron/hole transport, and of the luminescent center. Such separation of functionality allows for optimization of device performance.

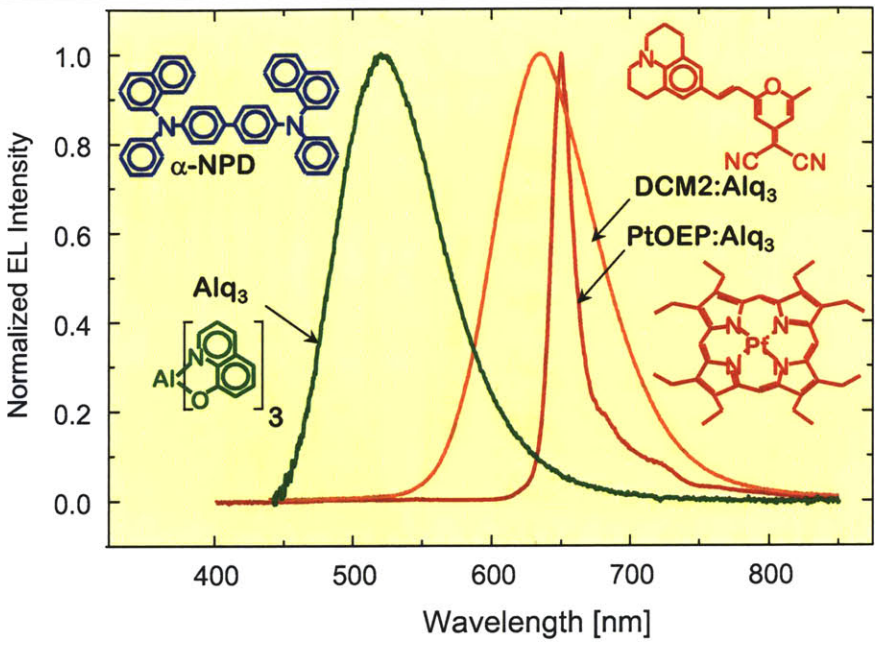

Figure 1-5: Electroluminescence of Alq3 electron transport layer, and Alq3 doped with fluorescent DCM2 and phosphorescent PtOEP. Chemical formula for α-NPD hole transport layer is also shown.

From the narrow and tunable emission spectra of inorganic QDs (Figure 1-6) it is apparent that the QDs could be well suited as luminescent dopants in organic host materials. Their photoluminescence efficiency is comparable to the best of organic lumophores, while the spectral emission width is less than half of the typical organic emitters, resulting in more saturated colors. CdSe QD absorption and emission can be tuned across most of the visible spectrum by changing the dot diameter from 17 to 120Å (see Figure 1-6). Such wide tunability by size selection greatly simplifies optimization of QD-LED color emission (an advantage not easily achievable with organic lumophores).

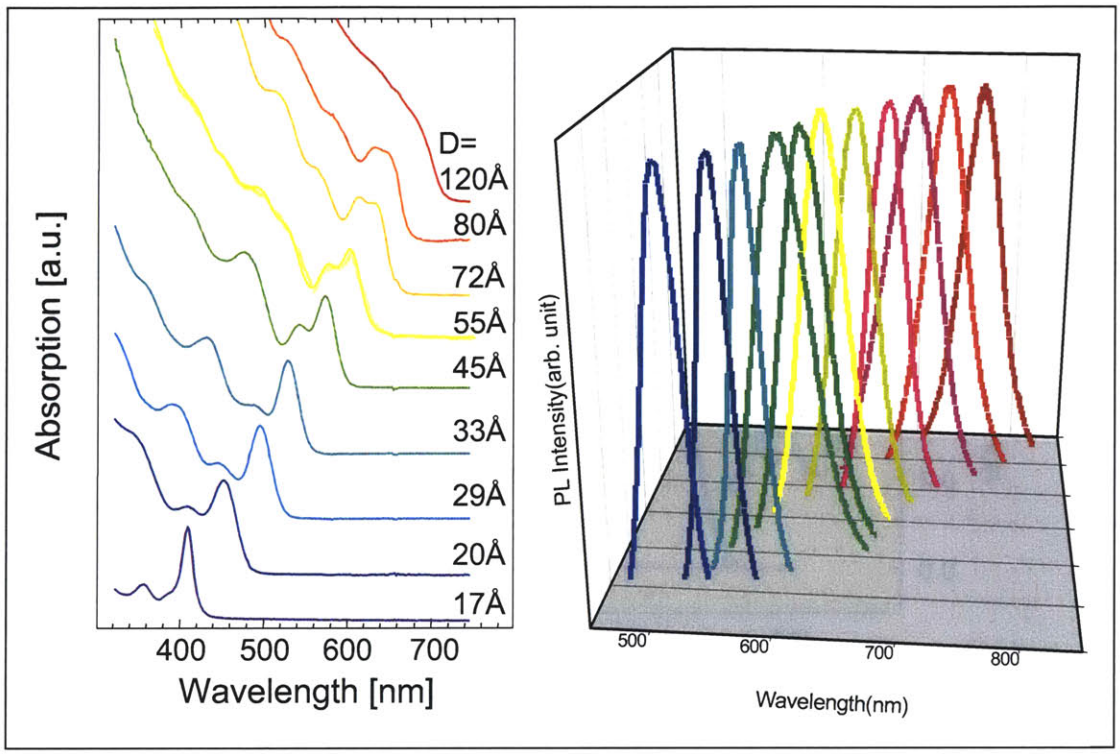

Figure 1-6: Absorption and emission spectra of CdSe quantum dots. Their ability to be continuously tuned throughout the visible (or infrared) region of the spectrum is unmatched by any class of organic lumophores.

1.6.3 OLED Deposition and Patterning Methods

Deposition techniques that have been employed in the successful fabrication of laboratory scale OLEDs may be classified as either wet or dry techniques. The use of wet techniques such as spin-casting and ink jet printing are largely confined to polymeric organics, where typical dry techniques such as vacuum thermal evaporation are not viable. This is due to the large molecular weight of polymeric materials, which causes their evaporation temperature to be far in excess of their decomposition temperature.

Spin-casting is a fast and easy deposition technique, depicted in Figure 1-7, in which a quantity of solid (usually polymer) is dissolved into an organic solvent. This solution is placed onto a substrate, allowed to wet the entire area to be coated, and then

set spinning at high speeds (1,000-10,000 rpm is typical). The majority of the solution is expelled due to the centrifugal force of the spinning, however, a fraction of the solution is left behind. The exact thickness of this liquid film is difficult to predict, but is controlled by a combination of adhesion forces at the substrate/liquid interface, solution viscosity, and friction at the air/liquid interface. For a low vapor pressure solvent, this thin liquid film can exist indefinitely on the spinning substrate surface. However, for typical organic solvents used in spin coating, the vapor pressure is quite high, and the solvent begins to evaporate immediately upon exposure to any unsaturated environment. Thus, this thin liquid film eventually dries (time scales are typically 1-60s), leaving behind an even thinner (1-1000nm), flat solid film of the initial solvated solid. It is important to note that while the spin-casting technique is a fast and easy method of preparing large area homogeneous films, it does not lend itself to patterned deposition. With inorganic semiconductors, photoresists are deposited by spin casting, and are subsequently patterned by UV exposure through a photomask. This photoresist is then used as a etch mask for the inorganic semiconductor to be patterned. This process does not map to organic semiconductors, or soluble materials in general, since it relies upon the solubility differences between the photoresist and the inorganic semiconductor to be patterned.

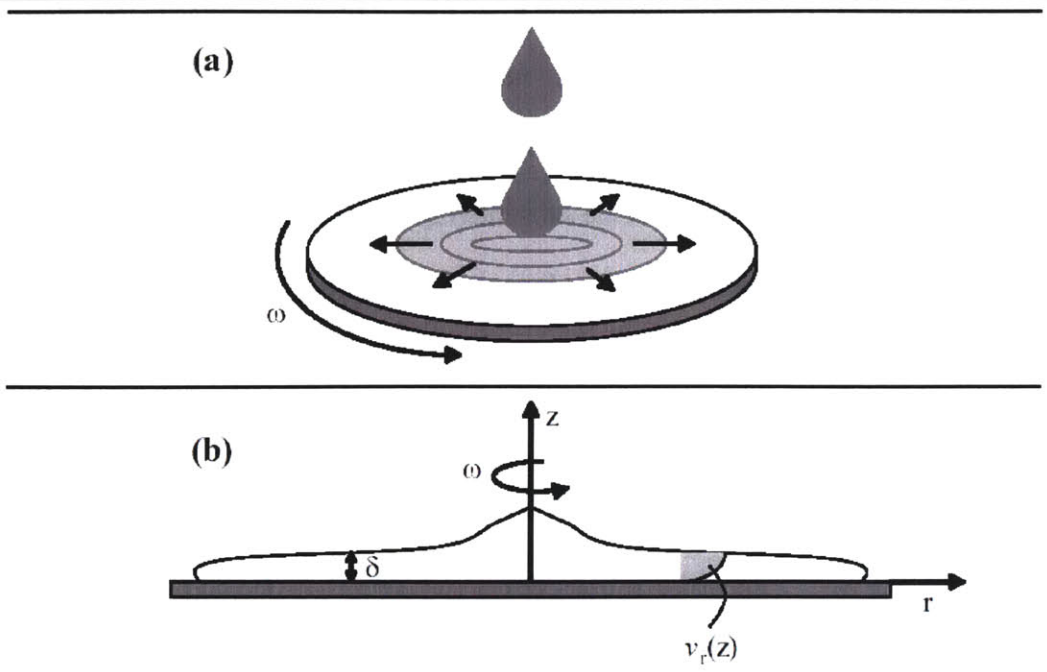

Figure 1-7: Coating of a substrate using spin-casting. A solution is dispensed onto a substrate, which rotates at an angular velocity ω = 1,000 – 10,000 rpm. Centrifugal forces spread the solution over the surface, as the solvent evaporates. Spin-casting is often followed by a bake step to drive off any residual solvent and further densify the coating. Better film thickness uniformity across the substrate is obtained for higher ω, but is typically limited to ±100Å.

Ink jet printing of organic materials again relies upon solvation of the material, but this solution is then expelled from a print head into very small (~20μm typically) droplets, which travel through air to reach a substrate roughly 100μm from the print head. Once the droplet reaches the substrate it begins to dry, and the material is deposited within the circumference of the droplet as it wets the surface. However, typically the deposited film is far from being uniform across the area of the deposition, but rather dries in a 'coffee stain' pattern. This is due to the convective processes that occur within the drying droplet, as well as material pinning effects which can occur at the circumference of the droplet. This film thickness non-uniformity gives rise to a dispersion of pixel operating voltages, and thus the appearance of bright spots in a display. Overcoming this

problem, as well as controlling the trajectory of the ejected droplet as it leaves the print head, has been the focus of academic researchers and industrial labs for a number of years. Ink jet printing has the advantage of being a patterned deposition technique, and hence is potentially a complete solution to the deposition of active layers within a display[38].

Dry techniques such as vacuum thermal evaporation (VTE) and organic vapor phase deposition (OVPD) have predominated small molecular organic material deposition. This is both because of the ease of depositing large area uniform and homogenous films using these dry techniques, and because the solubility of small aromatic molecules tends to be too small to allow for solution processing of sufficiently thick films.

Vacuum thermal evaporation (VTE) is the simplest vacuum deposition technique possible, as depicted in Figure 1-8. A boat made out of a resistive metal (typically tungsten, molybdenum, or tantalum) is heated by passage of electrical current. The boat contains organic material, which upon heating evaporates or sublimes. The evaporation takes place in a low pressure (typically 10^{-6} torr) vacuum chamber so that the evaporated material is unlikely to undergo any collisions along its path towards the substrate, and also to keep the deposited materials as pure as possible. Each molecule that is liberated from the solid has some initial speed and direction that is not changed until it contacts a substrate or chamber surface, which is typically cold enough to cause it to condense on contact. Because of the even distributions of the initial molecular trajectories, the resulting deposition is essentially of uniform thickness for any solid angle intersected by a substrate. To achieve uniform depositions over larger area substrates, longer boat-to-

substrate throw distances are used, or uniformity plates are inserted into the molecular beam path to even out non-uniformities. Substrates are also typically rotated to reduce non-uniformities in one direction. Using this technique, it is unavoidable that between 70-99% (depending on throw distance) of the material in the boat is deposited on the walls of the vacuum chamber, rather than the substrate. The materials utilization is traded off against film thickness uniformity.

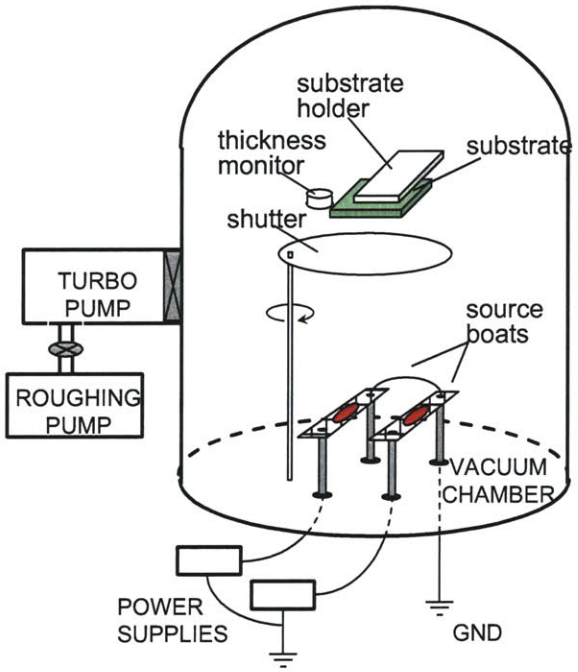

Figure 1-8: Cartoon depiction of thermal evaporator. Source boats are resistively heated until material begins to evaporate. Evaporated molecules travel unimpeded through vacuum until they collide with a solid surface (substrate or chamber walls), where they condense. A quartz crystal thickness monitor allows the user to shutter off the growth when the desired thickness is attained.

Materials deposited by VTE are most commonly patterned using shadow masking. Shadow masking allows for the patterning of a material by preventing deposition in the areas where it is not desired. Typically, a thin metal foil is used as a shadow mask, with a pattern of through holes across its surface. Material that reaches the shadow mask is

deposited onto the metal mask, and thus material reaches the substrate only in the area of the holes. This technique is simple and powerful, but has proved to be quite difficult to scale in manufacturing. Active matrix OLED displays have been built with dimensions up to 4" in diagonal using shadow masking, but it is considered unlikely that the technique can continue to scale to larger areas. For larger patterned substrates manufacturing yield is reduced, while the mechanical constraints complicate the large area scaling. Because shadow masking requires the deposition of material onto the metal of the mask itself, there is a build-up of material from run to run. This material is then a source of impurity and particulates in the chamber reducing yields of subsequent runs, and eventually requiring the masks to be cleaned. Both of these add to the cost of manufacture of the display. Additionally, to reduce the dust accumulation on the substrate the typical direction of VTE deposition is up, with the shadow mask held just below the substrate. Ideally, the mask would be a uniform distance from the substrate across the entire area to be masked – but due to gravity a warp in the mask develops. Suspending a large area mask below the substrate with some reasonable uniformity of separation requires applying tension to the metal foil. However, physical limits to how much tension can be applied to these thin, perforated foils limits the practical size of the shadow mask to less than 40 cm on a side, too small for profitable display manufacturing that benefits from larger glass sizes of up to 200 cm in today's Generation-7 LCD production. Finally, the material deposited on the shadow mask wastes material, further decreasing the material utilization rate, further increasing the cost to manufacture. This litany of drawbacks to the shadow masking technique has recently led even the

staunchest supporters of vacuum evaporation to hedge their bets and consider solution based approaches.

Organic vapor phase deposition (Figure 1-9) is another known technique for the dry deposition of organic materials[29]. It similarly relies upon the evaporation of small molecules from a solid in the presence of heat and vacuum. However, the pressures used are typically mtorr or even 10's of torr, and so the mean free path of the gas phase molecules are much shorter than the throw distances used. Also, a carrier gas is flowed over the evaporation source, and is used to move the material in a given direction. Finally, the chamber walls are kept at or above the evaporation temperature of the material being deposited, preventing material from being deposited on the chamber walls, resulting in a higher material utilization factor (typically 50%) than that of thermal evaporation. Using this technique, high levels of control can be attained, with excellent uniformity over large areas, despite much shorter throw distances. However, because of the higher pressures and shorter collision lengths inherent in the process, the pattern resolution that can be attained by shadow masking is more limited than in a VTE process.

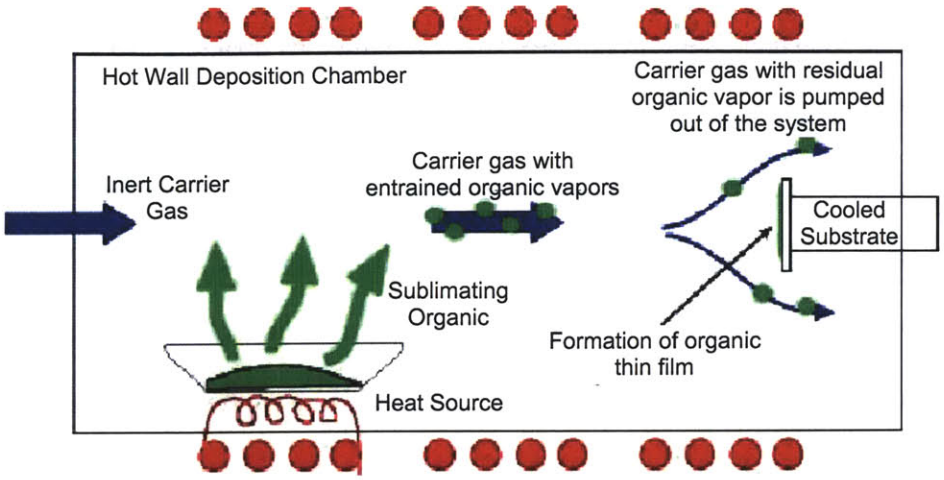

Figure 1-9: Schematic of Organic Vapor Phase Deposition (OVPD). A hot inert carrier gas such as Nitrogen transports organic vapors through a hot-wall reactor towards a cooled substrate, where the vapor selectively physisorbs. (Figure courtesy of Max Shtein.)

Either side in the academic debate between polymer and small molecule technologists claims to have both the superior material, and the ideal deposition technique. Researchers in polymer LEDs site the flexibility and diversity of polymer design, and the low cost of wet deposition techniques which do not require the use of vacuum equipment as advantages of their approach. Researchers pursuing the small molecule pathway refer to the higher purity of available materials, the reproducibility and thickness control of vacuum evaporation, and ultimately the higher performance metrics that have been achieved as the validation of their approach. What becomes important to our present work is that both sets of deposition techniques and materials are available to us for combining with the QD material set, and that we have the flexibility of pursuing whichever seems the most promising for our particular avenue of research.

1.7 Colloidal Nanocrystal Quantum Dots

A quantum dot can most generally be defined as a nanoscale material in all three dimensions such that its electronic structure is modified by quantum mechanical effects[39]. They are also frequently referred to as nanodots and nanocrystals. Quantum dots had been theoretically analyzed long before it was possible to physically make them with high degrees of reproducibility and uniformity. The advent of molecular beam epitaxy made it possible to form very thin layers of semiconductor materials known as quantum wells. These quantum wells are continuous films in two dimensions, and thin enough in the third dimension to result in quantum confinement. Differences in the electronic structure of quantum wells was studied both theoretically and physically, and led to the concept of quantum wires, and quantum dots. With each subsequent confined dimension, the density of allowed electronic states in these materials narrows, giving rise to narrower absorption and emission spectra, which we utilize in QD-LEDs (see Figure 1-10).

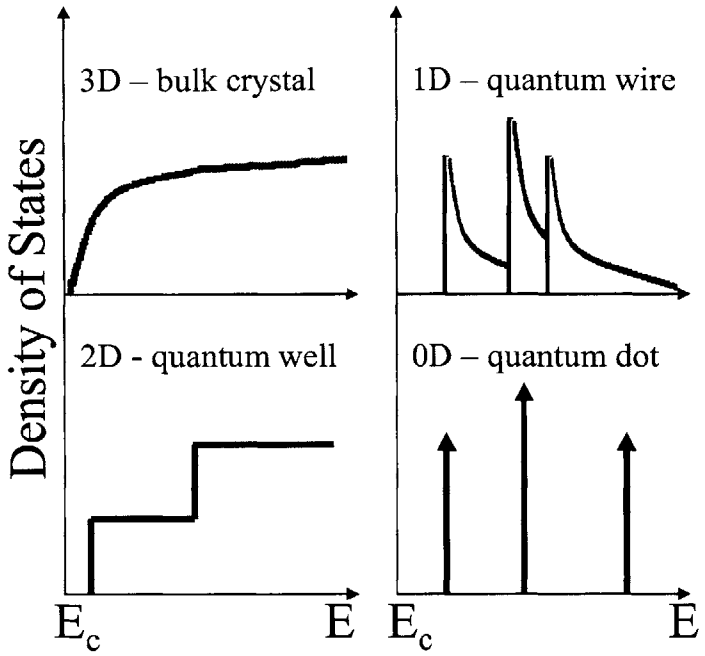

Figure 1-10: The density of states within a semiconductor just above the conduction band energy (E_C) shown for various degrees of quantum confinement. This particulat effect of quantum confinement is what gives rise to the narrow band emission that is possible to attain from a quantum dot.

However, while epitaxial techniques enabled the creation of small structures in one dimension, they did not provide a general method for creating confinement in the other two dimensions. It was demonstrated that quantum dots can be created through epitaxy by depositing very small quantities of material onto a substrate, with lattice mismatch between the two crystals causing strain which is reduced when the thin film breaks up into droplets. These droplets are typically extremely thin and of larger dimension in the plane of the layer. Additionally, it is challenging to have all of the droplets form into the same size, and hence the size distribution of these epitaxially grown quantum dots is broad, with the typical standard deviation of their size distribution exceeding 10% of the mean size.

The synthetic route of Murray *et al.* [40] departed from the more standard vacuum MBE growth of randomly arranged QDs on a crystalline substrate[41]. Instead, this new technique allowed for the growth of ensembles of crystals out of solution. This enhanced the level of control available in preparing the material, and simultaneously allowed the QDs to be handled as if they were organic "macromolecules" in solution, since they were grown with an organic capping layer already assembled on their surface. This new synthetic route made is possible to separate the formation of the nanoscale material from the deposition of the QDs onto a substrate. QDs prepared in this manner can have extremely narrow emission and absorption bands due to the quantum confinement effects and the size monodispersity of a sample. In addition, they can be extremely efficient emitters, with photoluminescence quantum efficiencies as high as 90%. And finally, their emission can be tuned continuously through large portions of the spectrum. As an example, CdSe quantum dots emit anywhere from 470nm to 630nm light, almost the entire visible spectrum. Subsequent advances in the synthesis of such materials by research groups worldwide have enabled the incorporation of this unique material set into useful devices, and have extended the range of semiconductors which can be made using this general technique. The colloidal synthesis of QD cores was extended to allow for the creation of core-shell type QDs[10, 42] simultaneously by researchers at the University of Chicago and MIT, a key step in the creation of highly luminescent material. This two step process is shown in Figure 1-11.

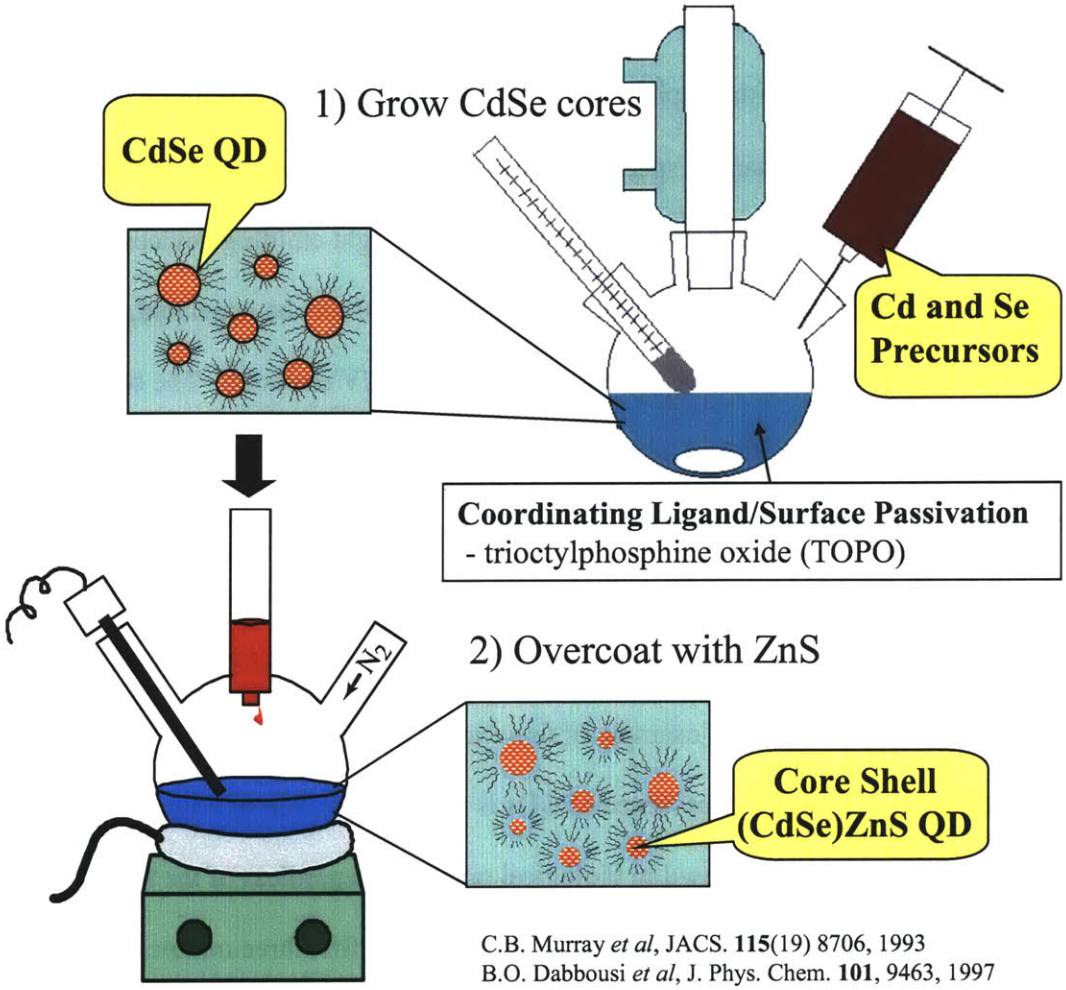

Figure 1-11: Two-step synthesis typical of core-shell colloidal quantum dots. In step one, the (in this case CdSe) semiconductor cores are grown. Organometallic precursor are injected into a high temperature organic solvent. Temperature activates the nucleation of tiny crystallites which can then consume the remaining unreacted precursor to grow to various sizes. The growth is stopped by cooling the reaction vessel. Similarly a shell can be grown on the cores by adding different precursors to a solution of cores, and avoiding the nucleation of new cores of this different semiconductor material. The result can be a solution of core-shell quantum dots of high size monodispersity and high fluorescent quantum yield.

Luminescence properties of inorganic QDs match the performance of good organic lumophores. For example, nanocrystallites of CdSe coated with a ZnS passivation layer [(CdSe)ZnS] have solution photoluminescence (PL) quantum efficiencies of as high as 50%[10]. More recently new techniques for the production of

90% efficient QDs have been reported[43]. In addition, by changing the diameter of the CdSe core from 23 to 55Å, the peak luminescence wavelength can be precisely tuned from λ=470 to λ=640 nm with a typical spectral full width at half of maximum (FWHM) of less than 40nm[42]. This narrow spectrum is perceived as saturated color, motivating the development of efficient, saturated color, quantum dot light emitting devices (QD-LEDs). We expect that even red and blue efficient QD-LEDs can be generated, since in narrow-spectrum LEDs no photons are lost to infrared and UV emission. The broadly and continuously tunable, efficient, saturated color emission of quantum dots is unmatched by any class of lumophores. Furthermore, environmental stability of covalently bonded inorganic nanocrystals suggests that device lifetimes of hybrid organic/inorganic LEDs should match or exceed that of all-organic LEDs, when QDs are used as luminescent centers. An example of this exceptional stability is shown in Figure 1-12. In this case, the photoluminescence of QDs is compared to that of a typical organic small molecule fluorescent dye used in biological tagging. Regardless of the feature being tagged, the organic dye is completely faded within the first three minutes of observation, while the QD tagged sections show no sign of fading. In this application, the use of QDs as fluorescent markers will enable a wider variety of studies to be performed, over a wider range of time due to this increased stability.

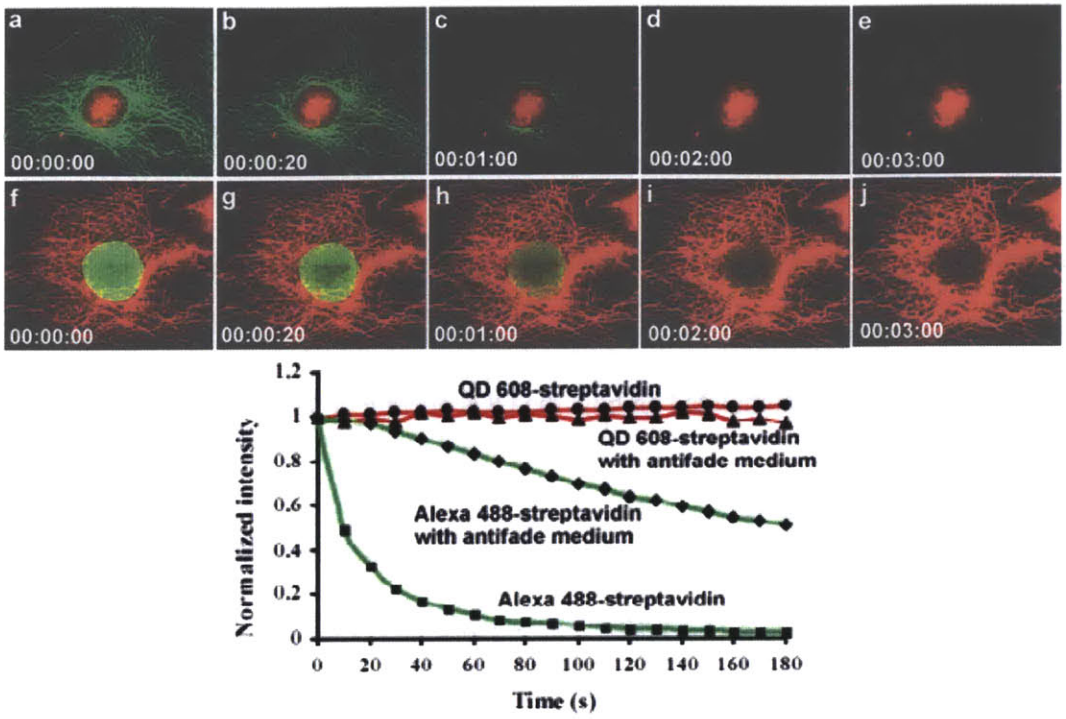

Figure 1-12: Photostability of a QD, courtesy of QDot Corp. Top panel (a-e): Nucleus labeled with Qdot™ conjugates and microtubules labeled with Alexa Fluor 488. Bottom panel (f-j): Nucleus labeled with Alexa Fluor 488 and microtubules labeled with Qdot conjugates. Bottom: quantitative data showing effect of QD photostability.

In contrast to OLEDs, colloidal QD device technology has not yet reached the commercial markets. There is much interest however, in utilizing QDs in such applications as combinatorial chemistry, as narrowband emitting sources for communications, and as biological fluorescent tags (as in Figure 1-12). These applications are likely to be the first instance of technology based upon low-dimensional physics impacting humanity.

From our perspective, QDs can be seen as the ideal lumophore for incorporation into LEDs. Their emission can be tuned throughout the visible spectrum, and thus they can become the only lumophore that is necessary in a full color flat panel display. In

addition, their emission is extremely narrowband, allowing for the creation of high luminous efficiency LEDs in the blue and red, where otherwise light would be lost to the ultraviolet and infrared respectively. As an inorganic emitting body, they have the potential to be far more stable than any organic molecule. Additionally, they still represent an ongoing and fascinating topic of research, and it is our hope that in incorporating the QDs into LEDs, we will be able to contribute to the body of knowledge that is currently being accumulated on how the QDs operate on the most basic levels.

1.7.1 QD Confinement

Understanding of how the energy levels of the QD develop requires a modest understanding of the principles of quantum mechanics and solid state semiconductor physics. In a conventional bulk semiconductor, the charged species (electrons and holes) may be best described by particle wave functions in a periodic medium. However, these wavefunctions are unconfined and experience the periodic medium throughout their extent (which is typically on the order of 10nm). In a confined system such as a QD, these wavefunctions are not able to extend fully, and hence exist at some raised energy state relative to the bulk case. Quantum mechanics allows us to consider the relative energies of a particle within such a confined system, but intuition is sufficient to tell us that this energy is raised as the level of confinement is raised (Figure 1-13). In the case of a QD the degree of confinement is determined by the particle size, and hence as the QD diameter is reduced the energy corresponding to the electron and hole wavefunctions are similarly increased. Thus, an emissive electron-hole pair recombination event will release more energy (if emissive, this means bluer light) as the QD diameter is decreased. The upper size limit at which this effect is pronounced is the diameter at which a bulk

exciton would occupy, which for the case of CdSe is about 12nm. At extremes of smaller QD size, surface effects dominate over any effect of the core crystal, and hence establish some minimum diameter (near 1.7nm) of a functional CdSe QD. At such small diameters, a majority of the core material's atoms are on the surface of the QD.

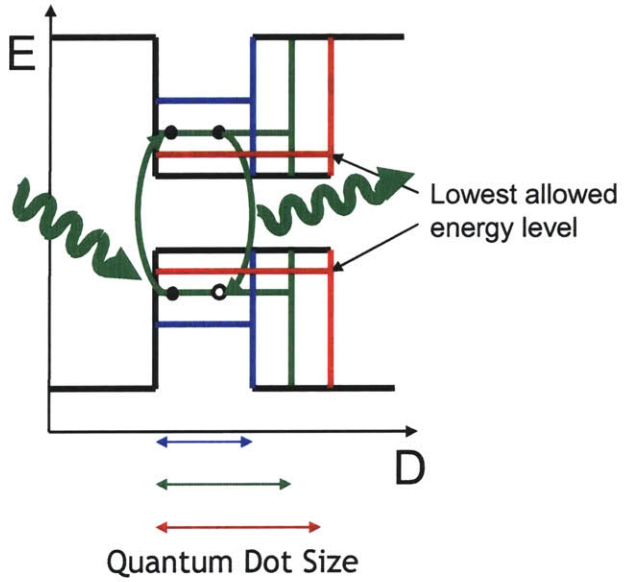

Figure 1-13: Energy band diagram demonstrating how QD diameter contributes to higher exciton energy, and therefore bluer absorption and emission.

Rapid progress has been made in quantifying the electronic structure of semiconductor nanocrystals[44]. For the simplest possible case – a spherical nanocrystal surrounded by an infinite potential barrier, using a parabolic approximation of band structure – the energy of the electron and hole quantum size levels (QSLs), characterized by angular momentum quantum number l[45, 46]

$$E_{l,n}^{e,h} = \frac{\hbar^2 \phi_{l,n}^2}{2m_{e,h}a^2}$$ **Equation 1-1**

where $m_{e,h}$ is the electron and hole effective mass respectively, a is the crystal radius, $\phi_{l,n}$ is the n^{th} root of the spherical Bessel function of order l $j_l(\phi_{l,n}) = 0$. For example, in CdSe QDs, this shift of the energy gap reaches 1.2eV. By changing the nanocrystal size, the energy gap in this material is changed from 1.8eV (bulk value) to 3eV, encompassing most of the visual part of the optical spectrum[47].

Refining this approximation first requires taking into account the Coulomb interaction between the (optically or electrically) excited electron and hole. The magnitude of this interaction is strongly dependent on the relationship between particle size a, and the Bohr radius of the bulk exciton,

$$a_B = \frac{\hbar^2 \kappa}{\mu e^2} \qquad \textbf{Equation 1-2}$$

where μ is the exciton reduced mass and κ is the dielectric constant of the semiconductor[45, 48]. For CdSe (a_B = 6nm), we can assume that $a << a_B$, and hence that we are in the so-called strong confinement regime in which the electron-hole Coulomb interaction lowers the energy of optical transitions only slightly. As a result, absorption spectra are given by[46]

$$\hbar\omega_v = E_g + E_v^h(a) - 1.8\frac{e^2}{\kappa a} \qquad \textbf{Equation 1-3}$$

where the Coulomb correction is calculated in first order perturbation theory. Further refinement of the approximation must take into account the non-parabolic nature of the conduction and valence bands in a real semiconductor. For typical semiconductors of cubic or zinc blende lattice symmetry (e.g. GaAs, CdSe, CdS) the conduction band is parabolic only at the band edge (extreme bottom of the conduction band). The top of the valence band consists of a 4-fold degenerate sub-band describing the dispersion of the light and heavy hole branches for non-zero k, and the spin-orbit split off sub-band (see

Figure 1-14). Various approximations have been utilized to more accurately describe this band structure[49-51], the results of which have been well summarized[44]. When the effects of intrinsic crystal field[52] and nanocrystal shape anisotropy[53] are added to the model, lifting the hole state degeneracy, one can consistently explain the QD Stoke's shift and exciton lifetime in terms of the resultant optically inactive lowest energy excitonic state[54].

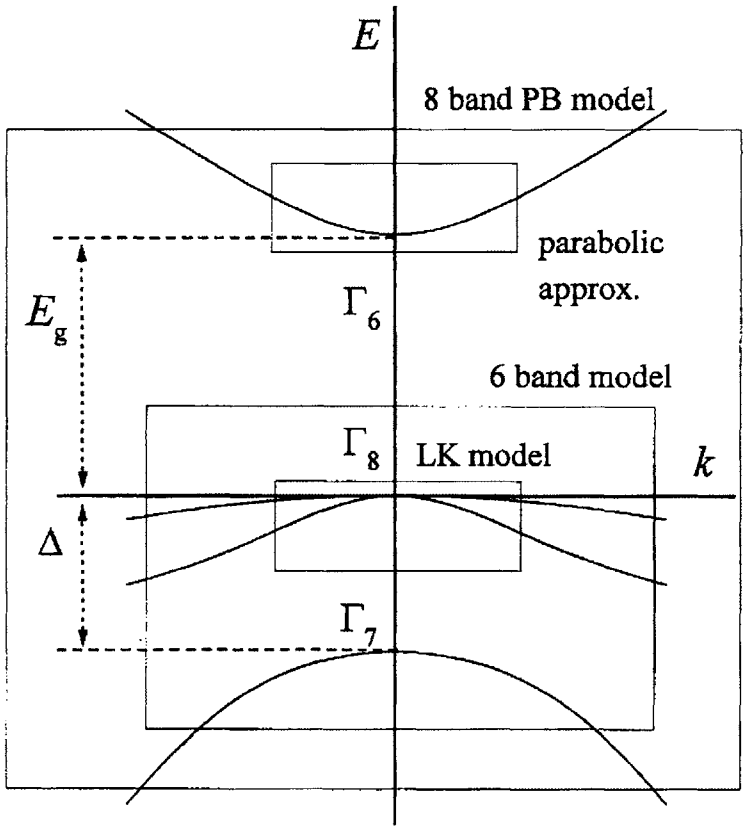

Figure 1-14: The bulk band structure of a typical direct gap semiconductor with cubic or zinc blende lattice structure and band edge at the Γ-point of the Brillouin zone. The boxes show the region of applicability of the various models used for calculation of electron and hole quantum state levels[44].

The function of the ZnS overcoating is explained by considering the QD surface. All of the above mentioned theories rely upon the assumption of the crystal structure

being perfectly periodic. A single crystal of CdSe has this periodicity throughout its bulk. However, this necessarily breaks down at any surface since the periodic crystal structure is not continued. Inorganic semiconductors such as CdSe are covalently bonded solids, with four bonds per atom. At the surface of a crystal, the outermost atoms do not have neighbors to bond to, generating so called dangling bonds. Even perfect crystals undergo some surface rearrangements to minimize the energy of these dangling bonds. The crystal periodicity is thus broken near the surface, giving rise to surface states of different energy levels, which are within the band gap of the semiconductor. In the case of a CdSe QD, these surface states lead to non-radiative relaxation pathways, and thus a reduction in the efficiency of emission. The effect is made more pronounced the smaller the QD diameter, where the surface to volume ratio is larger.

Overcoating mitigates all of these effects. By adding another shell of semiconductor to the crystal, the CdSe dangling bonds are passivated. They are instead replaced with ZnS dangling bonds at the new surface. ZnS also had a larger bandgap than the CdSe, and hence the electronic wavefunction is still well confined within the core. Thus, the wavefunction has only minimal overlap with the dangling bonds and the surface states, and gives rise to a QD with higher photoluminescence quantum yield. It is important to note that their must be reasonable agreement in crystal structure and lattice constant in order to overcoat a given core material with a given shell material. The restrictions on this matching increase as one tries to overcoat with thicker layers of semiconductor shell. In the case of ZnS overcoating CdSe, this mismatch is 25%.

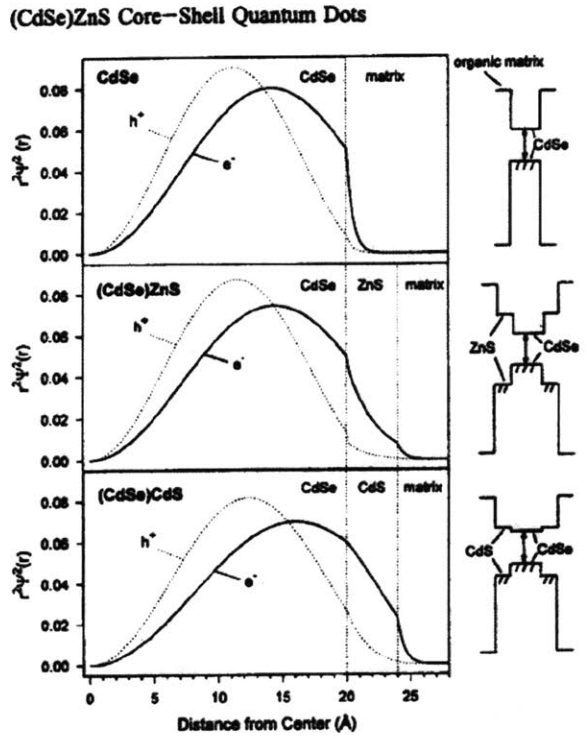

Figure 1-15: Radial probability functions for the lowest energy ($1S_{3/2} - 1S_e$) electron and hole wave functions in (A) bare 20Å diameter CdSe dots, (b) (CdSe)ZnS dots with a 20 Å diameter core and a 4 Å ZnS shell, and (c) (CdSe)CdS dots with an identical core and a 4 Å CdS shell. The sketches to the right show the approximate band offsets between the various components. From Dabbousi *et al* (1997)[42].

The extremely narrow emission band that we are relying upon for our narrow emission QD-LEDs is also due to quantum confinement effects. In a bulk three-dimensional semiconductor, the density of available states above the conduction band rise very quickly ($g(E) \propto E^{1/2}$). However, as the dimensionality of the crystal is reduced, the functional form of the density of states changes. For a truly zero-dimensional crystal the density of states becomes a series of delta functions, one at each of the confined levels with in the "box" (see Figure 1-10). In the non-idealized physical system of a QD between 1nm and 12nm in diameter, these delta functions become broadened, giving rise to the typical bandwidth of QD emission that is observed. Thermal effects contribute to

this broadening as well as the size dispersion in any ensemble sample of QDs. The broadening effects combine to give a typical (CdSe)ZnS spectral FWHM of 25-40nm. A thermally broadened spectrum of a single QD of the same material will have a FWHM of emission that is only ~15nm in width.

Another unique feature of a QD that has been observed is the fluorescence intermittency or 'blinking' phenomenon[55-57]. When imaging dilute films of QDs embedded in a matrix, QD photoluminescence can be observed to turn on or off for long periods of time under uniform illumination. The on QD has been shown to correlate to a charge neutral QD, while the off state correlates to a charged QD. The reason for the reduction in photoluminescence efficiency of a charged QD is the Auger process, where the exciton is quenched by the presence of charge. This non-radiative relaxation process can occur very fast (~100ps[58], relative to τ~10ns for the radiative emission process of a QD) and hence completely darken any charged QD.

1.7.2 Quantum Dot Deposition Techniques

To utilize the colloidally synthesized QDs in a solid state active device structure we looked for a method that would allow us to deposit a thin film of QDs onto a planar substrate. Dry techniques such as thermal evaporation are not available for QD deposition, because their high molecular weight makes sublimation impossible. However, the wet methods employed by the polymer OLED community are accessible to QDs, since they are soluble in many organic solvents. Drop-casting, spin-casting, and ink-jet printing are all promising options. However, these techniques make it challenging to grow even a two layer device structure, and all but impossible to go beyond two layers. We therefore needed to develop a new deposition technique for the creation of multilayer

QD devices. An enabling step in developing any new deposition technique was design of a growth system that allowed for the use of known deposition methods, and was flexible enough to incorporate any new methods that were developed. The linear transfer system was designed to meet these criteria, as discussed later in this chapter.

The solution in which a QD sample is grown is typically a solid at room temperature. The creation of high performance electrical devices utilizing QDs grown from this solution requires the addition of purification processing steps to remove excess materials (the growth solvent, unreacted precursors, etc.). The details of this clean-up procedure are dependent on the growth procedure and materials used, and so will not be discussed in detail in this work. However, it is noted here that refining this procedure is critical to the creation of high purity QD layers. The growth solution is typically not one component but rather a mixture of one or more high temperature solvents, and surfactants that are typically added to the mixture in much smaller quantities. Quantitative analysis of the precise purity of a QD sample is difficult to perform, and thus less precise measures are typically relied upon. In many cases, it is the observations of the solid films formed from a sample that are the most telling of the starting sample purity. A highly repeatable, scaleable clean-up procedure is necessary prior to the development of any QD deposition technique, lest trace impurities within QD samples dominate the experimental results rather than intentionally controlled variables.

Previous methods used for the deposition of QD films from solution are dip-casting, spin-casting, drop-casting, Langmuir techniques, and electrodeposition. All of the above techniques have been used with relative success for the deposition of QD monolayers and multilayers onto various substrates. Dip-casting was the approach taken

by Colvin *et.al.* in their early work on QD-LEDs[59]. This method required pre-treatment of the substrate surface with hexane dithiol as a surface binding agent, but a small molecule like this was no doubt an electrical trap and an exciton quenching site, contributing to the low efficiency of these devices. Spin-casting has been used by many researchers to deposit QDs for many applications[60, 61]. However, our experiments confirm and others have noted in their own reports,[61] that such films are frequently dominated by pin-hole defects which in electrical devices would cause shorts. While these defects can be overcome to some extent by using subsequent treatments, this problem seems to be fundamental to spin-cast films of QDs. Drop-casting has also been a common method for depositing QD films. This technique gives much control over drying times through the use of mixed solvent systems, and people have successfully used the approach to assemble close packed ordered two and three dimensional[62, 63] super-lattices. However, the top surface of such films is typically rough, and therefore does not allow for the construction of vertically stacked devices. Drop-casting also requires precise control over the substrate surface chemistry, making the technique far from generally applicable. Langmuir-Blodgett and Langmuir-Schaefer[64] techniques have also been used to assemble QD films. It is the complexity of this process that has to date prevented its application to any active device. This complexity also makes Langmuir based techniques unlikely to scale well to high throughput manufacturing. Electrodeposition has also been used to deposit nanocrystals[65]. Most recently, there have been several reports of the use of micro-contact printing to deposit QDs[66, 67]. In later chapters of this work, we extend upon this technique to show that it is uniquely

qualified to enable the large area deposition of QD monolayers within active device structures in a reliable and repeatable manner.

2 Device Design

In the previous chapter, the basics of both organic light emitting devices and quantum dots were discussed. In this chapter, we will explore the strengths and weaknesses of prior quantum dot light emitting device structures, and draw conclusions as to what an ideal structure for a QD-LED might be. With this structure in mind, chapters 3 and 4 will then detail two fabrication methods for fabricating such structures, and chapters 5 and 6 will discuss the device operation and results that can be obtained using such methods. Future areas of research are discussed in chapter 7, with growth system integration and parameter calculations left for appendices A and B.

2.1 Previous QD-LED Structures

The first published work on LEDs incorporating colloidally grown CdSe QDs[59] utilized a device structure consisting of a polymer hole transporting layer, and a 15-25 nm thick QD multilayer film (5 monolayers of 3-5nm diameter QDs) as the electron transporting layer (see Figure 2-1, a). The semiconducting polymer *p*-paraphenylene vinylene (PPV) was prepared by spin-casting of the monomer followed by thermal conversion to the polymer at 250°C. A relatively thick layer (100nm) was necessary so as to not have the device performance dominated by shorting defects. The QD multilayers were deposited via a layer-by-layer approach. The ITO/PPV coated substrate was alternately exposed to hexane dithiol and a toluene solution of QDs five times, resulting in the deposition of five complete monolayers of QD solid, separated by organic spacers. The devices operate with an external quantum efficiency of between 0.001 and 0.01%.

While it is possible that the low efficiency of this device is entirely due to low QD luminescence efficiency (the QDs used are core only, not core-shell), we may also attribute the device operation to the structure employed. Electrons are transported through multilayers of QDs, and hence electron transport from QD to QD is necessary. In addition, hexane dithiol was incorporated into the device during fabrication. Such addition of film impurities could either cause charge trapping within the transport layer, or operate as a quenching site for any QD excitons.

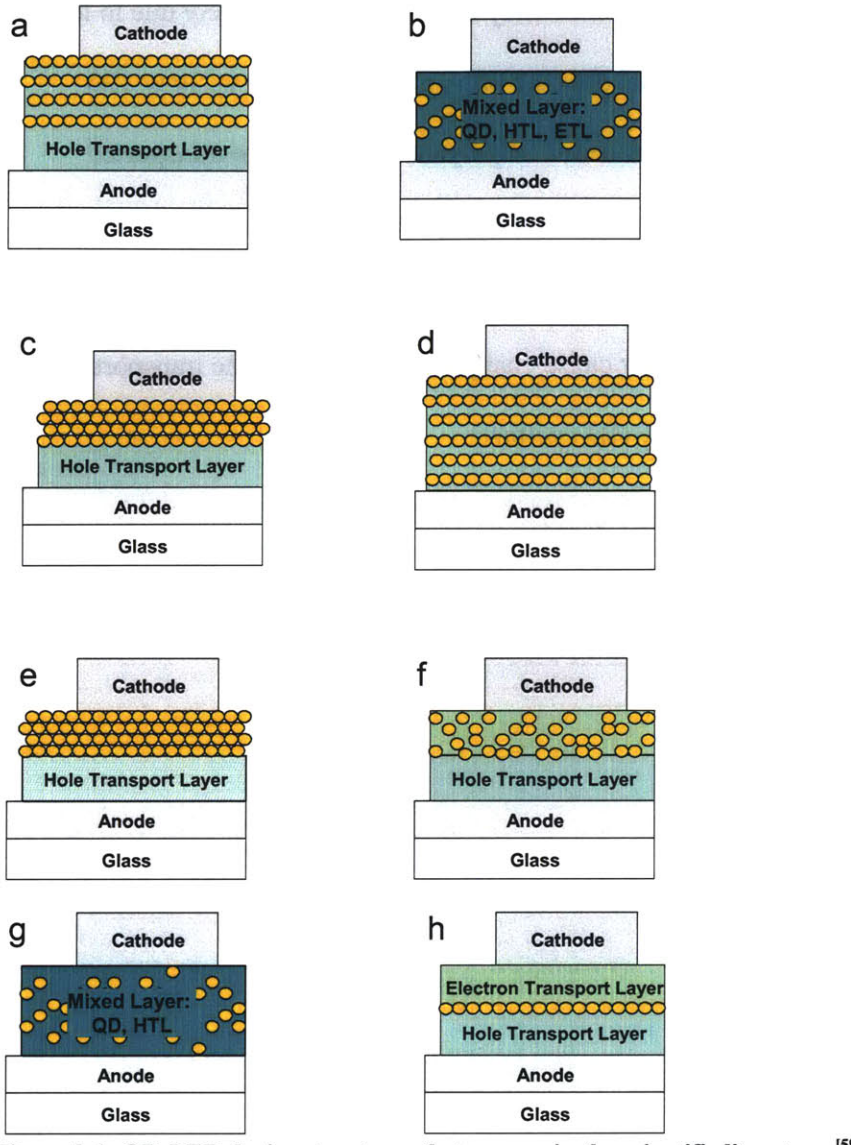

Figure 2-1: QD-LED device structures that appear in the scientific literature.[59, 68-73]

Contemporaneously, a QD-LED structure was fabricated incorporating QDs within a semiconducting polymer matrix,[68] in a single layer structure as shown in Figure 2-1, b. The active layer of the device was spin-cast from a mixture of CdSe QDs (5-10% by volume), polyvinyl-carbazole (PVK), and an oxadiazole derivative (t-Bu-PBD) all dispersed in chloroform. These materials were chosen for their known properties as

efficient transporters of holes and electrons respectively. Again, the external electroluminescence quantum efficiency reported was low (η_{EL} ~0.0005%), and cannot entirely be explained by the QD photoluminescence quantum yield (reported to be ~10% in solution). In this device structure, the QDs are allowed to interfere with both electron and hole conduction, resulting in charged QDs which are likely to be less efficient emitters due to the Auger process discussed in Section 1.7.1. These two studies together demonstrated for the first time that electrically generated QD electroluminescence (EL) was possible, and alluded to the technological potential of QD-LEDs.

Subsequent papers explored the benefits of combining these two approaches[68, 74], with the use of overcoated (CdSe)ZnS[75] and (CdSe)CdS QDs[60]. Schlamp *et.al.* used a thermally polymerized PPV hole transport layer, followed by a spin-cast deposition of a core-shell QD multilayer (Figure 2-1, c). This structure resulted in significant improvement in quantum efficiency, with η_{EL} as high as 0.22%. However, the device response time was in excess of one minute, which was attributed to the presence of trap states within the QD multilayer film.

The layer-by-layer approach was revisited by Gao *et.al.* with a variety of device structures (Figure 2-1, d) based on alternating bilayers of CdSe QDs and polymers such as PPV, poly(allylamine) and poly(styrenesulfonic acid). No device efficiency is reported in this work, which focused primarily on the stability of the devices under both forward and reverse bias. Fabrication in the presence of water was no doubt responsible for the diverse effects reported herein.

Figure 2-1, e, depicts yet another variation of QD-LED device structure[69]. PPV is once again used as the hole transporting layer, though in this work it is deposited using

a layer-by-layer approach, dip-coated in alternating fashion with both sulfonated polystyrene (SPS) and polymethacrylic acid (PMA). After deposition of 30 such bilayers, the films are aggressively dried and thermally cross-linked in a process that takes 36 hours. QDs of either CdSe or (CdSe)ZnS are then spin-cast on top of the converted PPV multilayers. This strategy resulted in $\eta_{ex} = 0.1\%$, and interestingly an inverse relationship between QD η_{PL} and η_{EL}. For the overcoated (CdSe)ZnS QDs, a increase in photoluminescence quantum yield was observed, which translated into a decrease in EL quantum efficiency relative to the equivalent devices made using core only CdSe QDs. This is attributed to a decrease in charge injection into the QDs due to the increased tunnel barrier thickness. Similar results were reported when the single component QD film was replaced with a QD/block co-polymer composite film[70], also deposited by spin-casting of a mixed solution (Figure 2-1, f).

A new QD material set, (InAs)ZnSe, was used to generate efficient EL in the near infrared[71]. This work reported record a device efficiency of $\eta_{EL} = 0.5\%$ using a very simple device geometry (Figure 2-1, g). Blended films of QDs and polymers (either poly[2-methoxy-5-(2-ethylhexyloxy)-1,4-phenylenevinylene] (MEH-PPV) or poly[(9,9-dihexylfluorenyl-2,7-diyl)-co-(1,4-[benzo-[2,1',3]thiadiazole])] (F6BT)) were spin-cast between opposing electrodes.

This was followed by our demonstration of η_{EL}=0.5% visible wavelength QD-LEDs that incorporate a single layer of QDs in a molecular organic structure (see Figure 2-1, h)[76], and extensions upon this to yield η_{EL}=1.1%[77] and most recently η_{EL}=2%[78]. The fast response time and higher η_{EL} of these latest devices matches that of fluorescent OLEDs.

Seen as a body of work as of 2001, the prior art implied that while QDs were an interesting nanoscale material, it was unlikely that they would ever compete with the efficiencies obtained using organic light emitting devices. After 7 years of progress, QD-LED efficiency had still not reached the point at which OLEDs were at in 1987[79]. Furthermore, their highly tunable photoluminescence had yet to be realized in electroluminescence; all the reported devices emitted between 560nm and 630nm. Large area deposition techniques were being employed in device fabrication, but there was no presented equivalent to shadow masking for patterning these solution processable materials. Though progress in the synthesis of efficient materials continued apace, as did research into various applications of QDs, there were no significant works pushing the state of the art in QD-LEDs for a period of roughly 3 years. It seemed the scientific community had lost interest in using these uniquely positioned materials in what was a clear application space for them.

We can ascertain the shortcomings of the two major categories of devices fabricated prior to 2002. For devices in which QDs were homogeneously distributed in a polymer matrix, we expect that the QDs were strongly influencing the film morphology and charge conduction through the polymer layer. Rough surface morphology, typical of thick (more than a few monolayers) QD films likely contributed to the observed low device yields and allowed little freedom in optimizing charge injection, transport and position of the exciton recombination region. In the devices in which QDs were deposited as thick, single component films, the QDs functioned as both lumophores and charge transport layers. QD photoconductivity experiments give us direct evidence of the poor conduction properties of thick QD films relative to organic semiconductors[80]. In

addition, thin films that have both charge and excitons present often undergo quenching mechanisms such as polaron-exciton quenching or Auger recombination[81]. The goal of our work is to allow the QDs to function exclusively as lumophores, and to play as little role in QD conduction as is feasible.

2.2 Isolating Quantum Dot Function

The prior art in QD-LEDs utilized a diversity of materials, deposition techniques, and device structures in their attempts to produce efficient devices. Looking at the improvement made in OLEDs during the same time period, one can notice a trend towards the addition of layers to the device structure, typically with the intent of isolating the function of each layer[82]. Charge injection was controlled using one molecule optimized for this function, charge transport another, and light emission a third. The ability to create layered structures of distinct materials is one of the principle advantages of small molecule OLEDs (SMOLEDs) as compared to polymer OLEDs, and in part explains the higher device efficiencies that have been achieved by SMOLEDs.

To improve upon the performance of QD-LEDs, we learn from the insights of SMOLED research. QD-LEDs are of interest primarily because of the unique luminescent properties of the QDs in comparison to organic lumophores; the QDs are narrow band, saturated color, stable, solution processable, and efficient emitters of light. However, prior art tells us that they are not effective transporters of charge (see Figure 2-2), especially in the cases where thick multilayer films of close packed QDs are used. Even in the instances where the QDs were doped into matrices of charge transporting polymers, the adverse effects of the QDs presence were observed, whether in reduced device quantum efficiency or in raised operating voltages. Additionally, the majority of

the QDs used in the device fabrication could not operate in their intended fashion. We understand from OLED research the effect of plasmon quenching when excitons are formed too close to an electrode[83]. Hence, a large portion of the QDs used in the QD-LED device structures were not only disruptive of charge transport, but could not contribute greatly to light emission due to their proximity to the electrodes. In the following section, we consider the design of an idealized QD-LED device structure.

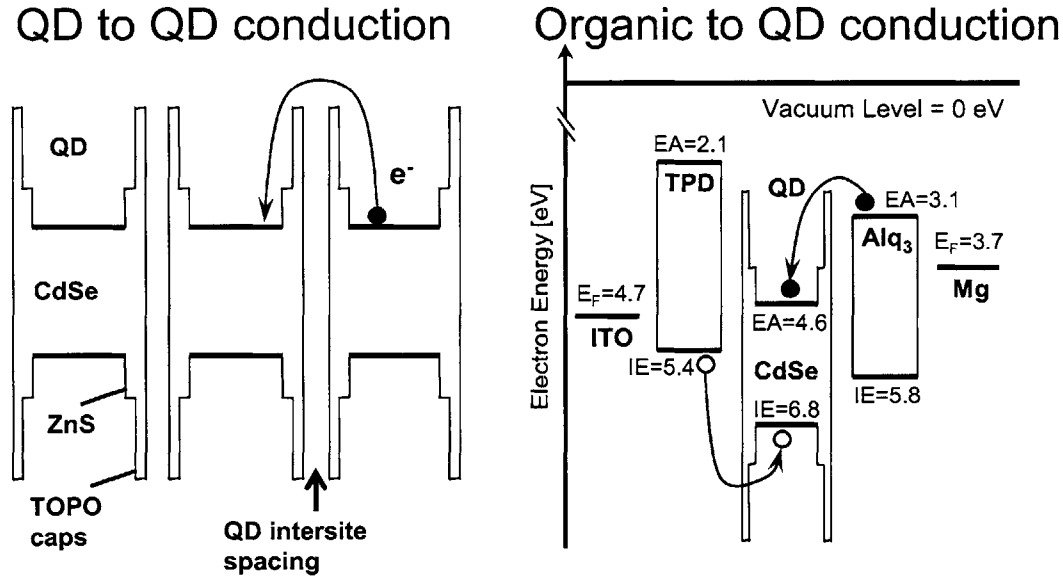

Figure 2-2: Energy band diagrams showing the difficulty of conducting electrons from one QD to another, versus conducting electrons from a neighboring organic molecule into an adjacent QD.

2.3 Idealized QD-LED Structure

In separating the QD function of light emission from charge transport, we immediately see the deficiencies in the diverse device structures already fabricated (see Figure 2-1). All of these previous structures allow QDs to be proximal to the cathode. They all allow QDs to participate in conduction to some greater or lesser extent. If for the time being one ignores the issue of how to fabricate such layered structures, it is clear

that the ideal QD-LED structure to be built would enable the efficient delivery of both electrons and holes to the emitting QDs. The QDs would be located where the electrons and holes meet, and nowhere else. With only these two very simple principles, a new device structure begins to emerge, depicted in Figure 2-3. The electron and hole transport layers (and electron and hole injection layers) are isolated from the QD deposition, and can therefore be optimized independently. The electrons and holes will meet at the QD emissive layer, and there create excitons on the QDs, which can emit radiatively.

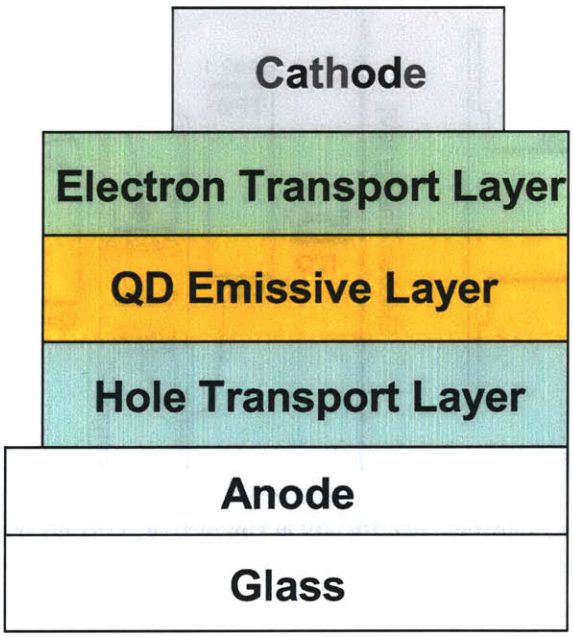

Figure 2-3: Idealized QD-LED structure. The exact nature of the QD Emissive Layer is dependent on the operating mechanism of the device.

How exactly we choose to create excitons on the QDs will determine the detailed structure of the QD emissive layer. Two possible mechanisms for electroluminescence from QDs have been proposed, and indeed both are possible depending on the device structure employed. Figure 2-4 graphically depicts these two processes, exciton energy

transfer, and direct charge injection. In exciton energy transfer, an exciton is first created on an organic molecule, which then transfers onto the QD prior to emission. In the case of direct charge injection, an electron and hole (negatively and positively charge polaron) are seperately introduced to the QD, where they form an exciton. Choosing which of these mechanism we want to dominate within our QD-LEDs will determine the composition of the QD emissive layer in our ideal QD-LED device.

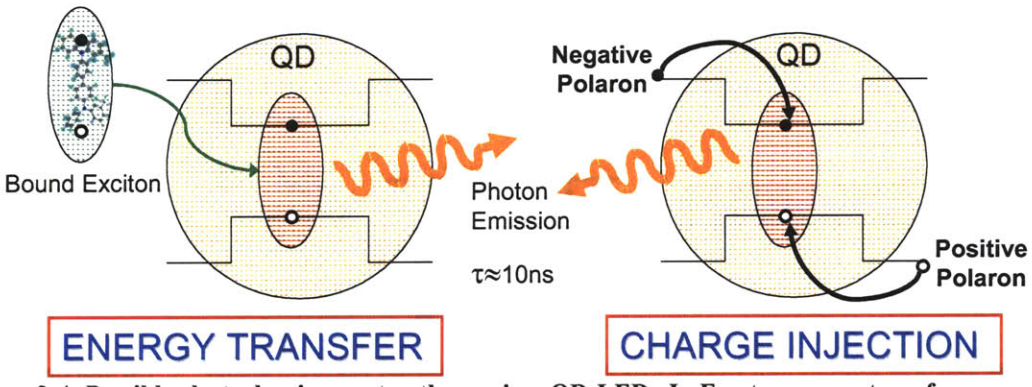

Figure 2-4: Possible electroluminescent pathways in a QD-LED. In Forster energy transfer, an exciton is first created on an organic molecule, which then transfers onto the QD prior to emission. In the case of direct charge injection, an electron and hole (negatively and positively charge polaron) are seperately introduced to the QD, where they form an exciton.

For the case of a QD-LED operating via energy transfer, our goal is to design a device that optimizes the creation of excitons on the organic donor molecules and allows for the complete energy transfer of those excitons to the receptor QDs. We also want to utilize as few QDs as possible so that we continue to minimize their impact on conduction. If we assume that the QD emissive layer (see Figure 2-3) is the region of the device where all excitons are created, then we meet this goal by placing QDs within this donor layer matrix, spaced evenly in all three dimensions. Research on the thickness of the exciton recombination layer in SMOLEDs tells us that for a wide range of current densities, the majority of the excitons are created within a region that is only 5-10nm

thick[84, 85]. Figuring out the ideal spacing of the QDs in the plane of this 5-10nm thick layer is dependent on the length scale over which exciton energy transfer processes can occur. Exciton energy transfer can occur by either Förster or Dexter transfer, as depicted in Figure 2-5.

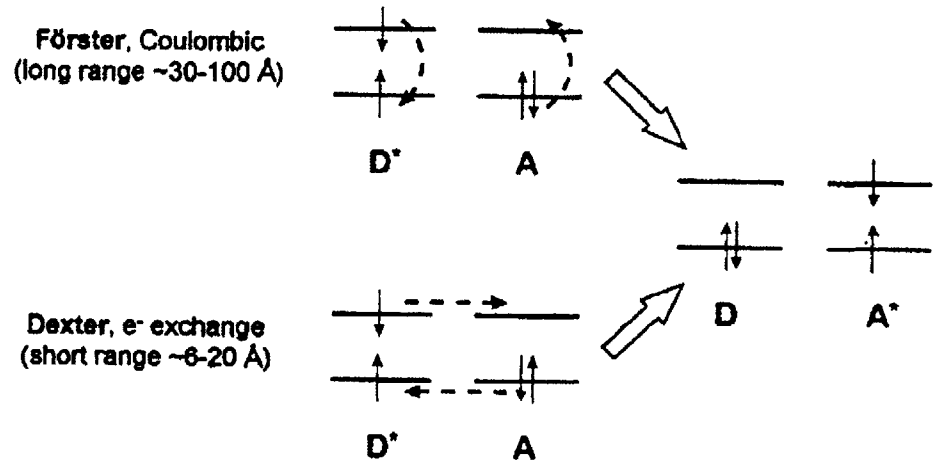

Figure 2-5: The Forster and Dexter processes in singlet-singlet energy transfer[86]. Up and down arrows indicate the spin state of individual electrons. Dashed arrows indicate direction of electron transfer.

In Dexter energy transfer, electrons and holes are directly exchanged from one species to another. Because of this, Dexter transfer occurs only over short distances of ~1nm[5]. We assume that Dexter transfer to the emissive states of a QD is only available from the nearest organic neighbors of a given QD, since the typical length of the QD capping ligands (plus the shell thickness for a core-shell QD) is also 1nm. Thus, for Dexter transfer to operate within this ideal device structure, our QD to QD spacing would be exactly one molecular length longer than the QD diameter, as depicted in Figure 2-6, a.

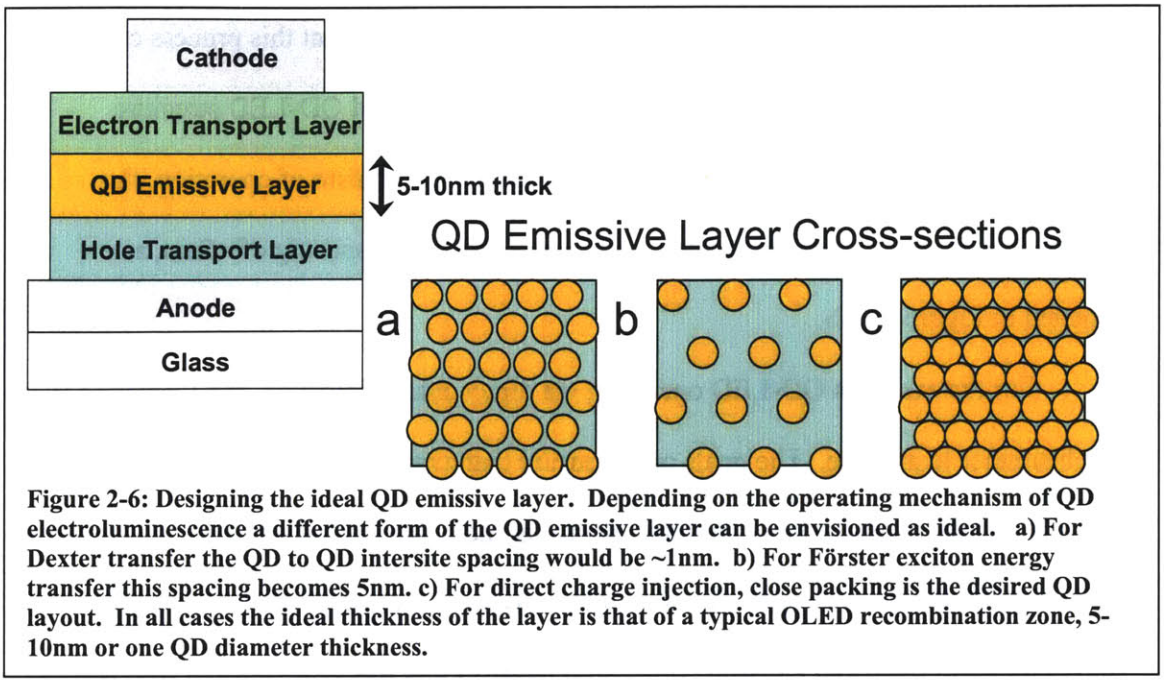

Figure 2-6: Designing the ideal QD emissive layer. Depending on the operating mechanism of QD electroluminescence a different form of the QD emissive layer can be envisioned as ideal. a) For Dexter transfer the QD to QD intersite spacing would be ~1nm. b) For Förster exciton energy transfer this spacing becomes 5nm. c) For direct charge injection, close packing is the desired QD layout. In all cases the ideal thickness of the layer is that of a typical OLED recombination zone, 5-10nm or one QD diameter thickness.

In contrast to this, Förster energy transfer[87] can occur over much longer distances[88]. Förster transfer describes the dipole-dipole interaction of an excited donor molecule and a ground state acceptor molecule. The electric field generated by the excited dipole falls off as R^{-3} (where R is distance from the dipole, near field), and the induced dipole in the acceptor molecule can be shown to be proportional to R^{-3}, giving rise to the R^{-6} dependence of the transfer rate:

$$K_{D\to A} = \frac{1}{\tau_D}\frac{1}{R^6}\left(\frac{3}{4\pi}\int\frac{c^4}{\omega^4 n_0^4}F_D(\omega)\sigma_A(\omega)d\omega\right) \qquad \textbf{Equation 2-1}$$

Where, $F_D(\omega)$ is the normalized fluorescence emission spectrum of the donor, $\sigma_A(\omega)$ is the normalized acceptor cross section in units of cm^2, n_0 is the medium index of refraction, c is the speed of light, τ_D is the natural lifetime of the donor in the absence of quenchers, and the ω integration is over all (angular) frequencies. Using Equation 2-1, and plugging in typical numbers for an organic guest: host thin film, it has been shown

that the dipole-dipole interaction can be significant out to distances as large as 10nm. Furthermore, in QD/organic hybrid systems, it has been shown that this process can occur with lengths scales that are identical[89]. Thus, for the idealized QD-LED structure operating with Förster energy transfer as the dominant mechanism of operation, the emissive layer would be 5-10nm thick, and have a QD to QD spacing of ~5nm, as depicted in Figure 2-6, b.

For the case of a QD-LED operating via direct charge injection, the ideal case is much simpler to analyze. The goals are to ensure that every electron (or hole) is injected into a QD at the emissive layer, and that electrons and holes are not allowed to recombine on any other species. Thus, the emissive layer should be a close packed film of QDs. Elimination of QD to QD electron conduction requires that this close packed film is exactly one monolayer thick. This gives rise to the QD emissive layer design depicted in Figure 2-6, c.

2.4 Target QD-LED Structure

Throughout the remainder of this work, we choose to focus on the device structure shown in Figure 2-6, c. The reasons for this are two-fold: constraints in fabrication tell us that arranging nanoscale objects on a surface with a fixed distance between them is extremely challenging. Two QDs sitting one nanometer (1nm) apart will have a strong van der Waals attraction between them, and in the absence of an equally strong fixative force, these QDs will aggregate to form a closer packing layer. In addition, the ever present goal of this work is to make an efficient device, and so we choose to operate via direct charge injection. Operating via energy transfer will effectively limit our performance to that of the donor organic molecule. In the case of

fluorescent donors this means an external quantum efficiency not to exceed 5%. One can envision using organic phosphors as donors to create 20% efficient QD-LEDs in this manner, but the lack of an efficient, high energy donor phosphor will clearly prevent this mechanism from being available for a blue emitting QD-LED. By utilizing direct charge injection, we hope to prevent the singlet-triplet ratio of organic lumophores from affecting the performance of our QD-LEDs. The seemingly analogous problem of the QD 'dark exciton' state[90] is not an issue for device operation at room temperature, since the energy difference between the dark and bright excitonic states is below k_BT, or 26meV for T=298K.

3 Phase Separation

In the previous chapters, the basics of organic light emitting devices, quantum dots, and quantum dot light emitting devices were discussed, leading to the design of an ideal QD-LED structure. With this structure in mind, the following chapters detail two methods for fabricating such structures. The final chapters will discuss the device operation and results that can be obtained using such methods.

3.1 Introduction

We investigate a new method for forming large area (> cm^2), ordered monolayers of colloidal nanocrystal quantum dots (QDs). The QD thin films are formed in a single step by spin-casting a mixed solution of aromatic organic materials and aliphatic-capped QDs. The two different materials phase separate during solvent drying, and for a predefined set of conditions the QDs can assemble into hexagonally close packed crystalline domains. We demonstrate the robustness and flexibility of this phase separation process, as well as how the properties of the resulting films can be controlled in a precise and repeatable manner. Solution concentration, solvent ratio, QD size distribution and QD aspect ratio affect the morphology of the cast thin film structure. Controlling all of these factors allows the creation of colloidal crystal domains that are square microns in size, containing tens of thousands of individual nanocrystals per grain. Such fabrication of large area, engineered layers of nanoscale materials brings the beneficial properties of inorganic QDs into the realm of nanotechnology. For example, this technique has already enabled significant improvements in the performance of QD light emitting devices.

The colloidal synthesis of inorganic nanocrystal quantum dots (QDs)[10, 40, 42, 91] enables tuning of QD material properties with atomic level precision. Research on devices that harness these properties can be divided into two distinct classes: point-contact devices that utilize a countable number of nanocrystals, or large area devices that utilize great numbers of QDs. In both cases, controlling the placement of the QDs within the active device structure presents the greatest challenge to device fabrication. Many of the earlier studies dedicated to assembling 2D and 3D superlattices of QDs on solid substrates[62, 66, 92-94] present techniques that require long preparation times and precise control of surface interactions to achieve ordered assembly, making the incorporation of such techniques into a working device structure challenging.

The present work investigates the phase separation during spin-casting process, capable of arranging QDs over large areas (cm^2) in two-dimensional sheets within layered structures. This process simultaneously yields QD monolayers self-assembled into hcp arrays and places this monolayer on top of a co-deposited contact. We describe the QD phase separation and self-assembly processes and how to controllably tune the resulting film properties. The technique has already been used in the structuring of efficient quantum dot light emitting devices (QD-LEDs),[76, 77, 95] but as a general and flexible fabrication technique this method could enable fabrication of a wide variety of large area nanostructured heterostructures. QD monolayers arranged onto organic thin films are a unique platform for the study of basic physical properties of materials, for example allowing investigation of coarsening mechanisms on the individual adatom (in this case a single QD) level.[96, 97]

The fabrication of a monolayer sheet of close-packed QDs by phase separation during spin-casting is in essence a very simple process, as depicted in Figure 3-1. The process relies upon the solvation of both the organically capped semiconductor QDs and the organic material to be used as an underlayer in a compatible solvent system. During solvent drying, the QDs phase separate from the organic underlayer material, and rise towards the surface of the film. When drying is complete, the organic material is in the form of a homogenous thin film, which is coated by a layer of QDs. For typical solvent systems, the film is dry well before equilibrium is achieved, and thus the film formation is arrested in a non-equilibrium condition. The exact structure and composition of the layer is completely determined by the composition of the spin-casting solution (for a fixed set of processing conditions). Hence, the material purity of the QD sample is of critical

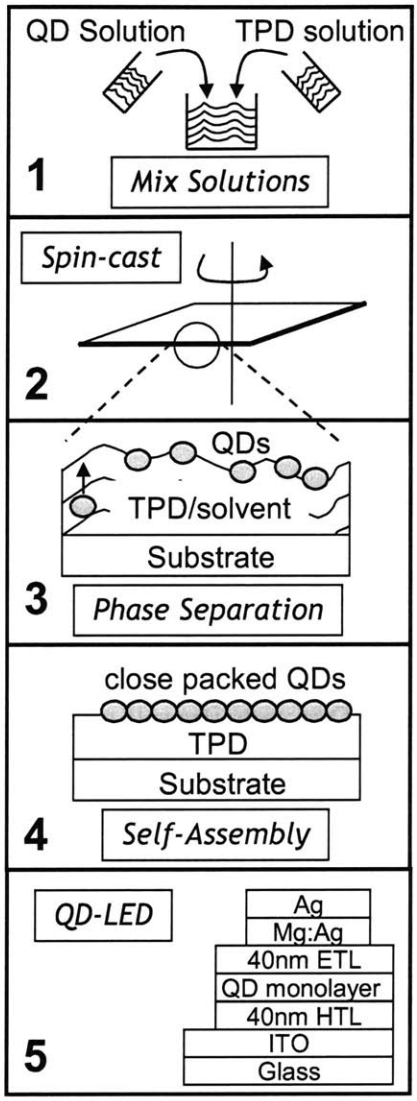

Figure 3-1: Graphical description of the fabrication of organic/QD bilayers through phase separation during spin-casting: TPD exemplifies the organic material. The entire process can be completed on the time scale of seconds, differentiating it from other QD self-assembly techniques. This fabrication process enables the creation of efficient QD-LED structures,[76] depicted in Step 5.

importance to the phase separation process (see Experimental). As an example, the fabrication can be continued resulting in a complete light emitting device.

While it is impossible for any thin film fabrication method to be universally applicable, we demonstrate that within the extent of this study the phase separation process is not critically dependant on any one component of the system. We observe phase separation and assembly of QD monolayer sheets for a number of substrates, solvents, organic underlayer materials, QD core materials, QD organic capping groups, QD diameters, QD size aspect ratios, spin-casting parameters and environmental conditions. Table 3-1 lists the materials used to demonstrate the generality of this process. The only known constraints on the phase separation process are 1) that there is a solvent or solvent system which dissolves both QDs and organics in the needed concentrations, and 2) that the solvent and organic layer wet the substrate surface.

Table 3-1: Examples of materials compatible with the phase separation process: A list of materials that have been incorporated successfully into the phase separation process. This list is not meant to be exhaustive, but rather representative of the materials that are compatible. TPD = N,N'-diphenyl-N,N'-bis(3-methylphenyl)-(1,1'-biphenyl)-4,4'-diamine; NPD = 4,4-bis[N-(1-naphthyl)-N-phenylamino]biphenyl; poly-TPD = Poly(N,N'-bis(4-butylphenyl)-N,N'-bis (phenyl) benzidine; CBP = 4,4'-*N,N'*-dicarbazolyl-biphenyl; Alq_3 = tris-(8 hydroxyquinoline)aluminum; TOPO = Trioctylphosphine oxide; Eponate 12 = trade name of epoxy available from Ted Pella Inc; ITO = indium tin oxide.

Organic hosts	TPD, NPD, poly-TPD, CBP, Alq_3, polycarbonate
Solvents	Chloroform, chlorobenzene, toluene, benzene, pyridine
QD core materials	PbSe, CdSe, and (CdSe)ZnS, (CdS)ZnS, Au
QD capping molecules	Oleic acid, pyridine, TOPO, dodecane thiol
QD core diameter	3-10nm
QD size aspect ratio	1:1 (spherical), 5:2, 5:1 (nano-rod)
Substrates	Silicon, glass, ITO, parylene-C, 'Eponate 12' epoxy

3.2 Results and Discussion

3.2.1 Control of Underlayer Thickness

Perhaps the simplest film property to control in this process is the underlayer organic film thickness. It is well known that the thickness of spin-cast organic thin films may be controlled by varying the solution concentration while fixing the spin parameters. For example, for a fixed set of spin conditions, the phase separation process remains unaffected when the TPD (N,N'-diphenyl-N,N'-bis(3-methylphenyl)-(1,1'-biphenyl)-4,4'-diamine, an archetypical organic) concentration in the solution is changed from 2mg/ml (resulting in 12nm underlayer film thickness) to 94mg/mL (440nm underlayer film thickness). Figure 3-2(f, inset) shows that the relationship between the TPD concentration in a chloroform solution and the resulting underlayer film thickness is linear. AFM images of these surfaces reveal that phase separation is still present in all samples, and that the fraction of QD surface coverage is completely independent of underlayer film thickness. This separation of parameters facilitates optimization of device performance in fabricated structures.

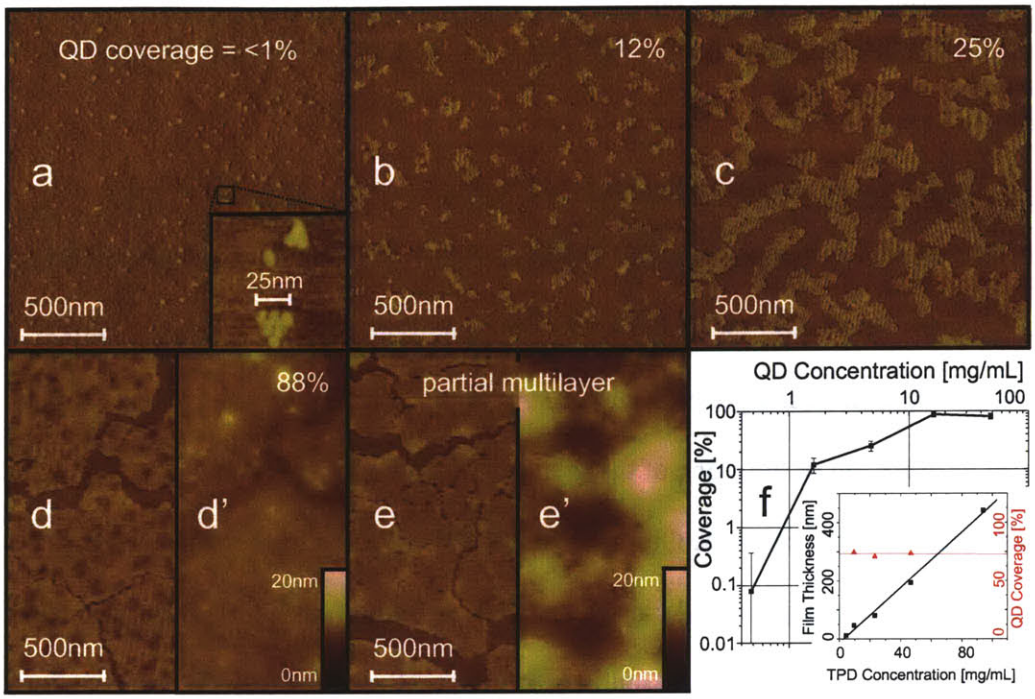

Figure 3-2: Effect of solution concentration on the phase separation process: Tapping mode AFM images of QDs assembled on an organic surface. As the concentration of QDs in the spin-casting solution is increased, the surface coverage of QDs is increased. The images show QD partial monolayers (a-d) with various coverages, and a partial multilayer that results from even higher QD solution concentrations (e). Figs. (a-e) are phase images, while Figs. (d', e') are the corresponding height images which demonstrate the increase in surface roughness for multilayer QD films. QD concentrations are Fig. (a) 0.48 mg/mL, (b) 1.6 mg/mL, (c) 4.8 mg/mL, (d) 16mg/mL, and (e) 48 mg/mL. Fig. (f) shows the dependence of QD monolayer surface coverage on concentration of QDs in the spin-casting solution. The inset plots the linear dependence of organic film thickness on the concentration of organic in the spin-casting solution (TPD in chloroform). The parameters that are varied in the two plots are completely independent, allowing organic layer thickness to be tuned independent of QD surface coverage fraction. The QDs in this figure are 6.5nm diameter PbSe cores, prepared as described in the Experimental Section.

3.2.2 Control of Monolayer Surface Coverage

The concentration of QDs in the spin-casting solution may also be tuned, with predictable effects on the resulting bilayer. For very low QD concentrations, the bilayer film (see Figure 3-2(a)) contains a countable number of QDs distributed homogeneously on the organic surface. The QDs can be imaged individually, or in close-packed groupings of two or more crystals. As the solution QD concentration is increased, the

number of QDs on the surface of the film increases (see Figure 3-2(b)-2(d)). Figure 3-2(f) plots the observed percent coverage versus QD concentration in the spin-casting solution.

As the QD solution concentration is increased, a nearly complete coverage of QDs on the organic surface is observed. If the concentration of QDs in the spin-casting solution is further increased, the result is a breakdown of the flat, uniform morphology shown in the other AFM images in this work. As more QDs than can fit try to pack, they are forced to break out of the plane of the monolayer and seek lower energy conformations. In some cases the QDs pile up into three dimensional stacks, leaving exposed regions of the organic underlayer. In other cases the first layer coverage remains high, but a buildup of regions of QD multilayers occurs (Figure 3-2(e)). Within this work we do not study such multilayer structures, but instead focus on the more controllable process of generating ordered monolayer and sub-monolayer coverage.

3.3 Control of Packing Order and Grain Sizes

3.3.1 Quantum Dot Size Distribution

The degree of hexagonal packing that is observed on a QD monolayer is directly related to the polydispersity of QD diameter. Figure 3-3 shows three partial QD monolayers, spin-cast from solutions formulated from three different QD samples. Figure 3-3(a) shows an example of a largely disordered film, made from a QD sample with size distribution standard deviation (σ_{SD}) of >10%. Although the film stack is determined by the phase separation process, the self-assembly into an hcp array of particles has been prevented by the size dispersion.

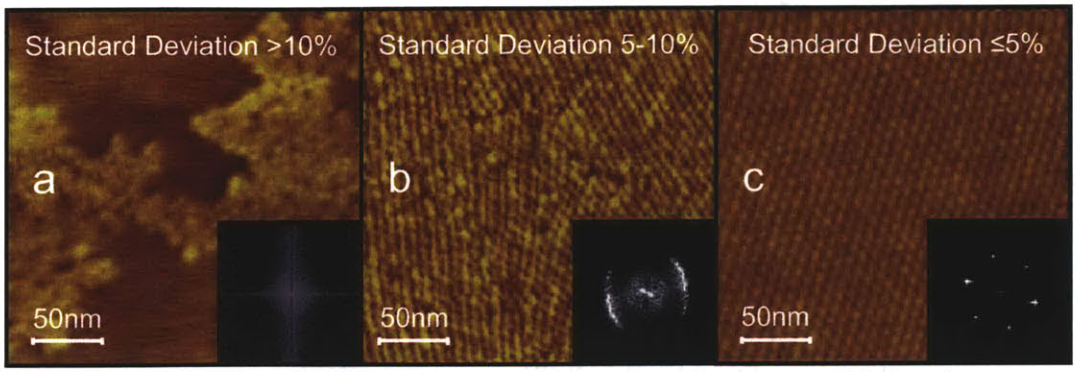

Figure 3-3: Effect of QD size distribution on the degree of packing order: AFM phase images demonstrating this effect. For broad size distributions (a, (CdSe)ZnS), the QDs assume random packing. As the size distribution is narrowed (b, red emitting bare CdSe, c, 5.5nm PbSe) the QDs clearly pack into hexagonal arrays. For monodisperse samples with $\sigma_{SD} < 5\%$ (c), high degrees of order are achievable, with grain sizes larger than $1\mu m^2$. The insets show the two dimensional spatial Fourier transforms of the images. For the perfect single grain (c), the Fourier transform reveals the expected six point pattern. These six points blur into a ring for the image containing a large number of grains (b), and shows no distinct features for the disordered film. Fourier analysis is an effective method of measuring the periodicity (QD center to center spacing) of the QD monolayers.

Figure 3-3(b) shows a bilayer formed from a QD sample with σ_{SD} = 5-10%. While it is clear that the QDs have assembled into the hcp monolayer structure, the ordered domains, or grains, remain small, containing at most a few hundred QDs per grain. It is noted that this size distribution is narrow enough to form high coverage monolayers which are of high enough quality for the fabrication of monochromatic emitting QD-LEDs.

By careful control of QD synthetic techniques, $\sigma_{SD} < 5\%$ is achievable (see 3.9 Experimental). Figure 3-3(c) shows an AFM image of an hcp bilayer created with such a sample, in this case 5.5nm PbSe QDs with oleic acid caps on a TPD underlayer. The high degree of spatial periodicity of the sample enables clear imaging of individual QDs in the hcp colloidal crystal as depicted in Figure 3-4. The average grain size exceeds $1\mu m^2$, with a high degree of two dimensional ordering over tens of thousands of repeat units.

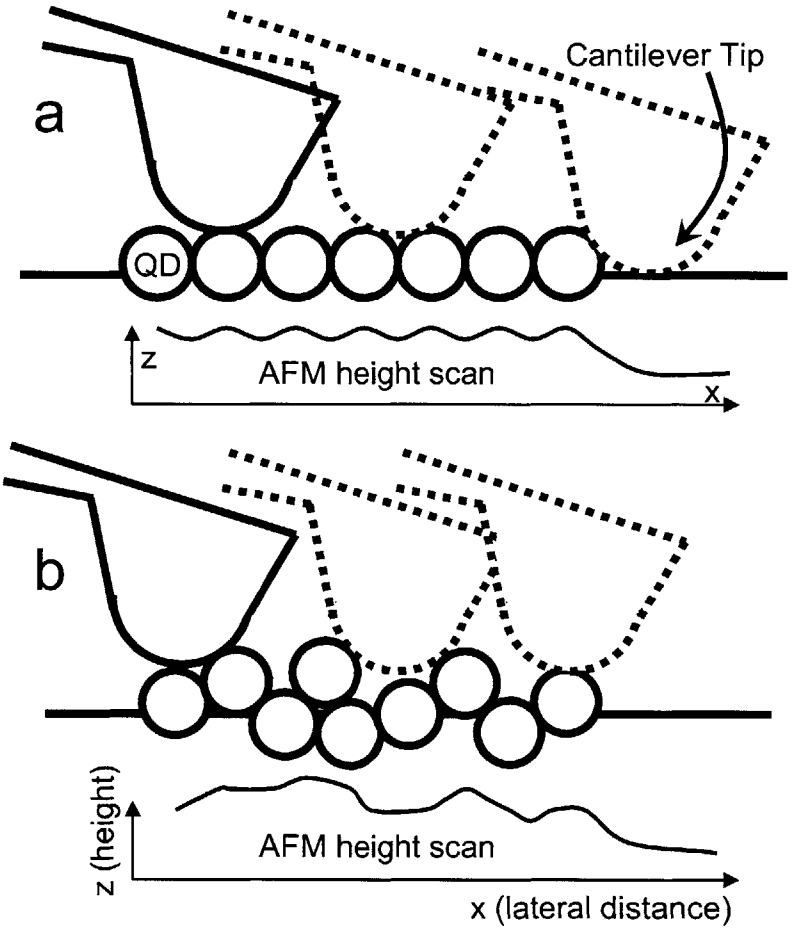

Figure 3-4: Depiction of the effect of surface roughness on the resolution of Atomic Force Microscopy (AFM). The pervasive use of tapping mode AFM throughout this work as a primary method of analysis is chosen over other microscopy techniques due to its ease of use, resolution, and flexibility of substrate compatibility. In contrast, transmission electron microscopy (TEM) requires lengthy preparation techniques that would make the production of optimized devices prohibitive. Also, scanning electron microscopy (SEM) lacks the necessary resolution to easily image individual ~5nm particles. The AFM image resolution is in part determined by the probe tip radius, which was specified as <10nm for all the probes used for this work. The ability to resolve features that are smaller than this tip radius is due to the flatness of the samples (as in Figure 3-4(a)). For exceptionally flat samples, imaging is done with the extreme tip of the probe, whereas the presence of any larger height variations (as when surface disorder is present) results in imaging with the entire tip diameter, setting the minimum resolvable feature size to ~20nm (as in Figure 3-4(b)). Smooth surfaces allow for resolution below the size scale of the probe tip diameter.

3.3.2 Quantum Dot Size Aspect Ratio

QD eccentricity, or size aspect ratio, also determines the degree of self-assembled order in these QDs monolayers.[98] Many of the II-VI colloidal semiconductors have a

Wurtzite crystal structure, with a unique c-axis in the crystal unit cell. Recent work has exploited this asymmetry in the crystal structure to create growth anisotropy, yielding nanocrystals with controllably tuned size eccentricity from $R_A = 1.0$ (spherical) to several 100 (rod shaped nanocrystals).[91] Figure 3-5 demonstrates that the phase separation process is unaffected by changes in aspect ratio from $R_A = 1$ to 5, but that the degree of ordering is reduced in samples made from more rod-like nanocrystals. In these nanorod monolayers the minimum energy phase is likely liquid crystalline rather than the hcp structure we see for $R_A = 1$ nanocrystals.

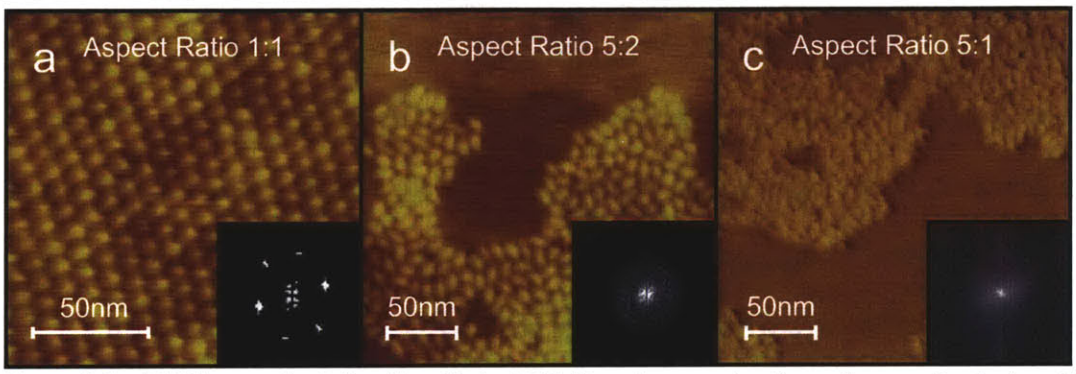

Figure 3-5: AFM images depicting the effect of QD diameter aspect ratio on degree of ordering. For spheres with narrow size distributions the packing is highly ordered (a), while for samples with larger aspect ratios (b, c) packing is observed but ordering is nonexistent. This is due in part to the lack of size monodispersity on the length of the QDs, which is independent of the diameter monodispersity in these samples. The insets display the spatial Fourier transform of the images, highlighting the differences in order between the images. The nanocrystals used in this study are (a) 7 nm PbSe QDs, (b) red emitting CdSe core-shell QDs, and (c) CdSe nanorods.

3.4 Solvent

The crystallinity of the ordered domains is strongly affected by the solvent drying time during the spin-casting process. Solvent drying time is directly related to solvent vapor pressure, and as such a wide range of control is possible using only two miscible solvents. We chose to work with chloroform and chlorobenzene, as they have similar solubility properties (both solvate TPD and oleic acid capped QDs effectively), but very

different vapor pressures (chloroform = 26.2kPA, chlorobenzene = 1.6kPa). Chloroform solutions dry in less than a second during the spin-coating process, while chlorobenzene solutions dry only after several seconds of spinning. A continuous range of solvent drying times could be achieved by mixing these two solvents in different ratios.

The equilibrium condition for monodisperse (σ_{SD} <5%) QDs arranged into a two dimensional sheet is a single hcp grain. A trend towards equilibrium is demonstrated in Figure 3-6, which depicts a series of spin-cast bilayer films that are made from the same QD sample and the same concentrations of both QDs and TPD. The solvent used is varied from 100% chloroform (fastest drying, Figure 3-6(a, d)) to 100% chlorobenzene (slowest drying, Figure 3-6 (c, f)). The mean QD island size is maximized for the mixed solvent system. Small grain boundaries, however, are visible in the 8μm scan (Figure 3-6(e)) and are more clearly visible in the 2μm scan (Figure 3-6 (b)) of the mixed solvent sample. Such grain boundaries, internal to an island, do not occur in the chlorobenzene sample, where almost every island is a single grain, in many cases larger than $1\mu m^2$.

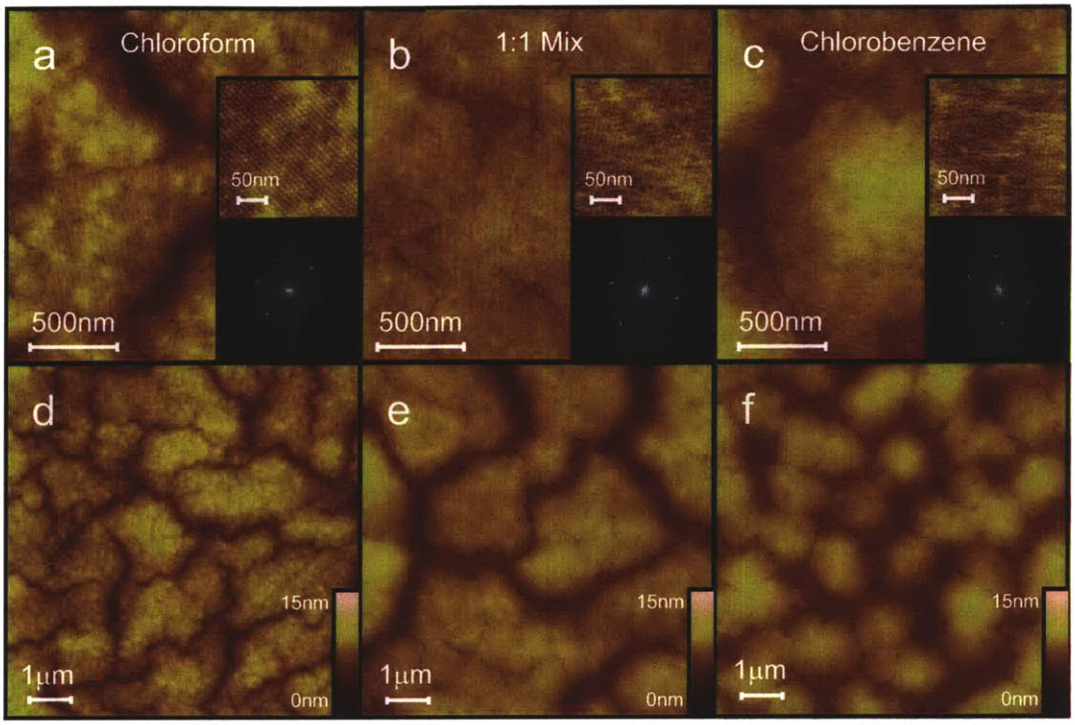

Figure 3-6: Effect of solvent on grain size and structure: AFM height images of QD monolayers on TPD spun from identical concentration solutions of different solvents. (a) and (d) are images of the same film at different scan sizes, as are (b) and (e), and (c) and (f). In (f) each island is a single grain of colloidal crystal (sizes exceeding 1μm^2), while in (d) and (e) the islands are composed of multiple grains separated by narrow grain boundaries that are observable in images (a) and (b). The insets in (a-c) are close up views of the individual QDs that make up the hcp grains, as well as spatial Fourier transform images showing the hexagonal periodicity of the QD self-assembled monolayers. The QDs in this figure are 6.5nm diameter PbSe cores, prepared as described in the Experimental Section.

Cracking between the large area islands is likely due to the solvent drying process, as the optimal particle spacing for solvated QDs differs from the dry QD spacing.[99] In Figure 3-6 (d) the cracks are of nearly fixed width, suggesting that adjacent islands were once joined together. While solvent is still surrounding the QDs during the spin-casting process, they pack into hcp arrays with some natural period corresponding to the spacing of solvent rich QDs. At this stage, the surface coverage is probably very close to 100%, and the QDs have some freedom to minimize their surface free energy. As the solvent continues to evaporate, the QD spacing decreases, and the

QDs in a given grain pack closer together. At some point the continuous QD layer must break to allow for the strain that results from this higher packing density. The breaking is most likely to occur at a grain boundary, as the van der Waals interactions that are holding the QDs to their neighbors are weakest at this point of the film. The result is the large scale cracking morphology that we observe in Figure 3-6 (d), with the perimeters of adjacent islands tracking each other almost perfectly.

For quickly drying solvents, the cracks seem to be more numerous, but smaller in width, while for slowly drying solvents the cracks are less frequent, but larger. In all cases, the total area of void is approximately constant (22%, 20%, and 27% respectively for chloroform, mixed, and chlorobenzene solutions). This implies that the QDs are packing into their equilibrium, dry packing distance in all situations, an effect confirmed by directly measuring the QD spacing on the AFM images (periods of 8.3, 8.1, and 8.3nm were observed, respectively for chloroform, mixed, and chlorobenzene solutions). The tendency for slower drying solvents to yield larger cracks could be due to several factors. First, there are fewer grain boundaries available in this system, because of the larger mean grain size, and thus fewer sites where a crack could originate. The shrinking process is also occurring much slower in these films, allowing more time for the strain induced by shrinking to propagate to an existing crack, rather than nucleate a new one. Alternatively, the cracking could occur at many sites very early in the drying process, with the slower drying times allowing more time for the cracks to heal, and for islands to coalesce.

3.5 Observation of Two Dimensional Crystal Defects

The creation of large area two dimensional super-lattices of nanocrystals allows the direct observation of colloidal crystal defects. There are of course fundamental differences between this colloidal crystal system and a single crystalline semiconductor, or a molecular crystal. The size scale is larger, and therefore single elements of the crystal are more easily observed. In addition, we can tune this critical size by growing larger particles. Another major difference is that all of the units are not identical, with slightly different sizes, aspect ratios, and surface chemistry all affecting the process of crystallization. Finally, the energies involved are vastly different, with only van der Waals interactions playing a role. Crystal formation in the plane of a substrate in van der Waal bonded solids is not completely understood, indicating a potential benefit in using this system to study the kinetics of crystallization.

Figure 3-7 highlights crystal defects found in a QD self-assembled grain on an organic underlayer. Vacancies are manifested as dark spots in the AFM image of the hcp array (Figure 3-7 (a)). Interstitial defects are imaged as a rare high spot in the AFM height scan, roughly one QD diameter higher than the remainder of the periodic pattern. Line defects, where two rows of QDs merge and become one row, are frequently observed (Figure 3-7 (a)). Finally, the fine structure of the grain boundary itself is observable (Figure 3-7 (b)). It is simultaneously possible to measure the grain angle deviation of two grains joining, and to identify the location of each QD that makes up the boundary.

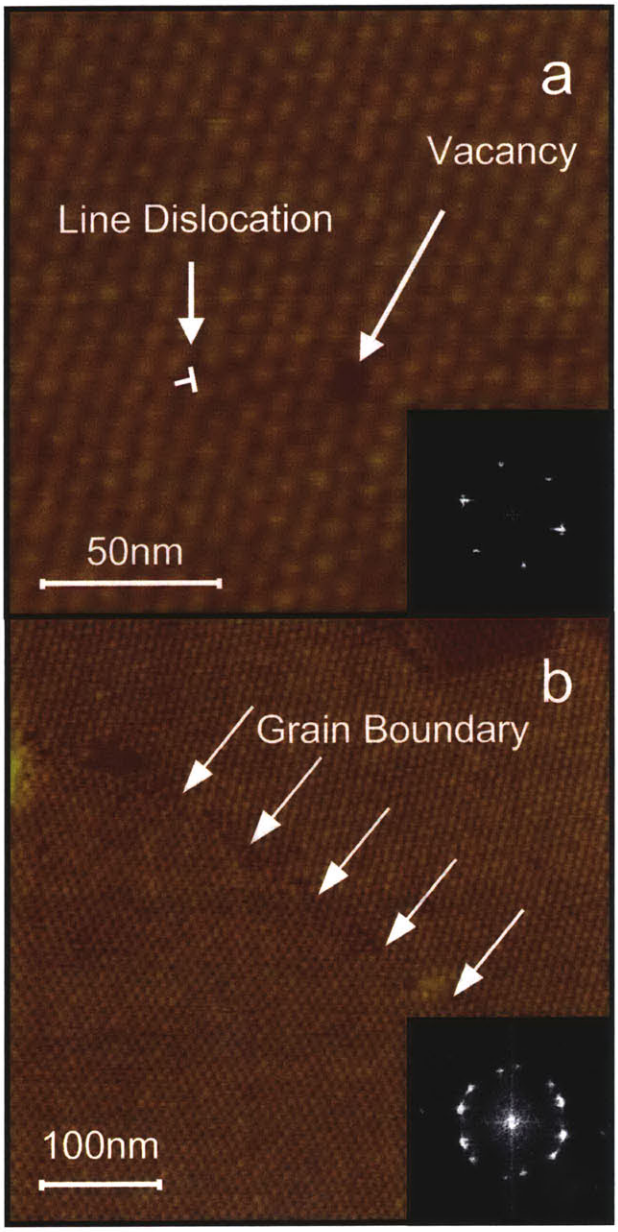

Figure 3-7: Crystal defects in two-dimensional QD colloidal crystals: AFM images of (a) a single QD grain, with crystal defect points clearly visible and (b) the grain boundary between two large area colloidal crystal grains, allowing the study of the individual QDs that make up the grain edges. Insets are the spatial Fourier transforms of the two images, in (a) showing the three-fold symmetry (six points) of the hexagonal periodic array, and in (b) showing the six points of each of the two grains, resulting in 12 clearly distinguishable points on the same diameter circle. The QDs in this figure are 5.5nm diameter PbSe cores, synthesized as described in the 3.9 Experimental Section.

3.6 Role of Organic Underlayer

Drying-mediated phase separation and self-assembly processes have recently received much attention in the literature,[62, 100, 101] though a detailed mechanism for the specific cases presented in this study are as yet unproven. During spin-casting, the organic/QD solution transitions from a homogeneous liquid mixture to a phase separated solid. It is unclear at exactly what point in time the separation occurs, a) early in the solvent drying, when the solute mass percent remains low or b) late in the process, when the solvent mass percent is low. The phase separation is driven by the minimization of interface surface energies. The organic small molecules are preferentially deposited on the substrate surface due to both their higher polarizability relative to QDs, and the higher contact area with a flat surface which they can achieve. The size of the QD units reduces both of these quantities relative to the small molecules.

Experiments in which the organic has been eliminated from the spin-casting solution demonstrate that one of the roles of the organic component is a simple surface modification; Pure QD solutions spun onto aromatic organic surfaces form monolayer films with hcp structure, while QD solutions spun onto silicon oxide form low coverage multilayers or sub-monolayers.[102] Another important effect of the organic is to slow down the evaporation of the solvent, allowing more time for the QDs to reach equilibrium on the surface. It is the combination of these two effects of the organic material that enable the monolayer formation and self-assembly to occur during the solvent drying time. Once phase separation has occurred, the QDs are mobile on the organic underlayer surface,[96, 103] and self-assemble into hcp arrays as they seek their equilibrium conformation, coarsening via a combination of Ostwald ripening[104, 105] and

cluster diffusion,[106] depending on the stage of coarsening and the initial QD concentration.

3.7 Light Emitting Devices

3.7.1 Visible

Figure 3-8 demonstrates the highest external quantum efficieny, η_{EX}>2%, quantum dot light emitting device (QD-LED) created to date. The layered device structure (Figure 3-8 a, inset) requires the use of a QD monolayer, which in this case is created using the phase separation technique. Holes and electrons are efficiently delivered to the active layers of the device to create excitons which recombine in the cores of the QDs. The electroluminescence (EL) spectrum (Figure 3-8 b, inset) demonstrates that the emission is dominated by QD band edge emission. Such a device is reported here to demonstrate both the utility of this fabrication technique, and the need for precise control of all aspects of the process, leaving device analysis for other works.[77] In such a device the underlayer becomes the hole transport layer, and the monolayer surface coverage and size distribution of the QD sample are directly related to the EL emission spectrum. The ability to use the phase separation technique on diverse substrates allows an indium tin oxide transparent electrode to be one contact of the device.

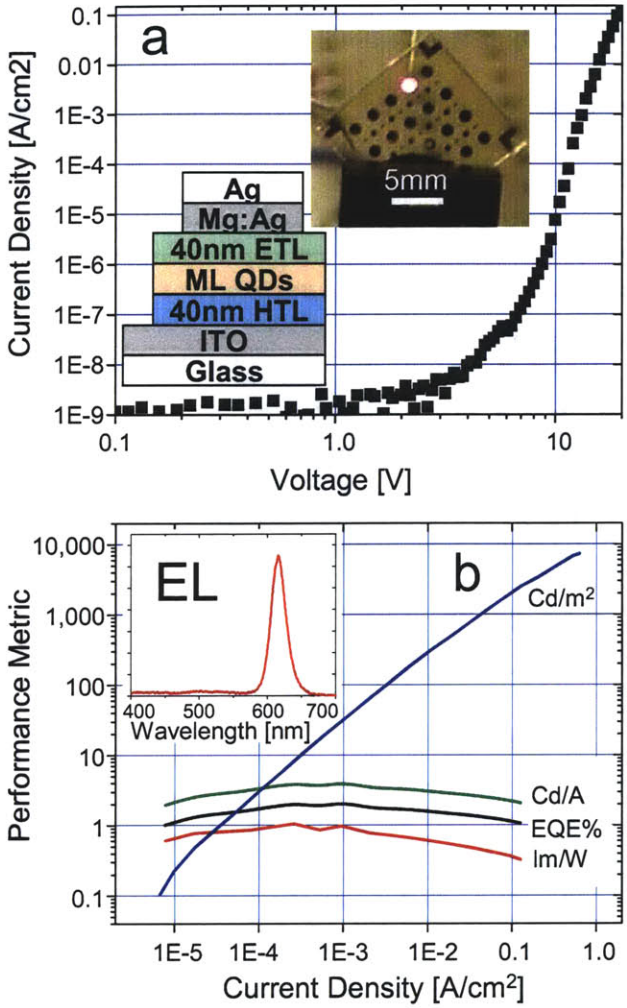

Figure 3-8: Structure and performance of a QD-LED fabricated using the phase separation during spin-casting method. a) Current-Voltage characteristic of the device; a, inset) Typical cross-section of an efficient quantum dot light emitting diode, and a photo of the operating 1mm diameter device; b) Critical performance metrics of the QD-LED, with external quantum efficiency in excess of 2%, > 1 lm/W, and a maximum brightness of over 7,000 cd/m2; b, inset) Electroluminescence spectrum of the QD-LED, with saturated color red emission peaked at 615nm, and FWHM of 27nm. In this device preparation we used overcoated CdSe QDs provided by Quantum Dot Corporation.

3.7.2 Infrared

Phase separation also enables the creation of infrared emitting QD-LEDs, utilizing PbSe core, oleic acid capped QDs. The electrical and optical characteristics of these devices are summarized in Figure 3-9. By changing the QD size the

electroluminescence is tuned from $\lambda = 1.33$ to 1.56 μm with a full width at half maximum of <160 nm (< 0.11 eV). This represents only a portion of the accessible QD tuning range, as the lowest energy optical absorption peak of our PbSe solutions can be tuned from 1.1 eV (corresponding to wavelength $\lambda = 1.1$ μm and 2.6 nm diameter QDs) to 0.56 eV ($\lambda = 2.2$ μm, 9.5 nm diameter).

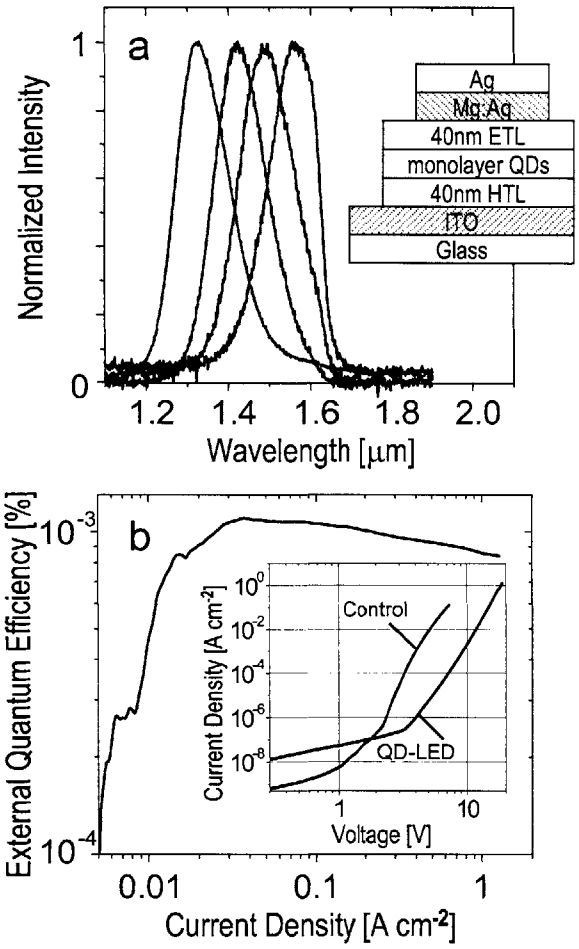

Figure 3-9: Device characteristics of infrared emitting QD-LEDs. The QDs in these devices are different sizes of PbSe cores with oleic acid caps, enabling (a) the continuous tuning of electroluminescence from 1.3μm to 1.55μm. In (b, inset) the current-voltage characteristics are shown relative to an all-organic control device, and (b) shows the external quantum efficiency versus current density for a typical infrared QD-LED.

Established technologies such as inorganic LEDs, lasers, photodetectors, and modulators have been developed and optimized in the near infrared (NIR) to address the needs of optical communications, chemical spectroscopy, and chemical sensing. These devices have high performance and long lifetimes, but the associated fabrication and material costs are high and therefore prohibitive for cost-constrained applications that require large area devices. New device paradigms that use less expensive fabrication processes and materials would enable the more widespread use of active NIR optoelectronic devices. Molecular and polymeric organics are among the materials that, in principle, meet these criteria, but as yet they are not readily available with efficient tunable emission beyond the wavelength of $\lambda = 1\mu m$, even when inorganic complexes are used as the emitter in doped organic structures[107, 108]. In this study we generate NIR electroluminescence (EL) by using inorganic PbSe nanocrystals in solution processible organic structures. Although our reported efficiencies are low, the demonstrated QD-LEDs are controllably tuned across the NIR spectrum and have the potential to be further improved based on the high solution PL efficiencies of the starting materials and our previous studies[73, 76] of efficient CdSe QD-LEDs.

The low η_{EL} of our devices is the result of the lowered quantum efficiency of films of close packed QDs and a device design that is optimized for visible emisison. While PbSe QDs have been shown to be very efficient NIR emitters in solution, the η_{PL} drops to 0.5 to 1.5% in thin film form. This is due to a reduction in the number of available capping molecules to the QDs in thin film form, as well as exciton energy transfer within the QD film, both of which have been shown to reduce η_{PL} in QD solids. Extrapolating from other QD material systems, it is reasonable to assume that the

development of a core-shell PbSe QD would result in higher solid state η_{PL}. Our active layer thickness and choice of organic semiconductors was originally designed for visible emitting organic LEDs. For the long wavelength devices described in this thesis, the optical mode overlap with the emissive QD layer is poor. Designs using a transparent highly conductive cathode would allow optimization of the distance between the metal and the emissive QD monolayer without incurring an increase in the operating voltage[83, 109]. We further note that the choice of ITO as the anode in our devices is not ideal, since the transparency of the 150 nm film is only 70% at $\lambda = 1.5$ μm.

Previous work has suggested that Förster energy transfer and direct charge injection are both potential mechanisms for QD excitation within QD-LEDs. (We find that radiative excitation of the QDs by green Alq_3 EL (spectral peak at $\lambda = 530$ nm) is a negligible source of QD NIR emission.) Exciton energy transfer should be possible for excitons created in the organic layer close to QDs despite the large capping group length (~1.8 nm). In contrast, photoconductivity experiments indicate that the 1.8 nm tunnel barrier is sufficient to reduce direct injection of charge carriers from the semiconducting organics into the QD core by several orders of magnitude relative to a QD capped with a shorter chain capping molecule[110]. For both mechanisms, however, shorter chain capping groups would serve to increase the likelihood of QD excitation. If we assume a Förster energy transfer process, the energy of the transferred exciton from Alq_3 molecules to QDs would initially be 2.4 eV (corresponding to the excited state of Alq_3). The generated QD exciton would then loose ~1.6 eV before occupying the lowest energy state from which QD emission originates. Since PbSe QD η_{PL} is constant over a wide range of

excitation wavelengths, PbSe QD-LEDs with higher power efficiency could be realized if organic transport materials with smaller optical gaps were utilized.

To accurately measure the efficiency and the EL spectrum of QD-LEDs it is necessary to maximize the detected NIR emission and attenuate the emission signal of both organic and blackbody radiation by using appropriate spectral filters, detectors, and detection geometry[111]. In our quantum efficiency measurements, the NIR signal (1-50 nW) is maximized by using a minimum distance between the emitter and a large area detector (3 mm distance, 3 mm diameter Newport 818-IR-C/M Germanium detector). The spectral measurements were performed using an InGaAs photodiode array cooled to 173 K (Roper Scientific OMA V) and monochromator with a fiber bundle input. The fiber bundle was coupled to the device substrate to maximize the input signal. For both efficiency and spectral measurements, the visible emission is filtered out using a double sided polished, 500 μm thick, Silicon wafer. The three lowest order diffraction peaks of Alq_3 (at λ = 530 nm, 1060 nm, and 1590 nm) that are otherwise detected by the spectrograph are completely eliminated when the Si filter is in place. Finally, the possible detection of blackbody radiation must be accounted for. Our 1 mm diameter devices were run at currents as high as 10 mA and 20 V operating voltages, corresponding to 200 mW of peak input electrical power. The power efficiency of these devices is no better than 0.1%, implying that 99.9% of the input power is converted to heat[112]. While a large portion of this heat will be lost to the surrounding air by conduction and convection processes, there is no doubt that some device and substrate heating to above room temperature does occur. Blackbody radiation at 300 K to 350 K has the bulk of its emission in the λ = 17 μm range, but a measurable quantity of emission

is in the λ = 1.1 μm to 1.7 μm detection window of Ge and InGaAs detectors. Our actual detected power in this spectral window was in all cases greater than 1 nW. A temperature rise of 70°C over the 150 mm^2 area of our substrates would be required to generate 1 nW of power in the spectral detection window. Our device could not support such a rise as the glass transition temperature of TPD is 65°C[113]. Furthermore, substrate inspection indicates that QD-LEDs are not warm to the touch during operation. A temperature rise of less than 10°C corresponds to <20 pW of detectable radiated power, and thus a <2% error in measurement of QD-LED NIR η_{EL}. This analysis shows that the detected power is therefore not a result of either blackbody radiation or visible organic EL, and is in fact due to the band edge emission from the QDs.

In conclusion, we demonstrate large area NIR EL from QD-LEDs. The LED emission is tuned from λ = 1.32 to 1.56 μm as the PbSe QD diameter is changed from d_{CORE} = 4 to 5 nm, without any modification to the device structure. Processing of the colloidally grown semiconductor QDs and the organic small molecules from the same solvent allows for the simple fabrication of double heterojunction devices, where the NIR emissive layer is only one monolayer thick. Using CdSe QD-LEDs as a model, we expect significant improvement of PbSe QD-LED performance through both device engineering and chemical optimization of the materials.

3.8 Conclusion

The fabrication of QD/organic bilayers via phase separation during spin-casting is a robust and general process. It has already been shown to be a useful technique for the creation of new optoelectronic device structures, enabling the creation of high efficiency QD-LEDs. In addition to the creation of single monolayers of QDs on top of organic

semiconductor contacts, this process enables the creation and study of large scale hcp crystal (super-lattice) domains of only two dimensions, which may be fabricated in seconds. The size scale of these domains is controllable, with a demonstrated maximum grain size in excess of a square micron. The upper limit of the grain sizes that could be formed certainly has not yet been reached. The facile assembly of large area arrays of nanoscale active elements, enabling the creation of macro scale devices from nanoscale materials, is an essential step to transitioning nanoscience into nanotechnology.

3.9 Experimental

3.9.1 Phase Separation

A known quantity of the organic material is weighed out dry, solvated in the chosen solvent, and stirred until completely dissolved. Some quantity of QD solution is then added, to yield both the desired organic to QD ratio, as well as overall concentration of solution. For example, in the bilayers used in Fig. 4(a), the final solution contained 10mg/mL of N,N'-diphenyl-N,N'-bis(3-methylphenyl)-(1,1'-biphenyl)-4,4'-diamine (TPD), and 9mg/mL of QD sample solid dissolved in chloroform. For simplicity and reproducibility all of the QDs are handled as stock solutions. The final concentration of particles in the spin-casting solution is determined by accurately measuring out a volume of this QD stock into the already prepared solution of organic small molecules. This mixture is then spin-cast onto a substrate. The entire substrate surface must be wetted by the solution before spin casting begins. The separation process is observed for a wide range of spin-casting parameters such as speed, acceleration, spinning time, and atmosphere (gas, temperature, solvent content). For the best control and consistent reproducibility of bilayers, we use a single spin speed (3000 rpm), a maximum starting

acceleration (10,000 rpm/s), and a long spinning time (60s) to insure complete evaporation of all solvent. Film properties can then be tuned by changing the solution composition.

3.9.2 Quantum Dot Clean-up Procedure

The QD growth solution is purified by solvent precipitation twice before spin casting. A typical procedure is to a) crash the QDs out of growth solution using an incompatible solvent b) centrifuge c) pour off supernatant d) rinse with incompatible solvent e) redisperse in compatible solvent f) crash out with incompatible solvent g) centrifuge h) decant supernatant i) rinse with incompatible solvent j) decant k) redissolve in compatible solvent l) filter m) pull vacuum on solution until completely dry n) redisperse in spin casting solvent to make stock solution.

3.9.3 Monodisperse PbSe Quantum Dot Synthesis

A solution of 1mmol of lead acetate trihydrate (Aldrich, 99.99%) and 2mmol of oleic acid (TCI America, 99%) in 12 mL of trioctylphospine (TCI America, run once through a column of basic activated aluminum oxide) is degassed for 2 hours at 300-500 mTorr and 100-120°C. 5mL of 1M trioctylphospine selenide is injected at 140°C and grown for 4.5 min while the temperature is ramping back up to ~140°C. After the growth time, the heating mantle is removed, allowing the solution to cool to room temperature. See Fig. 9 for absorption and emission spectra of such a QD preparation.

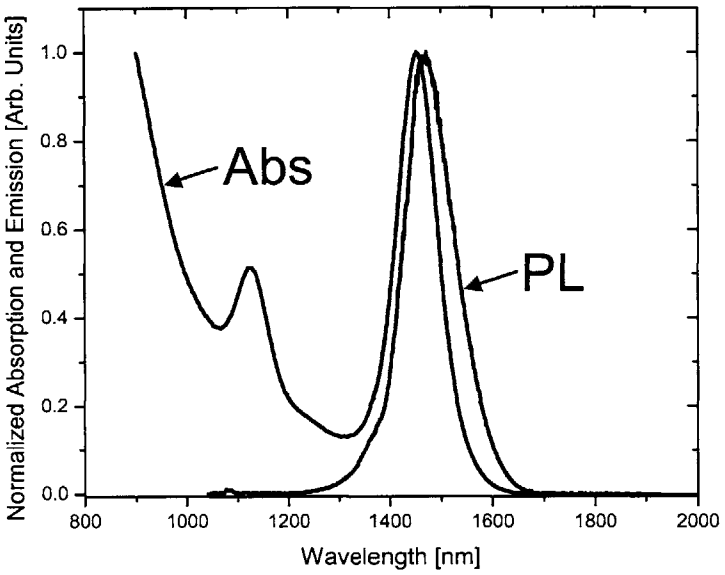

Figure 3-10: Absorption and photoluminescence (PL) emission spectra of a typical PbSe oleic acid capped QD sample (core diameter is 5.0nm in this example) prepared by the route detailed in the Experimental section of this work. The PL full width at half of maximum is 115nm (66meV), peaked at wavelength λ = 1470nm. The first absorption feature peaks at λ = 1452nm.

4 Micro-Contact Printing

The previous chapter detailed a fabrication method enabling the formation of large area monolayers of colloidal QDs self-assembled onto organic semiconductor surfaces. This fabrication is robust in many ways, but does not allow for the lateral patterning of such monolayers, a critical component in making QD-LEDs a viable display technology. In this chapter, the technique of QD micro-contact printing is discussed, enabling the creation of three color QD-LED substrates for the first time. Subsequent chapters will then discuss QD-LED device operation, pathways to commercialization, and future research directions.

4.1 Introduction

Semiconductor nanocrystals (quantum dots, QDs) which are highly monodisperse, photoluminescence efficient, and emission wavelength tunable can be seen as an ideal lumophore for the creation of light emitting devices for almost any application. Such QDs are solution processable, and hence compatible with thin-film deposition techniques such as spin-casting, drop-casting, and dip coating. However, QD solids have poor electrical transport properties in solid state devices, inspiring the use of single monolayers of QDs in active devices so as to utilize their beneficial light emission properties while minimizing their impact on electrical performance. Such QD monolayers are typically self assembled out of solution, either by spin-casting, Langmuir-Blodgett techniques, or drop-casting. However, these assembly techniques place requirements on the substrate onto which the monolayer is deposited, and do not allow the QD monolayer to be laterally patterned. These two traits make the available techniques far from ideal for assembly of multiple color LEDs onto the same substrate, or

for device engineering. To solve both of these problems we have extended the method of micro-contact printing to QD monolayer deposition. This chapter describes the micro-contact printing of QD monolayers, utilizes these monolayers in making saturated color red, green and blue QD-LEDs, demonstrates placing multiple QD-LEDs of different colors onto a single substrate, and demonstrates the micron scale (<100μm) patterning of QD-LED pixels via this micro-contact printing technique. This represents the first use of micro-contact printing of QDs in the creation of electroluminescent devices, towards the realization of QD-LED full color displays.

Much work has been dedicated to the assembly of large area monolayers of QDs. All of these techniques either place constraints on the substrate used[62, 67], require the addition of chemicals that effect the electrical or optical properties of the layer[59, 62], or subject the substrate to harsh conditions[64]. Hence, adapting any of these techniques to the creation of active electrical devices such as QD-LEDs would require the device to be designed around the deposition technique, leading to non-ideal structures and therefore performance. In addition, once such a device is fabricated a method for the in-plane patterning of adjacent devices is necessary for creation of three color displays from QD-LEDs. Some initial work has been done on patterning of QD layers as well[65-67, 114, 115], but has not been integrated into a device fabrication procedure. Our approach is to develop a technique for the patterning of such QD monolayers while simultaneously allowing for as much flexibility in device design as possible. Indeed, the ideal QD fabrication technique would involve the dry (solvent free) application of an already patterned QD film to any substrate, removing all solubility and surface chemistry

requirements on the substrate which are typical and to some extent assumed within the field.

4.2 QD Micro-Contact Printing Process

Figure 4-1 depicts a flow chart outlining the basic steps in the process. First, a silicon master is made using standard semiconductor processing techniques (alternatively, for a non-patterned deposition, a blank Si master can be used). Poly dimethyl Siloxane (PDMS, Sylgard 184) precursors are then mixed, degassed, poured onto the master, and degassed again, and allowed to cure at room temperature (or above room temperature, for faster cure times)(Figure 4-1, step 1). The PDMS rubber "stamp" is then freed from the master, and cut into the desired shape and size. This stamp is then coated with a chemical vapor deposited Parylene-C layer, anywhere from 0.1-2μm thick, depending on the pattern to be reproduced (Figure 4-1, step 2). This stamp is then inked through a simple spin-casting of QDs in a solution of chloroform (concentration 1-10mg/mL depending on desired outcome) (Figure 4-1, step 3). The inked stamp can then be inverted onto a substrate, and with gentle pressure applied for 30 seconds, the ink will transfer completely to the new substrate (Figure 4-1, step 4). Figure 4-1 (a,b) depicts an ITO coated glass substrate, which has already had hole tranport and/or hole injection organic semiconductor layers (HTL and HIL respectively) thermally evaporated on top of it. The patterned QD monolayer is transferred to this HTL layer, and the rest of the device (electron transport layer (ETL), electron injection layer (EIL), metal contacts) can then be grown on top of the QDs (Figure 4-1, step 5).

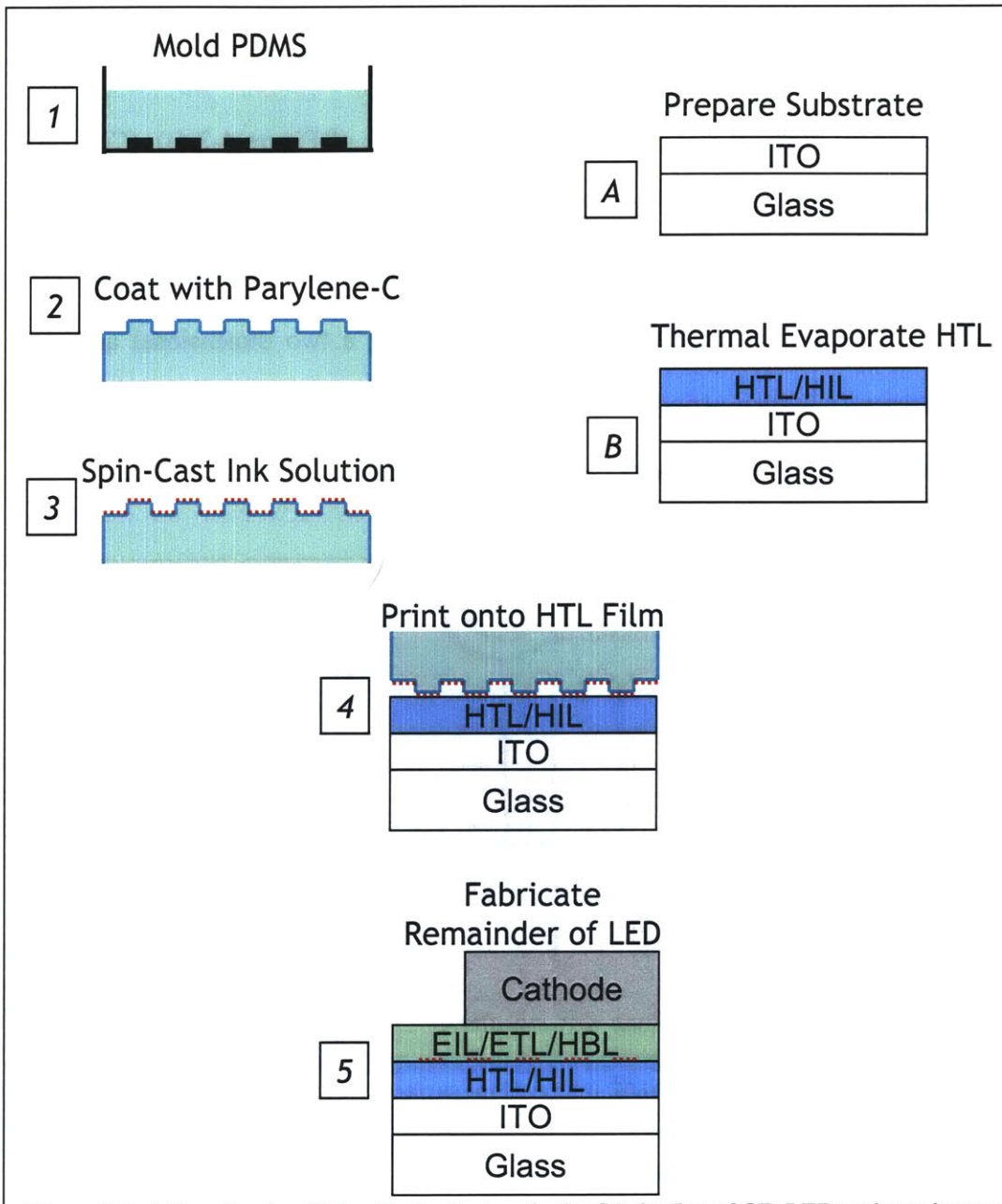

Figure 4-1: A flow chart outlining the basic steps in the fabrication of QD-LEDs using microcontact printing of QDs. First, a silicon master is made using standard semiconductor processing techniques, which is then transferred to PDMS (step 1). The PDMS rubber "stamp" is then coated with a chemical vapor deposited Parylene-C layer (step 2). The stamp is then inked through a simple spin-casting of QDs in a solution of chloroform (step 3). The inked stamp is then inverted onto the ITO coated glass substrate (step A), which has already had hole tranport and/or hole injection organic semiconductor layers thermally evaporated on top of it (step B). The ink (QDs) is transferred completely to the new substrate (step 4) and the rest of the device (electron transport layer, electron injection layer, metal contacts) is then grown on top of the QDs (step 5).

Figure 4-2 demonstrates the surface relief that is observable through atomic force microscopy (AFM) after the stamping process. In the case of Figure 4-2 (a), (CdS)ZnS QDs are deposited using a planar stamp with submonolayer QD coverage, onto a TPD surface. Figure 4-2 (b) shows the result of using PbSe QDs with a patterned stamp. The master is created using interference lithography, yielding a two dimensional array of 150nm features on a 300nm period in both dimensions. This pattern is then replicated on the stamp, and finally on the QD layer transferred onto silicon.

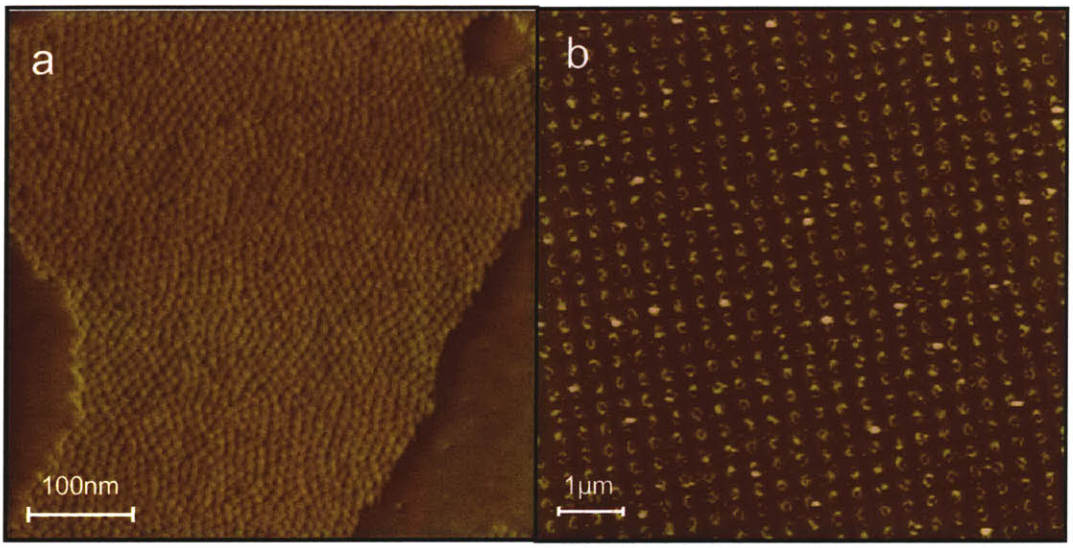

Figure 4-2: Atomic force microscopy (AFM) images of the surface relief that is observable at step 4 of Figure 4-2. a) shows the QD monolayer after transfer onto an organic semiconductor surface, using an planar (not patterned) stamp. b) shows the partial QD monolayer resulting from transfer onto a Silicon surface using a patterned (150nm circular features on a square grid) stamp.

4.3 QD-LEDs via Micro-Contact Printing

Figure 4-3 shows the optical device characteristics for the red, green, and blue QD-LEDs fabricated using our QD microcontact printing technique, while Figure 4-4 shows

the electrical performance of the same devices. Red, green, and blue emitting QDs were all printed onto a thermally evaporated thin film of 4-4'-N,N'-dicarbazolyl-biphenyl (CBP) (HTL). The QD deposition is followed by the deposition of the hole blocking layer (HBL) 3-(4-Biphenylyl)-4-phenyl-5-tert-butylphenyl-1, 2, 4-triazole (TAZ) and the ETL, tris-(8 hydroxyquinoline)aluminum (Alq_3), and finally an evaporated Mg:Ag/Ag cathode (50:1 Mg:Ag by weight).

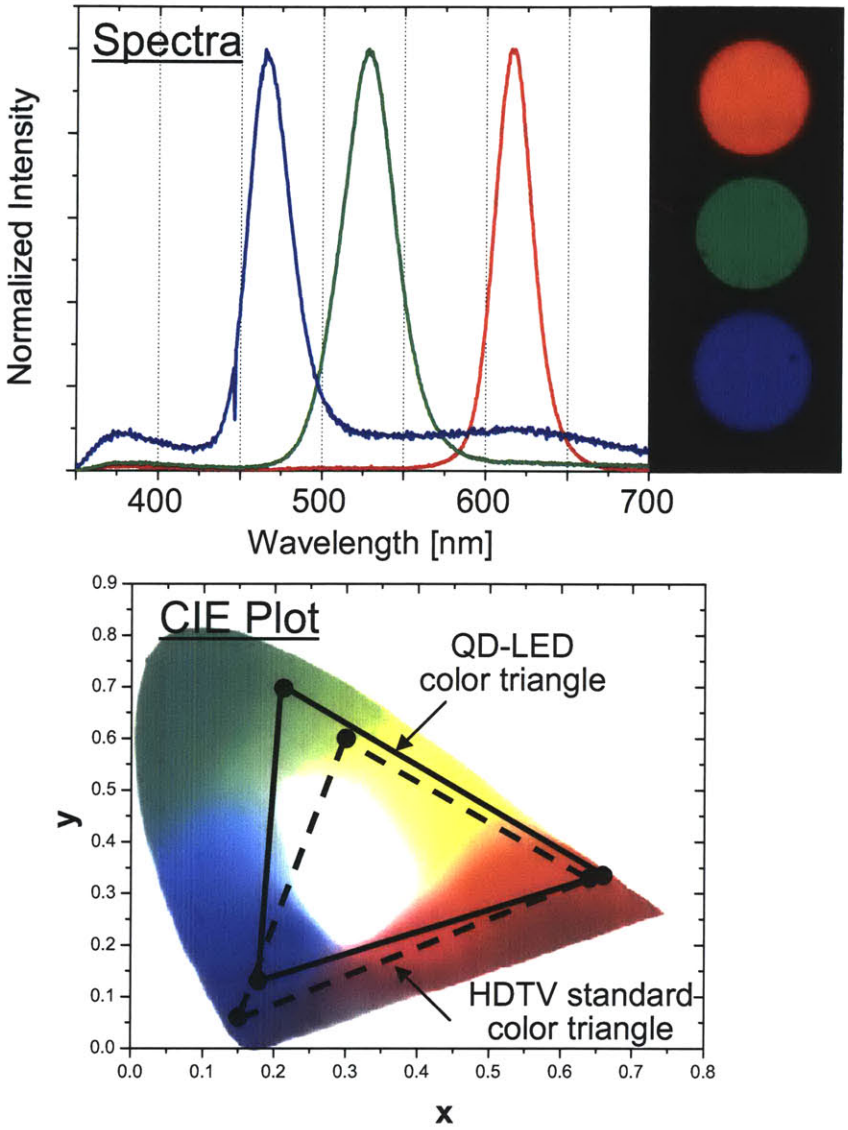

Figure 4-3: Red, green, and blue emitting QD-LED device luminescence characteristics. The normalized electroluminescence spectra of red, green, and blue QD-LEDs are shown (top) alongside digital photographs of individual pixels emitting their characteristic light color. The colors of the lines in each plot correspond to the color of light that the device is emitting. The CIE Chromaticity Diagram (below) shows where those colors being emitted by the respective devices show up on the relative to the HDTV standard color triangle. The triangle described by these three QD-LED vertices encompasses 1.3 times the area of the HDTV standard color gamut.

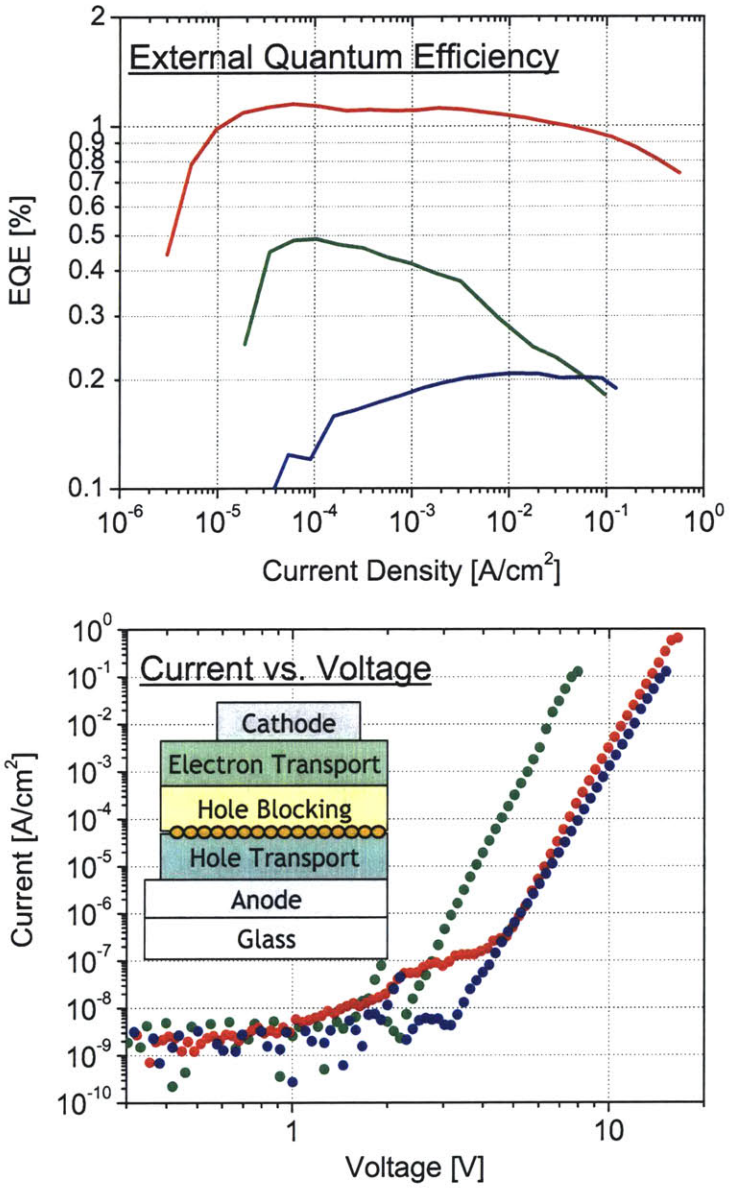

Figure 4-4: Electrical performance data of the same micro-contact printed QD-LEDs as shown in Figure 4-3. Again, the colors of the lines in each plot correspond to the color of light that the device is emitting. The top plot shows external quantum efficiency versus current data, showing trends similar to those of OLEDs. The current-voltage curves below are show the turn-on voltage of each of the devices to be between 2 and 5 volts. The inset shows the device structure as fabricated in all three colors of QD-LEDs.

4.4 Discussion

The ability to now separate the deposition of the organic HTL/HIL from that of our QD monolayers has allowed us to explore the use of other molecules for the HTL/HIL and as a result led us to the large band gap organic semiconductor, CBP. Our previous work on QD-LEDs employed the use of N,N'-diphenyl-N,N'-bis(3-methylphenyl)-(1,1'-biphenyl)-4,4'-diamine (TPD) as the HTL, simply due to its good solubility in chloroform and chlorobenzene compared to many other HTL candidates. We have found that the larger band gap CBP molecule produces far better color saturation in our devices as can be seen in Figure 4-3. Color saturation refers to how pure a color appears to the human eye and is quantified in the Commission International d'Eclairage (CIE) Chromaticity Diagram, shown in Figure 4-3(bottom), by calculating coordinates on the CIE diagram based on the emitters wavelength and bandwidth (full width at half maximum). The greater color saturation could be attributed to the larger downhill energy transfer process now available with the use of CBP[116, 117], which results in a decrease in the intensity of organic emission and an increase in intensity of QD emission, leading to the larger ratio between the QD electroluminescence (EL) and organic EL. The observed increase in ratio of QD EL to organic EL in our devices is also due to the ever increasing photoluminescence (PL) quantum efficiencies of the QDs themselves. Over the past decade the chemistry of QD synthesis has developed dramatically with PL quantum efficiencies approaching 80 to 90%, and because there is no fundamental reason limiting their quantum efficiency it will likely approach unity within the next 5 years. The superior color saturation of our red and green QD-LEDs is represented by their position on the CIE diagram relative to the current High Definition Television (HDTV) standard color triangle as seen in Figure 4-3. The blue QD-LED CIE color coordinates lie just

inside the HDTV standard color triangle and is a result of the red tail seen in the blue QD-LED EL spectrum. This red tail we believe is the result of a mixed state between the two large band gap HTL and HBL (exciplex emission) in our device structure. An exciplex is a transient complex formed between the excited state of a donor molecule and the ground state of an adjacent acceptor molecule. This exciplex emission is not seen in the red QD-LED device most likely because those energy states from the exciplex are Förster energy transferred to the red emitting QDs. The green QD-LED exhibits only a very small amount of this exciplex emission probably due to the excellent film coverage of the monolayer of green emitting QDs, which separates the HTL from the HBL and therefore their interaction, as well as the high PL quantum efficiency (40%) of the QDs themselves, which contributes to the large QD EL intensity relative to the organic exiplex EL. Another contributing factor is that when the devices are run at high currents (~100uA) the exiplex emission peak shifts from ~620 nm to ~ 520 nm, which is right over the green QD emission peak and is either covered completely by the green QD emission or is Förster energy transferred to the green emitting QDs. The blue QD-LED devices will improve as the blue emitting QD PL quantum efficiency increases (currently 20%). Figure 4-4 shows the external quantum efficiency (EQE) of our red, green, and blue QD-LEDs and demonstrates how the EQE of our devices scales with the PL quantum efficiency of our QDs. Currently our red EQE is 1.2% using QDs with PL quantum efficiencies of 70% after processing and preparing for device use (as described in 3.9.2 Quantum Dot Clean-up Procedure, above), our green emitting QD-LEDs have EQEs of 0.5% using QDs with PL quantum efficiencies of 40%, and our blue EQE is 0.25% using QDs with PL quantum efficiencies of 20%. All three color QD-LEDs have

reproducible and stable current-voltage (IV) characteristics, with turn on voltages of between 2-5 volts and operating voltages of 8-12 V as seen if Figure 4-4. Display brightness (100 Cd/m^2) is achieved at ~2 mA/cm^2 and ~10 V for these QD-LEDs.

The continuous tunability of QD emission wavelength allows us to fine tune the color of QD-LEDs. In the design of red, green, and blue devices, we assume an application to visible displays where color saturation is of importance. Thus, we choose center wavelengths for the QDs in each device to maximize the lumens per optical Watt of the emission spectrum while maintaining the color saturation in excess of the current National Television System Committee (NTSC) standard color triangle. The appropriate choices are 470nm, 530nm, and 610nm for blue, green and red QD-LEDs, respectively.

The most promising result of this QD micro-contact printing technique is the ability to place different color emitting QDs on the same substrate in a pattern towards pixilation for full color display applications. Sub-pixel dimensions for full color displays are typically on the order of 25-100 μm. Here we demonstrate that this technique enables patterned QD-LEDs with 25μm line widths (though Figure 4-2(b) allows us to project this dimension to be much smaller in the future). Figure 4-5(a) shows the result of stamping an area of green emitting QDs next to an area of red emitting QDs on the same ½ inch substrate. The three devices that have been turned on in Figure 4-5 are adjacent red and green emitting devices as well as a device on an area where no QDs have been stamped (ITO/CBP/TAZ/Alq_3/Mg:Ag/Ag organic LED). Figure 4-5(b) demonstrates the real potential of this technique to achieve less than 25 μm patterning toward pixilation for QD-LED displays. Here red emitting QDs have been printed using a stamp that was patterned with lines having dimensions of 2 μm in height and 25 μm line widths on a

50μm pitch. The size of the device that has been turned on is 1 mm in diameter and the red lines that lie within this device are the 25 μm patterned red emitting QDs.

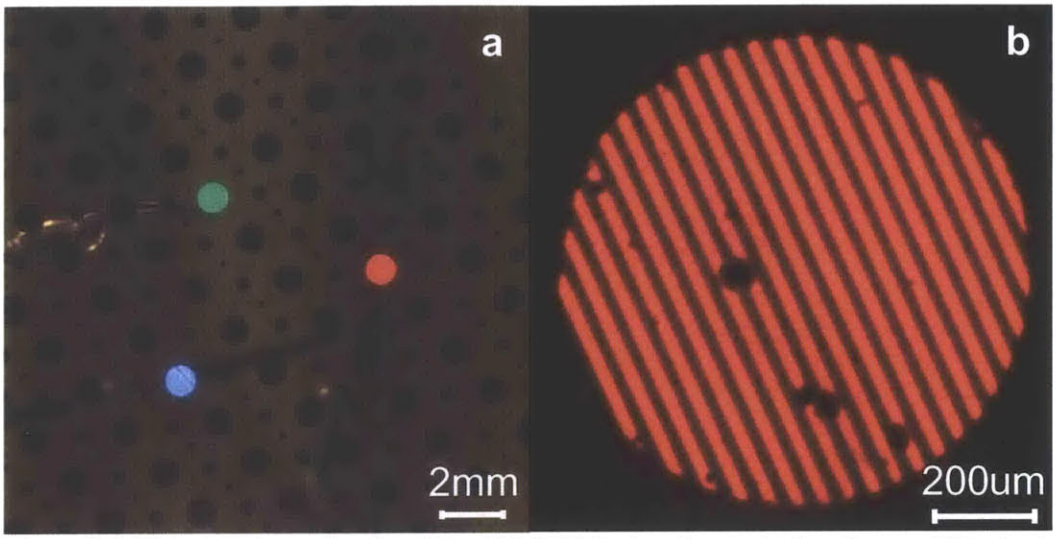

Figure 4-5: Digital photographs of working QD-LED devices demonstrating the capability to stamp different color emitting QDs on the same substrate and pattern the monolayers of QDs as well through the use of microcontact printing. a) Two adjacent areas on the same substrate were stamped with a monolayer of red and green emitting QDs and three different devices were turned on, a device made over an area where red QDs had been stamped, a device over an area where green QDs had been stamped and a device over an area where no QDs had been stamped (emitting blue). The dark circles in the image are the cathodes of LEDs which do not have any bias applied across them, and hence are not actively emitting any light. b) A device area was defined by the size of the cathode (1 mm in diameter) and within that area a layer of red emitting QDs was deposited. Red light can be seen emitting from the pattern in which they were stamped (25 μm width lines, on a 50μm pitch).

4.5 Conclusions

In conclusion, we demonstrate red, green, and blue emitting QD-LEDs that are efficient, with high color saturation compared to organic LEDs and liquid crystal displays, and which can be patterned towards pixilation for full color display applications by means of micro-contact printing of single layers of nanocrystals. The use of micro-contact printing of nanocrystals to fabricate LEDs shows tremendous potential in becoming a next generation flat panel display manufacturing technology. It is inherently

simpler than both inkjet printing and contact shadow masking, has the potential to be efficient in materials usage and to scale easily to large area batches and continuous roll-to-roll processing.

5 Device Operation

The previous chapters described two novel QD thin film fabrication methods, enabling the formation of QD-LEDs with high color saturation and quantum efficiency. In this chapter, we explore the details of QD-LED operation. While there is no definitive proof of the operating mechanism of our QD-LEDs, the series of experiments below give us insights into device operation, and suggest steps that can be taken to further optimize performance. Subsequent chapters will discuss such future directions for QD-LED research, as well as the commercialization potential of QD-LED displays.

5.1 Exciton recombination zone width

In exploring QD-LED device operation, we must start with a few simple assumptions. For uniformity of argument, we first define the QD-LED device structure which we will analyze (see Figure 5-1(a)). The primary simplification here is the removal of the TAZ or hole blocking layer. In general, devices which include this layer will have similar operation, with exciton generation and recombination occurring at the HTL side of the heterojunction rather than on the ETL side. Second, we propose a band diagram of this device structure as depicted in Figure 5-1(b). Literature values can be used for the organic thin films as determined by experiment, as well as for the QD monolayer as determined by calculation, though the error in all such techniques is on the order of a few hundred meV (0.1-0.3 eV). Additionally, we note that the conduction electron affinity of the CdSe QD will be dependent on core diameter, giving rise to a 300meV range for this value for tuning from green to red. We can then assume that charge conduction through the organic thin films proceeds as in the absence of the QD

monolayer (charge hopping mechanism, trapped-charge limited space-charge conduction[86]), and focus on the role of the QD monolayer in conduction, exciton formation, exciton diffusion, and emission.

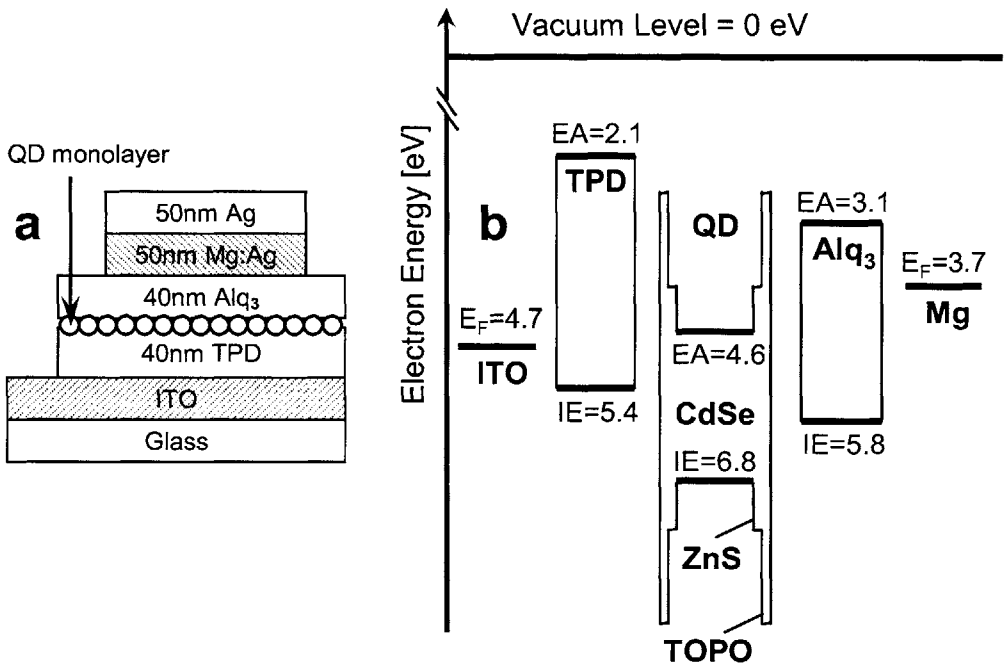

Figure 5-1: Archetype QD-LED device structure, and proposed band diagram showing electron affinity (EA) and ionization energy (IE), or Fermi levels (E_F) for each of the layers that comprise the device. All values are taken from the literature, based on experimental data for the organic thin films[118] and calculations for the QD values[69].

Figure 5-2(a) shows the EL spectra of different QD-LEDs operated at low current density (0.38-13 mA/cm^2, Figure 5-2 (a)). The spectra demonstrate our ability to fabricate devices using the phase separation technique which yield highly monochromatic EL that is tunable from 540nm to 635nm, corresponding to the PL spectrum of each (CdSe)ZnS QD starting solution. The EL of these devices has greater than 70% QD emission. The remaining organic (Alq_3 or TPD) EL is due to the presence of voids, grain boundaries, and interstitial spaces in the QD monolayers that allow the creation of

excitons on organic sites as depicted in Figure 5-3. For example, excitons generated in region A, deep within the electron transporting layer, are more than the Förster energy transfer radius (R_F) away from the nearest QD, resulting in organic EL. Similarly, excitons in region B, within the monolayer void, will result in organic EL.

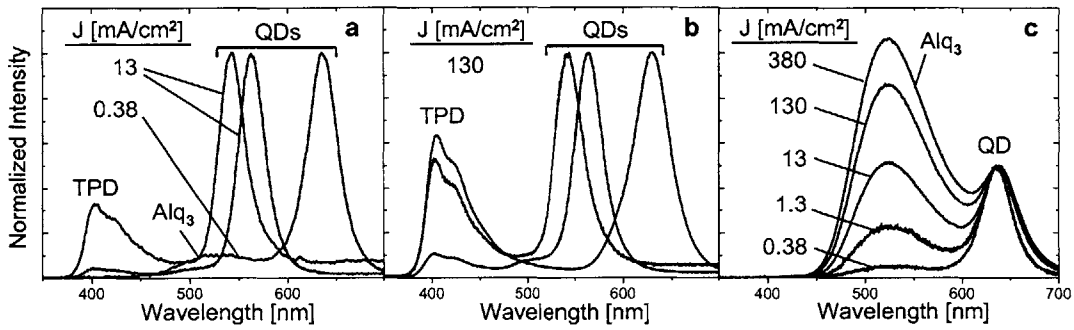

Figure 5-2: Typical normalized QD-LED electroluminescence spectra of three different sized QD samples measured at (a) low current levels (0.38-13mA/cm2), where most (>70% in all cases) of the emission is from the QDs in the device, with only small spectral contributions from either Alq_3 (when TAZ layer is omitted) or TPD (when TAZ layer is present) (b) moderate current levels (130mA/cm2), where two of the three spectra have a large fraction of EL from TPD (c) and a progression of currents for a single device (from 0.38mA/cm^2 to 380mA/cm^2). Note that the devices emitting at 540nm and 560nm are the same in 4(a) and 4(b). At low currents, a larger portion of the excitons are created within a Förster energy transfer radius of the QD monolayer. For all devices, $0.2\% < \eta_{EL} < 0.5\%$.

Figure 5-2 (b) shows the EL spectra of QD-LEDs operated at higher current density (130 mA/cm^2). Comparing to Figure 5-2 (a), it is clear that the fraction of emission coming from organic lumophores has increased. Figure 5-2 (c) demonstrates this same effect for a single QD-LED operated over 3 decades of current densities, from 0.38 mA/cm^2 to 380mA/cm^2. This change in ratio of QD to organic EL signifies a notable change in the exciton generation process.

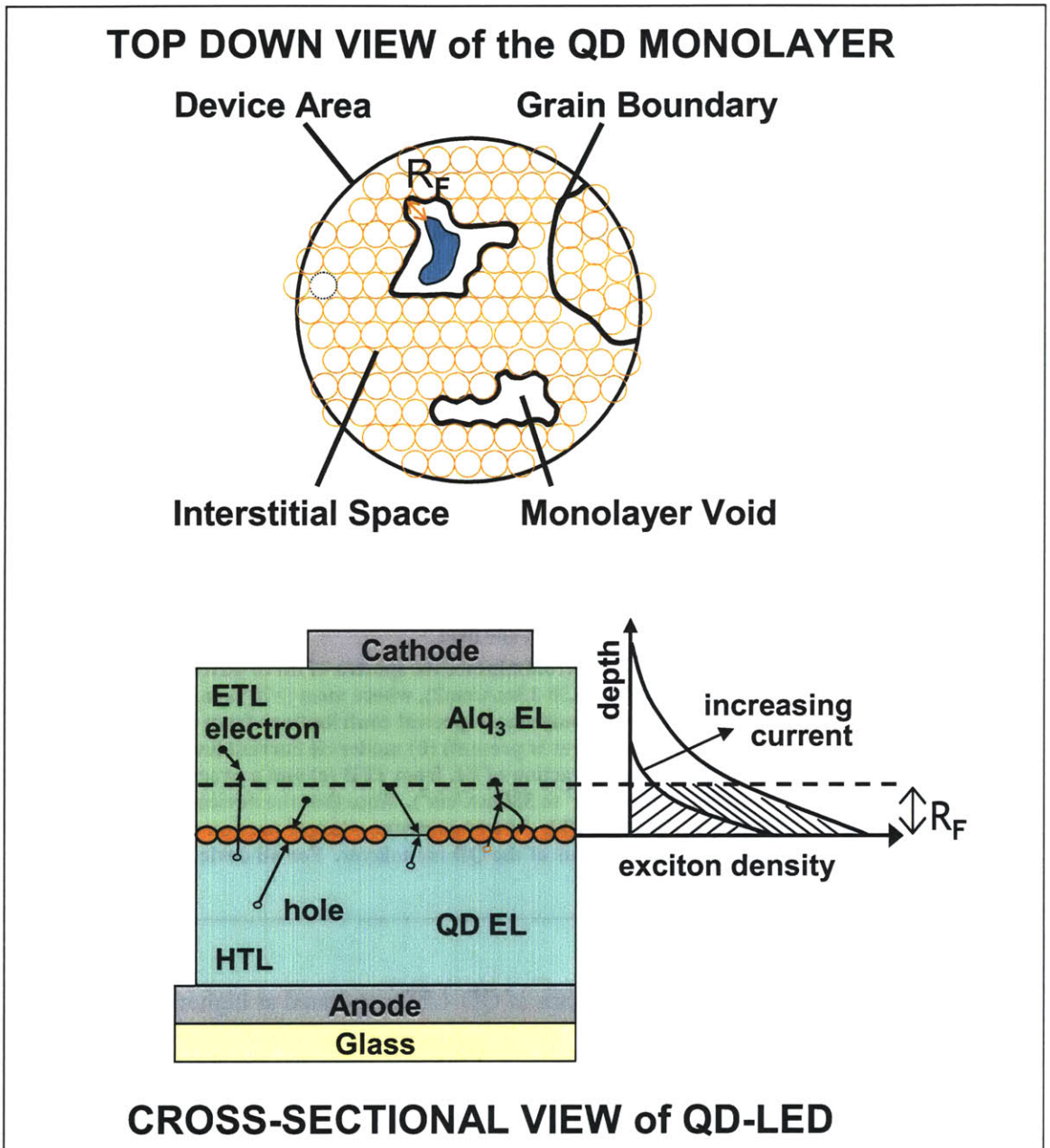

Figure 5-3: Graphic representation of exciton generation process within the QD-LED structure. At high currents the width of the exciton generation region is expected to exceed the organic-QD Förster energy transfer radius (R_F) (region *A* in the figure), resulting in an increased contribution of organic (Alq_3 or TPD) luminescence to the EL spectrum. Excitons created at voids (region *B* in the figure), interstitial spaces and grain boundaries of the QD monolayer may also be farther than R_F away from the nearest QD.

In section 2.3 we noted that EL is generated by either direct injection of holes and electrons into the QDs or by the Förster energy transfer of excitons onto the QDs from

the neighboring organic molecules of higher exciton energy (note that the PL of TPD and Alq_3 overlaps with the absorption spectra of all QDs in this study). In the energy transfer picture (see Figure 2-4) we can attribute the organic emission to the recombination of excitons in the organic molecules which are at a distance $>R_F$ from the nearest QD. Therefore, at lower currents, either all excitons have energy transferred from organic molecules to QDs, or alternatively, they are initially formed by direct charge injection on the QD sites. We note that at the current density of 130 mA/cm^2, at most 10^6 electrons per second arrive at each QD site so that the rapid QD exciton relaxation (thin film CdSe QD exciton lifetime $\tau_{QD} < 30$ ns [119]) keeps the QD exciton density at <1%. Such a low QD exciton population should not modify the organic-QD exciton transfer rate, and consequently the change in the QD emission fraction with current is attributable to a change in the exciton recombination region width.

Following an earlier study[120] we suggest that the exciton recombination region of QD-LEDs broadens with increasing current, which we confirm by using an archetype OLED system, DCM2 doped into a TPD/Alq_3 structure. The OLED cross-section is shown in Figure 5-4(a), with the red laser dye DCM2 used in place of QDs. The dye is doped at low concentration (2% by weight) in a 5nm thick Alq_3 layer, to closely model the thin two-dimensional QD sheet that makes up the emissive layer of the QD-LED structures. With this device we can study the performance of a very thin and extensively characterized lumophore layer, eliminating QDs as a performance modifier. The spectral dependence on current density is then measured over 4 decades of current. From the normalized EL spectra in Figure 5-4(b) it is clear that the ratio of Alq_3 to DCM2 emission rises with increasing current density. The observed changes in Figure 5-4 are consistent

with the spectral changes of the QD-LED in Figure 5-2 (c). Equivalently, the organic emission in the QD devices is a consequence of the very thin QD lumophore layer, suggesting the need for better confinement of excitons near the QDs. To date, however, fabrication of an effective exciton confinement structure has been complicated by the difficulty in depositing a uniform thin (<10nm) aromatic film on top of an alkane capped QD monolayer, as morphological studies have explored[76].

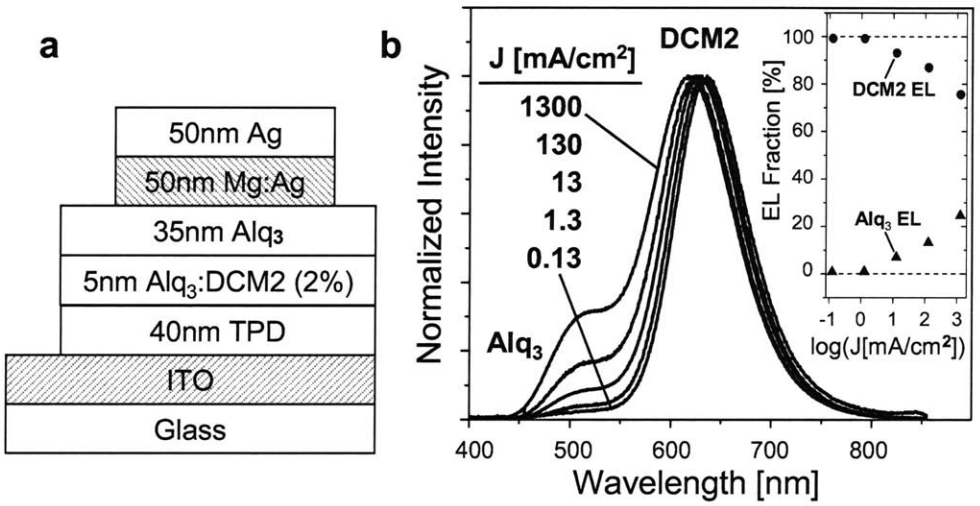

Figure 5-4: Normalized electroluminescence spectra from a DCM2 doped OLED shown in (a). The five curves are at five different current levels, each an order of magnitude higher than the previous. At the lowest current density (0.13mA/cm2) the device is nearly monochromatic, emitting only from DCM2 sites. As the current is increased, a larger fraction of the emission is from the Alq_3 sites. Inset is a plot of emission fraction versus current density for Alq_3 and DCM2 EL.

5.2 Time resolved photoluminescence

Photoluminescence studies are useful to investigate the role that excitons play within our devices. Because excitation by light is essentially injecting singlet excitons into the structure, such experiments are limited in the information they can provide regarding conduction processes. Time resolved photoluminescence measurements allow

us to study not only static exciton locations, but also exciton migration within a thin film structure. A typical measurement set-up is shown in Figure 5-5. 400 nm laser pulses (10 fs pulse width, 10 MHz repetition rate) were obtained from a frequency doubled output of a Ti-sapphire laser (Spectra Physics Tsunami) and directed towards a sample as an excitation source. Luminescence then was collected by focusing the output to a Streak Camera, allowing simultaneous collection of the time and wavelength resolved spectra (such as shown in Figure 5-5, bottom right). All measurements were performed at room temperature and under inert atmosphere to avoid photo-bleaching of thin films.

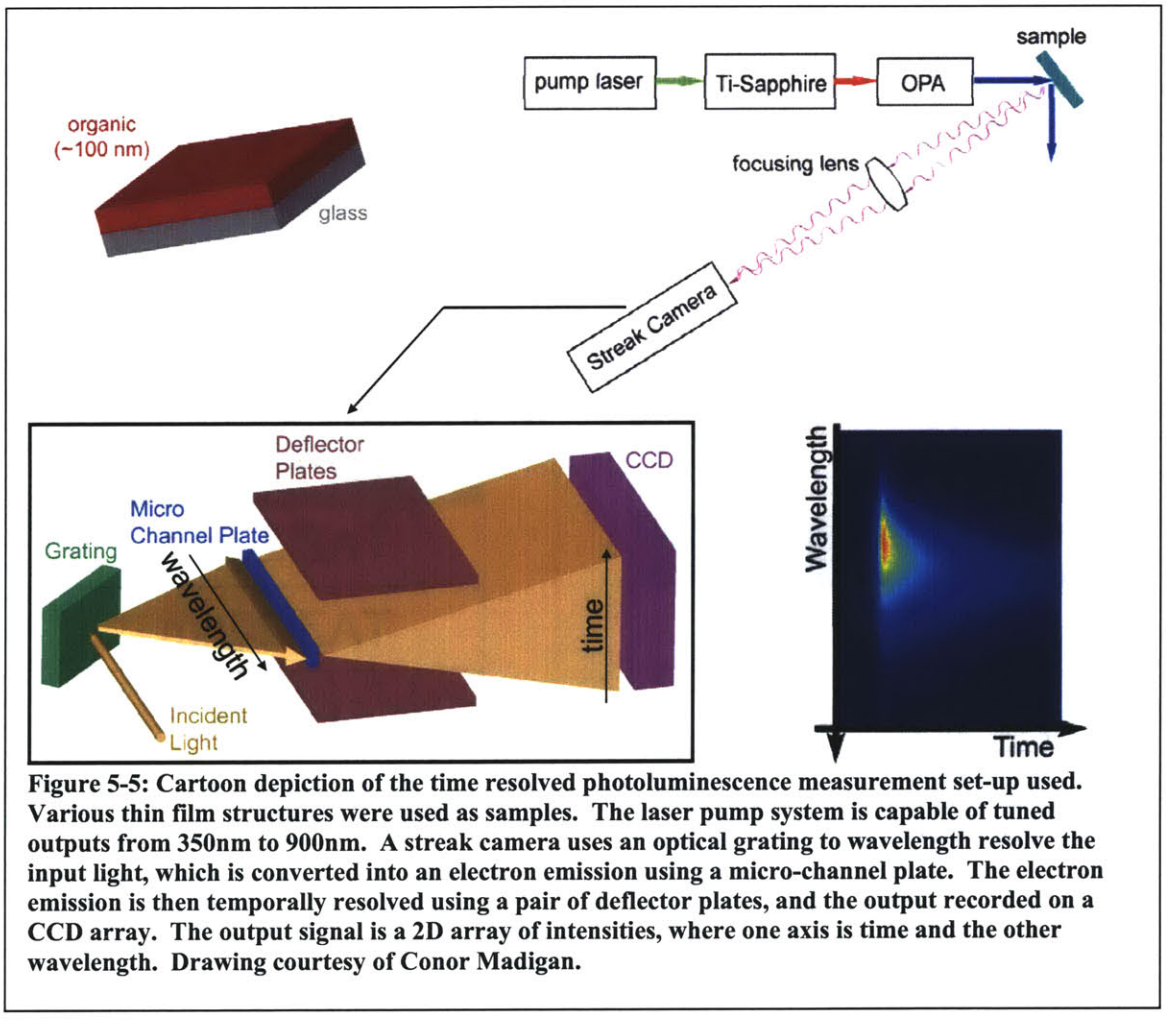

Figure 5-5: Cartoon depiction of the time resolved photoluminescence measurement set-up used. Various thin film structures were used as samples. The laser pump system is capable of tuned outputs from 350nm to 900nm. A streak camera uses an optical grating to wavelength resolve the input light, which is converted into an electron emission using a micro-channel plate. The electron emission is then temporally resolved using a pair of deflector plates, and the output recorded on a CCD array. The output signal is a 2D array of intensities, where one axis is time and the other wavelength. Drawing courtesy of Conor Madigan.

To investigate exciton migration processes in organic/QD hybrid thin film structures, we fabricated two sets of films using the micro-contact printing method discussed above. In the first set of films (Figure 5-6 (a, b)), an identical series of layers are grown on a glass substrate, with the only variable being the location of the layers. In the case of Figure 5-6 (a) the QD monolayer is separated from the $Ir(ppy)_3$ doped donor layer by a 20nm spacer of the wide band-gap organic molecule TAZ, while in Figure 5-6 (b) the QD acceptor layer is grown directly after the donor layer. The organic phosphorescent donor dopant $Ir(ppy)_3$ was chosen for it's well documented properties (triplet energy level 2.4 eV, triplet lifetime $0.8\pm0.1\mu s$)[121, 122], and it's suitability for energy transfer to red QD samples. The long triplet lifetime makes resolution of its PL decay easy to resolve from that of a typical CdSe QD, with a characteristic PL decay of less than $0.1\mu s$.

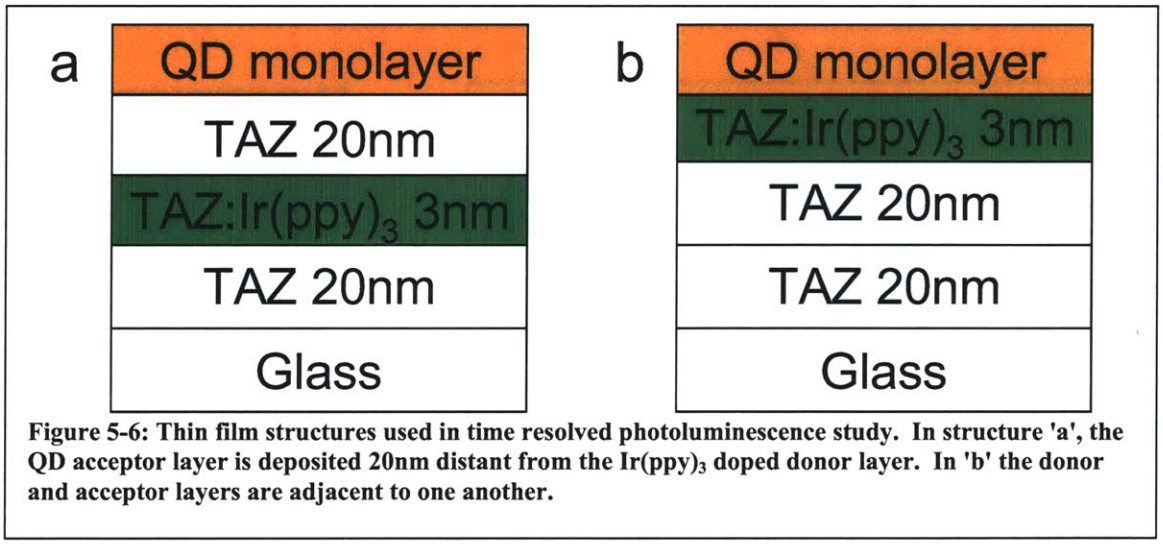

Figure 5-6: Thin film structures used in time resolved photoluminescence study. In structure 'a', the QD acceptor layer is deposited 20nm distant from the $Ir(ppy)_3$ doped donor layer. In 'b' the donor and acceptor layers are adjacent to one another.

When either sample of Figure 5-6 is excited with a pulse of 400nm excitation light, light is absorbed by both the QDs and the $Ir(ppy)_3$ (negligible light is absorbed by

the glass and TAZ). The collected data for Figure 5-6(a) is shown in Figure 5-7. In Figure 5-7 (a), the raw data is shown, with blue corresponding to a low number of counts on the streak camera, and redder colors corresponding to higher camera response. The vertical axis resolves the wavelength of the collected light, while the horizontal axis displays the timing of the light output. Figure 5-7 (a) shows the intense and long $Ir(ppy)_3$ response at 550nm, as well as a less intense and shorter lived QD response, centered at 610nm. Figure 5-7(b) sums the raw data along the time axis to show the static PL output of the sample, which is dominated by green $Ir(ppy)_3$ emission. This data shows clearly that the total light output of the $Ir(ppy)_3$ far exceeds that of the QDs when the two layers are uncoupled.

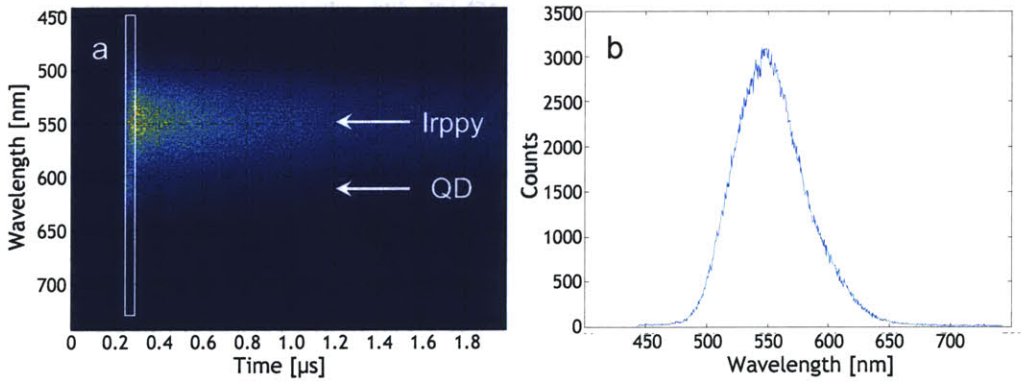

Figure 5-7: Time resolved photoluminescence data from the sample shown in Figure 5-6 (a). (a) shows the raw data as collected by the streak camera, resolved in both time and wavelength, and (b) shows the same data summed over all time, showing what the static PL spectra would look like.

However, much information is lost from this data if we only observe it over the 2μs window shown in Figure 5-7. Zooming in on the 20ns window highlighted by the white box in Figure 5-7(a), we can more clearly resolve the temporal response of the laser excited QD layer. Figure 5-8(a, b) are similar to Figure 5-7(a, b), but shown over the first

20ns window after the laser pulse excites the sample. Over this finer slice in time, the $Ir(ppy)_3$ emission is still visible, but the QD emission can be seen more clearly allowing us to see the PL decay function of the QDs when separated from the $Ir(ppy)_3$ layer by 20nm of TAZ spacer layer.

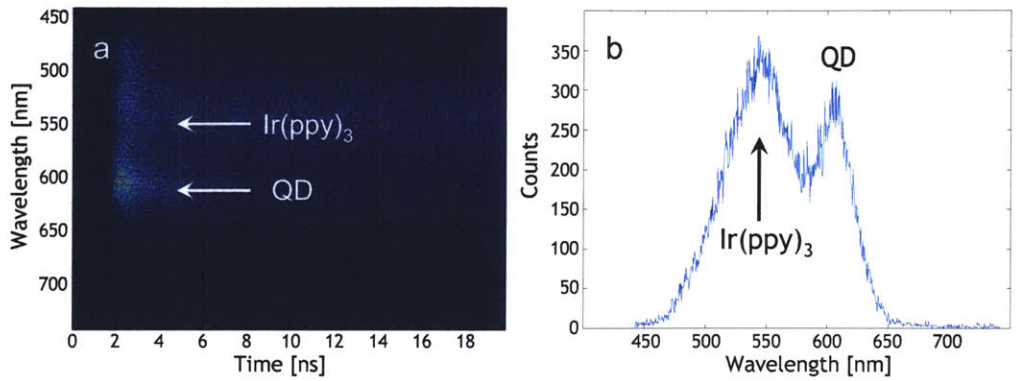

Figure 5-8: Time resolved photoluminescence data from the sample shown in Figure 5-6 (a), over the time window shown as a white box in Figure 5-7(a). As in Figure 5-7, (a) shows the raw data as collected by the streak camera, resolved in both time (over the 20ns window) and wavelength, and (b) shows the same data summed over the time window, showing the contribution of the QDs to the emission spectrum.

Next we perform the same analysis on the sample shown in Figure 5-6(b). Again we focus on a 20ns window so as to resolve the QD decay (Figure 5-9(a)). This sample's response is significantly different than that of Figure 5-6(a), with almost no perceptible emission at the wavelengths characteristic of $Ir(ppy)_3$ (500-600nm) despite the fact that the only variable in the experiment was layer location. Observation by eye confirms that the emission from this sample is intense red light, as opposed to the intense green emission seen for sample Figure 5-6(a). The summation over time if Figure 5-9 (a) gives the spectrum of Figure 5-9 (b), which not surprisingly shows a nearly monochrome spectrum of red QD emission. We assume that the $Ir(ppy)_3$ absorption is not dependent on its proximity to the QD layer (identical quantity of material deposited on the same deposition run), and hence the number of initially created $Ir(ppy)_3$ excitons is not altered

in this experiment. The nearly 100% quenching of $Ir(ppy)_3$ emission then implies that the excitons were quenched by the presence of the QD monolayer, and that this quenching process is strongly distance dependent since the other sample (Figure 5-6(a)) did not show this degree of quenching.

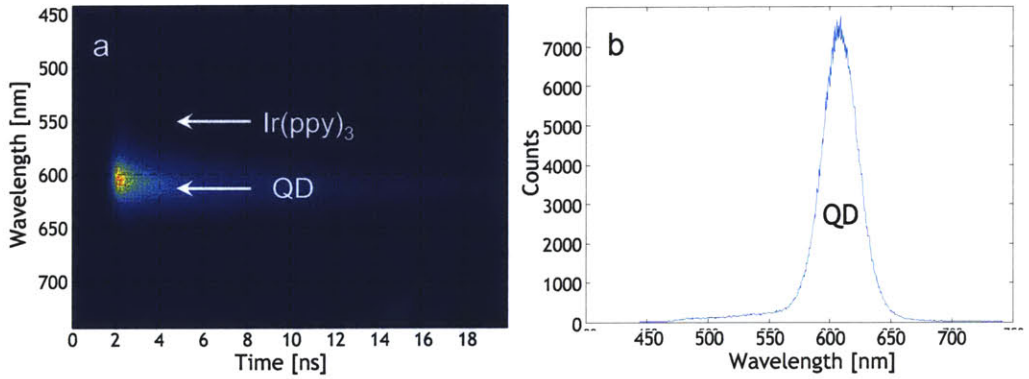

Figure 5-9: Time resolved photoluminescence data from the sample shown in Figure 5-6 (b), over a 20ns time window. As in Figure 5-7, (a) shows the raw data as collected by the streak camera, resolved in both time and wavelength, and (b) shows the same data summed over the time window, showing the dominant contribution of the QDs to the emission spectrum. This is in contrast to Figure 5-8, which shows similar contributions of both the $Ir(ppy)_3$ and the QDs, despite having identical quantities of each material in the thin film stack.

Using the same data sets (Figure 5-8(a) and Figure 5-9(a)) we can also analyze the QD PL decay versus time by summing vertically the region of QD PL over a window from 590nm to 640nm. Renormalizing the data, and fitting bi-exponential curves to each decay, we end up with the curves shown in Figure 5-10. Here, 'adjacent' and 'separate' refer to the structures of Figure 5-6 (b) and (a) respectively. The experimentally significant change in the PL decay curves corresponds to the new relaxation pathway that has been activated in the 'adjacent' sample. Here, not only have the $Ir(ppy)_3$ excitons been quenched by the presence of the nearby QD layer, but the lifetime of QD excitons in

the sample has been prolonged. This is due to the laser excited $Ir(ppy)_3$ excitons energy transferring with some non-instantaneous time constant to the QDs.

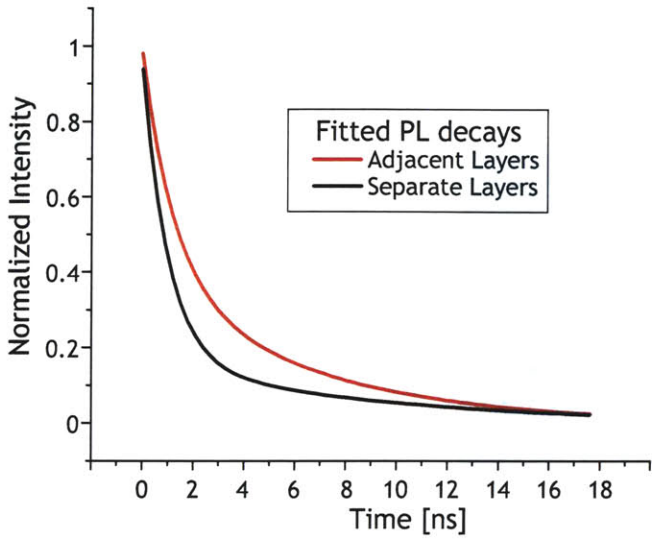

Figure 5-10: Photoluminescence decays of the QD layers for the two sample of Figure 5-6. Adjacent refers to Figure 5-6(b), and separate refers to Figure 5-6(a). The slower response of the adjacent sample is due to the delayed exciton pumping by energy transfer from the excited $Ir(ppy)_3$ molecules. This shows that $Ir(ppy)_3$ excitons are not only quenched by the QDs, but can also excite QDs to emit radiatively.

This observation of anomalously fast Förster energy transfer rate inspired further investigation of phosphor/QD hybrid thin film structures. In a follow-on study, three structures were fabricated as shown inset in Figure 5-11: sample I is a thermal evaporated 40 nm film of 10% $Ir(ppy)_3$ doped into CBP, sample II is a monolayer of CdSe quantum dots (7 nm diameter) micro-contact printed directly onto a glass substrate and sample III is a monolayer of the same sample of CdSe QDs printed onto an identical film of 10% $Ir(ppy)_3$:CBP. These three structures are then excited using a constant power excitation, without altering the collection geometry, allowing a quantitative comparison of light

output intensity. Figure 5-11 shows the total PL light collected for each of the three samples.

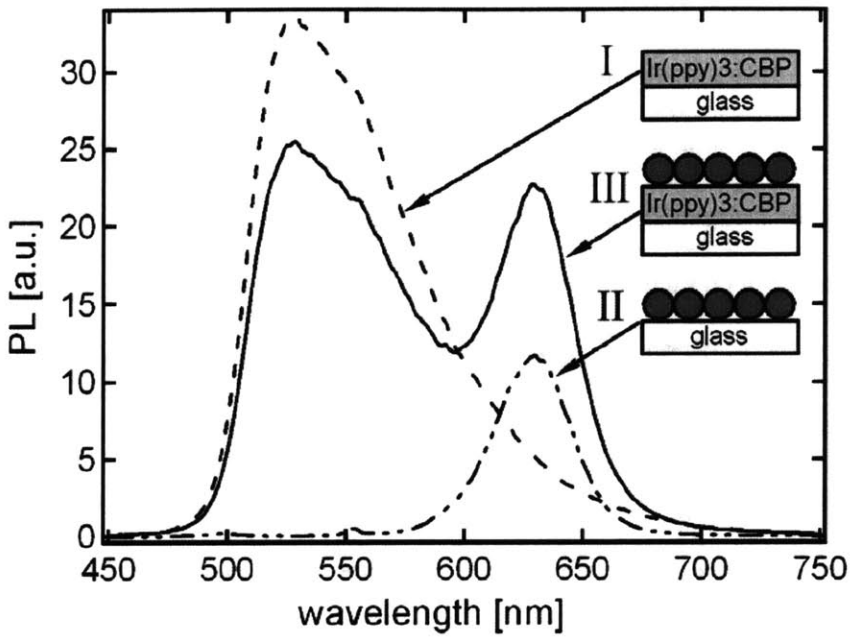

Figure 5-11: Integrated PL spectra of samples I, II, III. All measurements were obtained at the same excitation source power. The PL of sample III can be constructed from the linear superposition of samples I and II.

In Figure 5-11 we observe a decrease of $Ir(ppy)_3$ PL intensity in sample III compared to that of sample I. The CdSe QD PL is enhanced in sample III relative to sample II. This again indicates energy transfer from $Ir(ppy)_3$ to QDs, as expected from the first set of experiments above. We can once again rule out QD reabsorption of emitted green light due to the low absorption cross-section of the monolayer of QDs used. To quantify the extent of energy transfer, we can decompose the sample III spectrum into a linear sum of the two spectra of samples I and II. This tells us there is 62 % increase in intensity of QD emission while the $Ir(ppy)_3$ luminescence is quenched by 21 %.

Figure 5-12 shows the time resolved data from all three samples. The PL decays of samples I and II are simple to analyze, and clearly show the difference in decay times between the QDs and the $Ir(ppy)_3$. The PL decay of sample III is partitioned by wavelength, and plotted as two separate lines in Figure 5-12. The $Ir(ppy)_3$ peak partition is taken as 510 – 560nm, and the QD window is defined as 600 – 650 nm. The initially rapid drop-off of emission intensity within the QD window is the fast decay of the QDs which are directly pumped by the excitation source. The $Ir(ppy)_3$ emission tail is clearly overlapping with the QD window, but this is taken into account in the dotted line decay of Figure 5-12, where for 20 points the $Ir(ppy)_3$ contribution to the emission spectrum is subtracted from the total QD window. Even after this subtraction, it is clear that the QD PL decay in sample III has been lengthened significantly. Additionally, the $Ir(ppy)_3$ decay has been shortened in sample III by the presence of the QD monolayer, consistent with the $Ir(ppy)_3$ acting as a donor for exciton energy transfer.

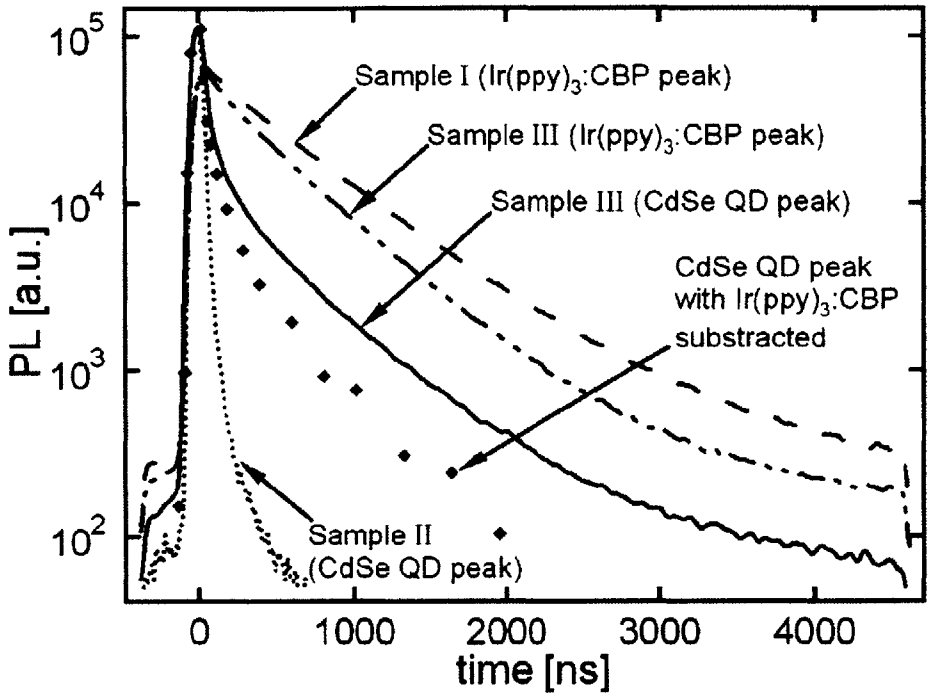

Figure 5-12: PL decay of all three samples described in Figure 5-11. Two distinct wavelength windows of sample III are separated, as well as the QD window decay with $Ir(ppy)_3$ emission subtracted. The QD temporal response matches that of $Ir(ppy)_3$ after the initial fast decay of the directly excited QDs (first hundred nanoseconds after excitation pulse). This is direct evidence that the QDs are emitting light via energy transfer from the $Ir(ppy)_3$ molecules, as QD emission would not otherwise continue over the time scale of microseconds.

Figure 5-13(A) shows the instantaneous spectra of sample III at three points in time, demonstrating the presence of QD emission even 1500 ns after the excitation pulse. This can be compared to the sample I spectrum at identical time, showing the clear lack of a peak at 630nm. This is further emphasized in Figure 5-13(B), where the $Ir(ppy)_3$ emission for each time is subtracted from the sample III spectrum, yielding spectra that correspond to the QD emission precisely. Since this QD emission is simply not present so long after the excitation pulse in sample II, we conclude that this emission is due to the

exciton energy transfer from $Ir(ppy)_3$ molecules, proving the possibility of energy transfer in phosphor/QD systems.

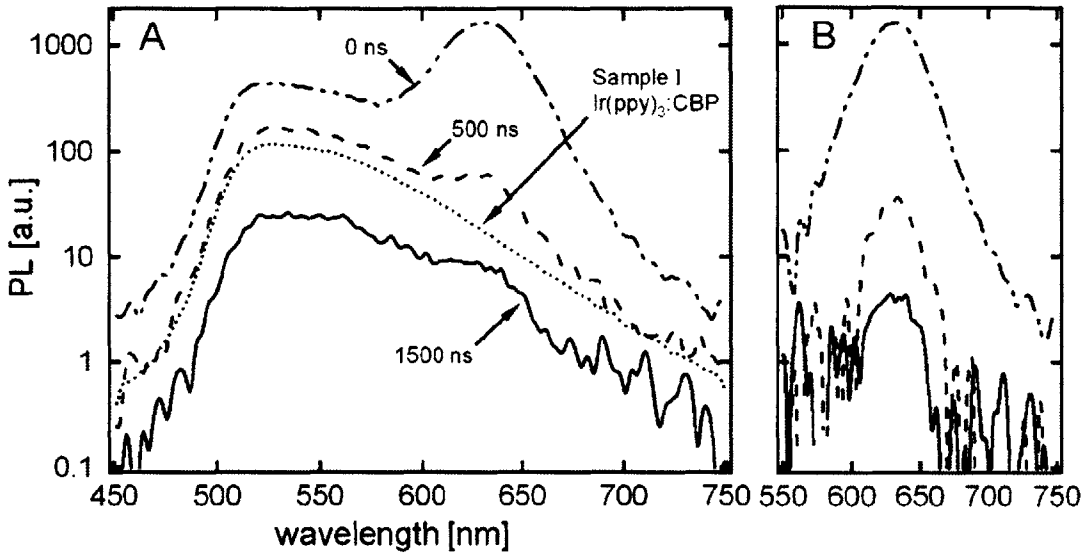

Figure 5-13: PL spectra of sample III taken at 0 ns (referenced to the excitation pulse arrival), 500 ns and 1500 ns, as well as the 500ns spectra of sample I for comparison. While the relative intensity of the QD peak to the $Ir(ppy)_3$ peak is decreasing with time, there is a signature of QD emission even 1500 ns after the excitation pulse arrival, a clear indicator of delayed excitation of the QDs by long lived excitons on $Ir(ppy)_3$ molecules. (B) shows the same three spectra, with the sample I emission subtracted out to show only the QD contribution. The resulting spectra correspond to the QD spectra of sample II.

Using this data, we may calculate an upper limit to the Förster energy transfer radius of this system. The calculation will yield an upper limit only, since the energy transfer of this experiment is exciton diffusion limited, and is thus a sum of the Förster radius as well as a contribution due to exciton diffusion on $Ir(ppy)_3$ molecules within the 40nm film. The rate of energy transfer between a donor molecule and a thin layer of acceptors is described by[123]:

$$K_{D-AL} = \left(\frac{1}{\tau}\right)\left(\frac{R_F}{R}\right)^4 \qquad \textbf{Equation 5-1}$$

Where τ is a donor relaxation time, R is a distance from a single donor to the acceptor layer, R_F is the Förster energy transfer radius, and $K_{D\text{-}AL}$ is the rate of energy transfer from donor molecule to acceptor layer. Relaxation rate of the donor in the absence of acceptors is $K_D = 1/\tau$. In our case we are dealing with a film of donors transferring energy to a monolayer of acceptors. Total transfer in this case can be obtained by integrating over the donor film thickness (which can be assumed infinite in this case)[124].

$$K_{D-AL}^{TOT} = \frac{R_F^4}{\tau}\int_{R=(b+a)/2}^{R=\infty}\frac{Q\rho dR}{R^4} = \left(\frac{1}{\tau}\right)\frac{QR_F^4}{32b(b+a)^3} \qquad \textbf{Equation 5-2}$$

Where ρ is a linear donor molecular density, Q is a percentage of donor molecules doped into the host material, a is the QD radius, and b is the $Ir(ppy)_3$ molecular radius. Efficiency of exciton transfer from donor to acceptor is:

$$\eta_{ET} = \frac{K_{D-AL}^{TOT}}{K_{D-AL}^{TOT} + K_D} \qquad \textbf{Equation 5-3}$$

Knowing η_{ET} which is equal to the percentage of $Ir(ppy)_3$ PL quenched by presence of QDs, we can use Equations 5-2 and 5-3 to calculate R_F. Earlier in this section η_{ET} was found to be 0.21 (Figure 5-11). In our experiment amount of doping Q of $Ir(ppy)_3$ into CBP was 0.1. Taking all these parameters into account we calculate R_F to be at most 13nm for this system. This number is consistent with Förster energy transfer radius calculation performed both for molecule-molecule systems[124], as well as QD-molecular systems[125].

In conclusion, enhanced PL of CdSe QDs can be achieved via Förster energy transfer from a phosphorescent sensitizer, extending the PL relaxation time of CdSe QDs to 1500 ns.

5.3 QD charging study

The previous two sections give us information on the location and dynamics of excitons within QD-LEDs and QD/organic heterostructures, but tell us little about the role a QD monolayer plays in conduction within our archetype QD-LED structure. However, the recent advance of QD micro-contact printing allows us to fabricate a series of devices that probe this effect. Figure 5-14 shows a series of LEDs fabricated using identical growth conditions; all organic films were grown simultaneously on each substrate, and the QD layers were applied using the same QD solution spun within a ten minute period of each other, and micro-contact printed subsequently. We label the devices Device A – where the QD monolayer has been applied within the Alq_3 layer, Device B – where the QD layer is located at the organic heterojunction (our archetype QD-LED), Device C – QDs embedded within the TPD layer, and Device D – control device without any QD layer (our archetype OLED).

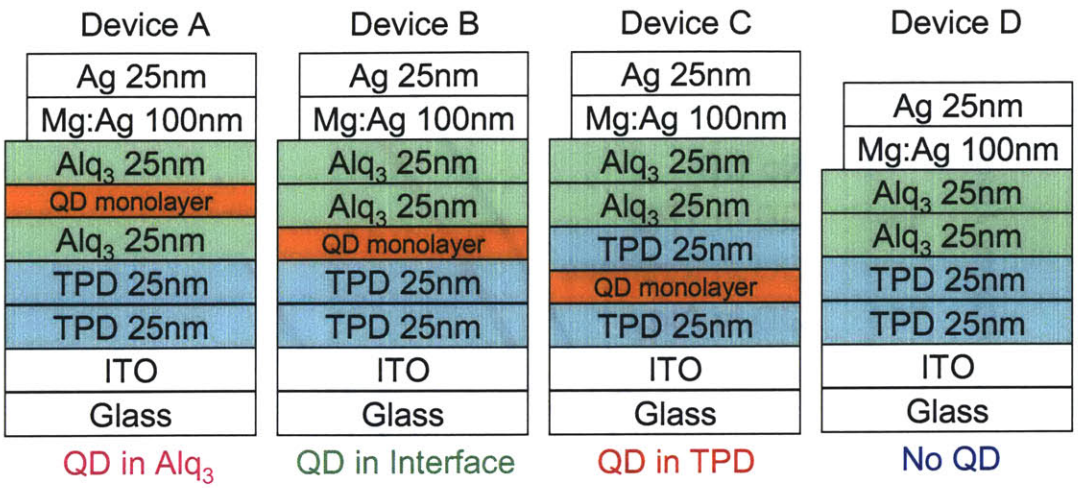

Figure 5-14: Series of device structures fabricated to isolate the role of QD monolayers in conduction processes within QD-LEDs. All devices are fabricated under the same conditions, with the organic layers deposited simultaneously. Devices A, B, and C incorporate a micro-contact printed monolayer of QDs within different regions of the device, while Device D is a control device without a QD monolayer.

Figure 5-15 summarizes the current-voltage response of this series of devices. All devices have low leakage current density at low bias voltage (< 3V), and hence all of the traces start out at the lower limit of current detection of the ammeter (< 1 nA/cm^2). The first device to turn on is the control device, Device D. At 3V, this LED begins to pass current which follows the typical OLED dependence of $J \propto V^{m+1}$ where for this device $m \approx 7$, indicative of trapped-charge limited space-charge conduction. This trace is stable over several scans, as are all the traces shown in Figure 5-15, as indicated by the multiple lines presented for each device.

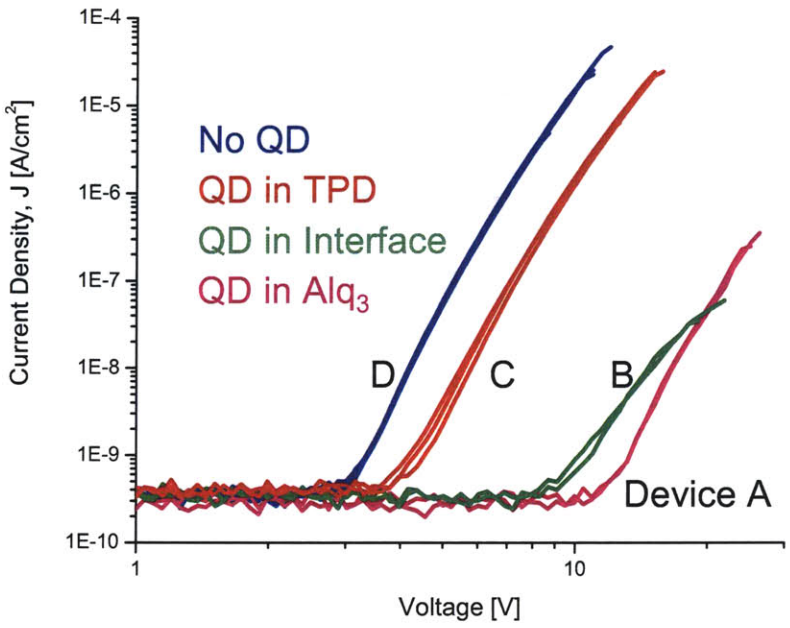

Figure 5-15: Current density versus bias voltage plots for the series of device structures depicted in Figure 5-14. The flat line portion of the plots does not indicate a constant relationship between current and voltage, but rather is the lower detection limit of the ammeter used in the measurement. All devices show a $J \propto V^{m+1}$ dependence with m between 5 and 7, indicative of trapped-charge limited space-charge conduction. The difference in operating voltages allows us to infer the different role that the QD monolayer plays in conduction within each device.

Device C begins to pass a detectable level of current at ~4V, and with increasing bias shows almost parallel performance to Device D. From this, we can conclude that the operating mechanism and conduction pathways of the device are almost completely unaltered. The slight increase in operating voltage can be completely accounted for by the increase in total device thickness that arises due to the inclusion of the QD monolayer. The effective thickness of this layer is ~10nm, which is a 10% increase in device thickness. The effect of device thickness on operating voltage has been studied in detail[126] for OLEDs, giving rise to a rule of thumb that for a given current, $V \propto t^2$, where V is the bias voltage needed to yield the given current, and t is the total device thickness.

This rule of thumb is in good agreement with the increase in voltage observed between Devices C and D. From this we can conclude that the QDs do not play an active role in hole conduction when embedded within a HTL layer of an OLED.

Figure 5-16 further validates this conclusion, showing the normalized, spectrally resolved light output of the devices shown Figure 5-14, and measured in Figure 5-15. In these devices, the electroluminescence (EL) peak at 610nm corresponds to the QD sample emission, and the peak centered at 525nm corresponds to Alq_3 EL. The control Devices D allows us to compare the exact shape of the Alq_3 emission profile with the emission profile of Device C, which is perfectly overlapping. Thus there is negligible QD emission from Device C and we may conclude that the QDs play no active role in conduction in this device, since this would correspond to some signature of QDs in EL emission.

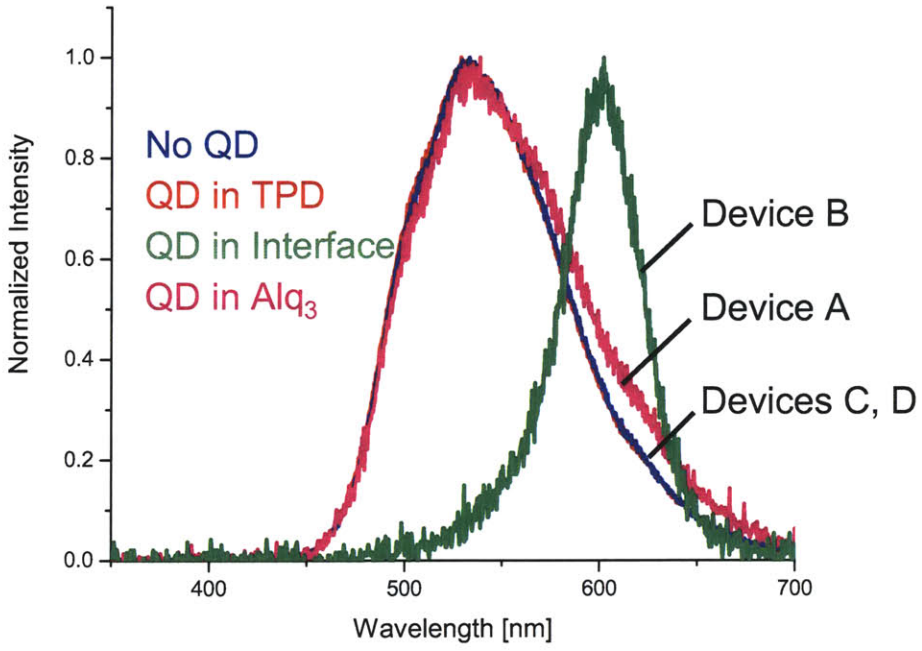

Figure 5-16: Normalized electroluminescence (EL) spectra for the series of device structures depicted in Figure 5-14. The peak at 610nm corresponds to the emission wavelength of the QD sample used in this series of experiments, while the peak at 525nm corresponds to the EL spectrum of Alq_3 which was used as the electron transport layer in this device series. Device B shows dominant QD emission, and Device A shows some small percentage QD emission, while Devices C and D show EL spectra that are entirely due to the emission of Alq_3.

Returning to the current-voltage characteristic of Device A (Figure 5-15), we again see the same basic plot, but this time at a greatly increased operating voltage as compared to Devices C and D. Possible explanations of this increase are thickness, as above, or inclusion of a deep trap layer within the device. If we try to correlate this to a thickness increase, we calculate that the QD layer thickness is ~70nm, well in excess of the experimental variation observed for both spin-casting and micro-contact printing of QD monolayers. This leaves us with the conclusion that the QD monolayer in Device A is acting as a deep trap to electrons in their conduction through the ETL. Further

evidence of this is found in Figure 5-16, where the EL spectrum of Device A reveals a minor component that is due to QD emission. This is to be expected if the QD monolayer is populated with electrons, since the statistically small number of holes that are present in the Alq_3 layer may now form excitons on the QDs, giving rise to QD EL. That QDs act as deep traps to electrons when placed adjacent to an ETL within OLEDs is not surprising given our proposed band diagram (see Figure 5-1).

Device B is our archetype QD-LED, and the spectrum shown in Figure 5-16 is similar to those found in Figure 3-8 and Figure 4-3. The current-voltage characteristic of this device is most similar to that of Device A, which is the expected result since they both contain QD monolayers adjacent to an ETL. The slightly lower turn-on voltage of Device B relative to Device A can be explained in terms of the greater availability of holes to neutralize the charged QDs in Device B, where the HTL is adjacent to the QD monolayer. The difference in slope of this device is not well understood, but could be associated with the increase in trap depth the QD electrons experience relative to the LUMO level of TPD rather than Alq_3 (see band diagram in Figure 5-1).

5.4 Conclusions

Taken individually, these three experiments each give us clues as to the operating mechanism of QD-LEDs. Analysis of the EL spectral dependency on current density in QD-LEDs containing sub-monolayers of QDs informs us of the source of non-QD EL in our devices. Time resolved PL of QD monolayers adjacent to phosphorescent organic molecules proves that efficient Förster energy transfer is indeed possible from excited molecules to QDs. Study of the current-voltage and spectral characteristics of QD-LEDs with QD monolayers placed in different locations of the device structure allows us to

further understand the role of QD monolayers in charge conduction. Taken collectively, we can make even stronger statements about device operation.

In our best devices (see for example Figure 3-8) the extremely monochromatic spectrum implies very high surface coverage of QDs in the monolayer. This effectively eliminates the effects of Chapter 5.1 from contributing to the device operation. Chapter 5.3 tells us that we can then assume that at most current densities, the complete QD monolayer is significantly charged with electrons. However, we also know from Chapter 5.2 that any excitons on neighboring organic molecules will energy transfer onto the QD. If this energy transfer was indeed the mechanism for efficient EL in our devices, than changing these neighboring molecules from fluorescent to phosphorescent species is expected to quadruple the observes EL external quantum efficiency. Repeated attempts at this experiment (in various device structures) have failed to demonstrate an efficiency increase – in fact it is usually coupled to an efficiency decrease despite the far greater η_{EL} that is achieved in these phosphorescent OLEDs which do not include a QD monolayer. However, it is now possible to understand this failure in light of Chapter 5.3. In spite of the increased number of excitons which Förster energy transfer to the QDs, the Auger recombination process effectively quenches all such excited QDs, since they are also statistically likely to contain an electron. This allows us to conclude that the efficient emission process in our QD-LEDs is actually direct injection of charge (both holes and electrons) into the QD to create neutral excitons which can then recombine radiatively before an additional electron is injected. Creation of more efficient devices operating by this mechanism requires a finely balanced injection of electrons and holes into the QDs, something which the device band diagram (Figure 5-1) suggests will be challenging. The

QDs are acting as deep traps to electrons, due to the much higher electron affinity of QDs relative to Alq_3. However, the ionization energy of the QDs is much higher than that of any known organic hole transport material, and thus there is actually a high (> 1 eV) energy barrier to injection of holes into the QD. This barrier is lowered when a QD is charged with an electron, due to the Coulombic attraction, but most estimates of this Coulomb effect suggest that the barrier lowering is only 0.1- 0.3 eV. Use of high work function hole transporting materials in place of organics is one area where future work is likely to focus.

6 Conclusions

Incorporation of nanoscale active elements into OLEDs enables the creation of a new set of devices, the properties of which can be tailored at the quantum mechanical level. However, attaining such levels of control necessitates a separation of the creation of the nanoscale elements (*i.e.* QDs, J-aggregates) and the macro-device fabrication. In the case of QDs, it is the colloidal chemical growth process that enables the nanometer scale control over the material properties. The phase separation or micro-contact printing process then controls the precise positioning of these nano-elements within a large area device. It is the combination of these two distinct nano-fabrication steps that enable creation and control of QD-LED properties. Importantly, once we learn to manipulate these two material sets to make hybrid structures, other possible applications open up as well. Use of the nanometer period pattern that results from phase separation as a patterning template is a foreseeable application that is now on the horizon.

In addition, the properties of known devices are improved through the use of this nanotechnology. The color gamut that is accessible to QD-LEDs far exceeds that of conventional OLEDs (as shown in Figure 6-1), due to the narrow FWHM of emission of the QDs themselves. In addition, power savings are also likely due to the narrow QD emission profile. If one assumes that device operating voltages and external quantum efficiencies will converge for the two technology platforms, a QD-LED device has the potential to be 50% more power efficient than the equivalent phosphorescent OLED, based upon the spectral purity of the QD emission profile. QD-LEDs can be continuously tuned in nanometer increments from the visible to the near infrared, as

shown in Figure 6-2, as opposed to OLEDs, for which color tunability requires major changes to complex molecular syntheses.

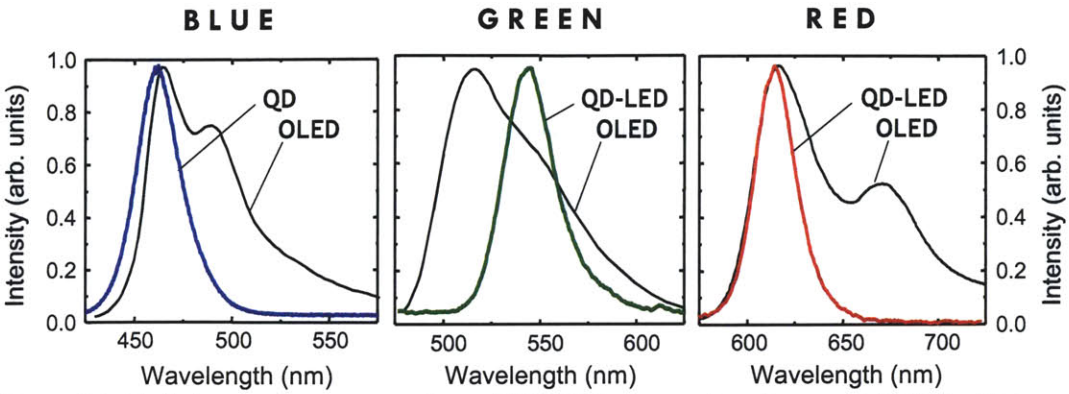

Figure 6-1: Emission spectrum comparison of QD-LEDs versus phosphorescent OLEDs. The lumophores used are FIrpic, $ppy_2Ir(acac)$, $btp_2Ir(acac)$ for the blue, green and red OLEDs respectively, and (CdS)ZnS, (CdSe)ZnS, and (CdSe)ZnS for the blue, green, and red QD-LEDs respectively.

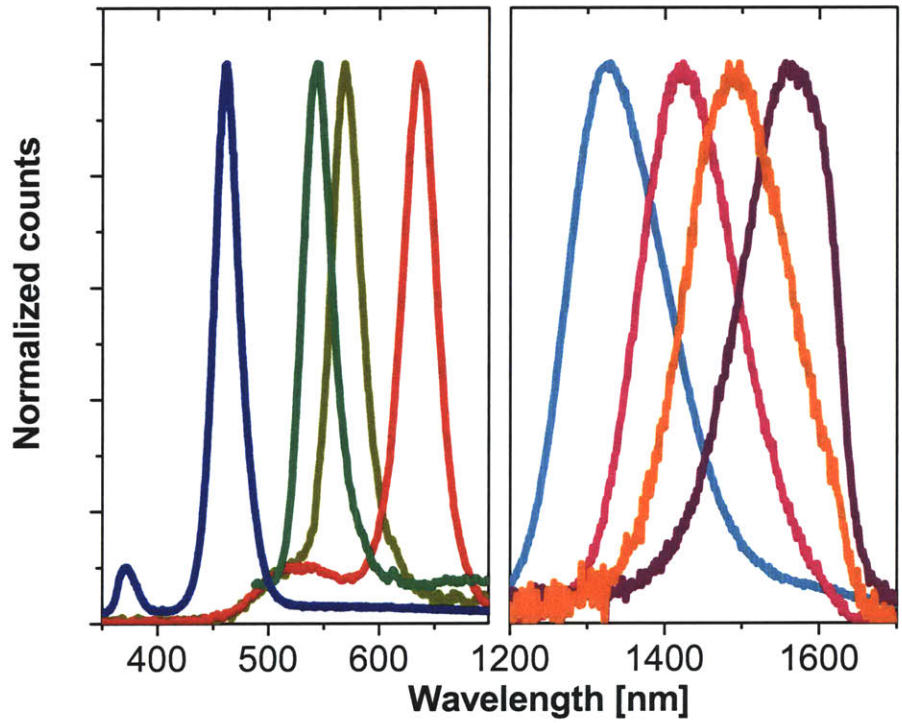

Figure 6-2: Electroluminescence spectra of eight different QD-LEDs, demonstrating both their range and continuous tunability. The visible LEDs incorporate CdS, ZnSe or CdSe core QDs, while the infrared LEDs incorporate PbSe core QDs.

QD-LEDs are a versatile test-bed for studying the electrical and optical behavior of QDs in the solid state. Active devices allow us to probe the electrical properties of single monolayers of QD solids. Furthermore, there is evidence that such devices could satisfy the technological requirements of flat panel displays and imaging applications which require the narrowband emission characteristic of QDs, as well as the efficient creation of visible light in the blue and red regions of the spectrum. In a span of eight years QD-LED efficiency has improved over two orders of magnitude reaching the luminous and quantum efficiencies of fluorescent OLEDs. This rapid advance was facilitated by the expanding knowledge of the OLED community whose developments are largely applicable to the QD-LED structures. Indeed, we identify QD-LEDs as a kin technology to OLEDs, potentially complementing their performance when highly saturated color emission is desirable. It is conceivable that with further development, QD-LEDs could reach the efficiencies of phosphorescent OLEDs since all of the electrically generated excitons within a QD are allowed to relax radiatively. The combination of inorganic luminescent properties with the advantages of organic processing techniques suggests the possibility of creating robust, large area emitters with physical properties that are tailored on the nanoscale. The present pursuit of QD-LEDs has the potential for near term scientific and technological impact, as the fabrication and synthetic processes are perfected.

7 Future Work

This work has to date yielded QD-LEDs from blue to the near infrared, two general deposition methods for making large area assemblies of a single sample of QDs, and an understanding of the operating principles behind QD-LEDs. We can now apply what we have learned about QD-LED device structures to create truly high efficiency QD-LEDs, approaching the theoretical limit of 100% internal quantum efficiency. It is our hope that QDs will be the clear choice amongst blue emitting materials, and will thus be a major focus of continuing OLED research. Finally, it should now be possible to create a white LED from a mixture of the three emitters used in the sub-pixel devices. Such as device could be of significance to the Next Generation Lighting Initiative and other programs funded by the government in an attempt to lower the power consumption of white indoor lighting, which currently consumes 25% of total power in the U.S. QD photodetectors, solar cells, and all inorganic QD-LEDs as well as voltage driven QD-LEDs are all on the horizon of QD devices incorporated into optoelectronic devices.

7.1 Mechanism of fabrication methods

The development of both phase separation and micro-contact printing processes for QD monolayer deposition has enabled the creation and study of QD-LEDs. However, our current understanding of how and why these processes operate effectively remains to be completed. Certainly first strides have been made in both of these areas. In fact, initial experiments on understanding the organic underlayer's role in phase separation led directly to the successful demonstration of the contact printing method. Additional experiments quantifying the surface energies of all the materials involved will be critical to furthering our understanding of this process, as will information on the effect of both

organic small molecules and QDs on the drying dynamics of the organic solvents used in phase separation (collected by thermal gravimetric analysis, mass spectrometry, etc.). Understanding how and when in the drying process the QDs arrange into two-dimensional sheets would also be beneficial in understanding the robustness of these techniques for conversion into manufacturable industrial processes.

7.2 Pump-probe EL-PL experiments

Understanding the excited state of the QD during normal device operation is of course critical in determining conclusively the mode of operation of the QD-LEDs discussed in this work. Fabricating our archetype devices and running them under normal bias conditions does not allow for analysis of this QD excited state. However, simultaneous PL experiments during normal EL operation could provide some important clues in this realm. If the QDs are predominantly charged under forward bias, their PL quantum yield should be measurably reduced due to Auger recombination. However, if the QDs are not charged, but rather only excited by relatively short-lived (10-30ns) excitons, the effect on QD PL quantum yield will be greatly reduced. By pulsing PL excitation , EL excitation, or both at different frequencies, much information could be obtained from an operating device *in situ*.

7.3 Lifetime testing

Research to date has focused on improving the manufacturability and quantum efficiency of QD-LEDs. To show their feasibility in commercial applications, however, it is critical to demonstrate lifetimes that compare well with the state-of-the-art OLED specifications. Currently, commercial OLEDs quote lifetimes of anywhere from 5,000 to 80,000 hours, though there is much discrepancy in the literature about both how to

measure and report device lifetime information. Regardless, it is critical to QD-LED commercial development to show that the nanocrystals do not negatively impact overall device lifetime, and that indeed the lifetime is increased due to the stable, inorganic nature of the QD crystals. At the time of this writing, work is underway to build a lifetime testing set-up, and so it is our hope to have this data very soon.

7.4 All inorganic QD-LEDs

The creation of QD-LEDs based upon all organic LEDs was a natural starting point for our research. OLED fabrication processes are in many respects compatible with QD materials. Replacement of the unstable organic lumophore of an OLED with an inorganic, and hence more stable, QD is one motivating factor in this substitution. Successful demonstration of this QD-organic-LED (QD-OLED) points out the desirable properties of inorganic materials in optoelectronic devices. Indeed, the remaining role of organic materials in this QD-OLED is charge transport, something with all semiconductors, not just organic semiconductors, are capable of providing. Inorganic semiconductors in fact have better band alignment with the hole and electron levels of the inorganic QDs which we use. It is the amorphous nature of the organic semiconductors which allows us to grow them inexpensively over large areas, on any substrate (non-epitaxially). However, amorphous inorganic semiconductors are also abundant, and can indeed be grown over very large areas in many high throughput manufacturing processes (such as the FPD industry). This leads us to the concept of a QD-inorganic-LED, or QD-ILED. Figure 7-1 summarizes the band gaps of some potential candidate materials for transport layers for the QD-ILED. Work is already underway to realize this QD-ILED in the lab. At the time of writing, saturated light emission has been measured from such a

device, although the external quantum efficiency is extremely low ($\eta_{EX} < 0.001\%$). This project has much promise, not only because of the higher stability QD-LED which will result, but also because this could represent the first step along the path of realizing electrically pumped QD lasers. Optically pumped QD lasers have already been demonstrated[127], but the lack of an effective charge delivery scheme has to date prevented this next step from being taken.

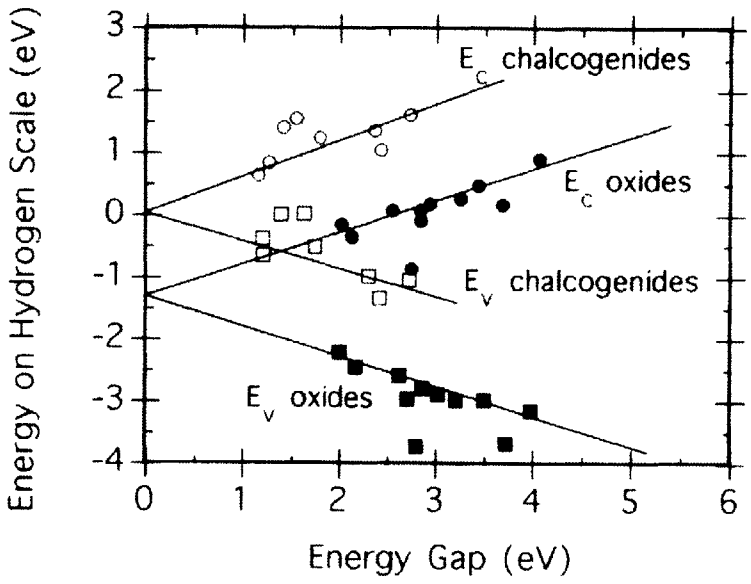

Figure 7-1: Energy band gaps of a selection of inorganic semiconductors. Both chalcogenides and oxides could be useful materials for inorganic transport layers in QD-ILED devices. Any material with a band gap greater than 2.7 eV that can be grown near to room temperature is a candidate for this application. (Source: Konenkamp, 2000[128])

7.5 Solid State Lighting (White) QD-LEDs

The majority of this work has focused on the narrow band light emission inherent to QD samples with narrow size distributions. The direct result of this is QD-LEDs with a correspondingly narrow EL spectrum and hence high color saturation, a desirable trait for display applications. However, the other prevalent light emission application, general

white lighting, can also benefit from this property. In order to create high quality white light efficiently, it is necessary to emit across the visible wavelengths such that emission spectrum closely matches that of a high temperature blackbody source. This is because our definition of high quality white is connected to the light produced by the sun, as measured by the quantities color temperature, and color rendering index (CRI). The former measures the blackbody temperature that most closely matches the produced spectrum, and the latter measured the ability of a human to view standard dyes under illumination by a light source on a scale of 0 to 100. An ideal general lighting source will allow a user to both choose the color temperature which is most appropriate for a given setting, and to achieve extremely high CRI at that color temperature.

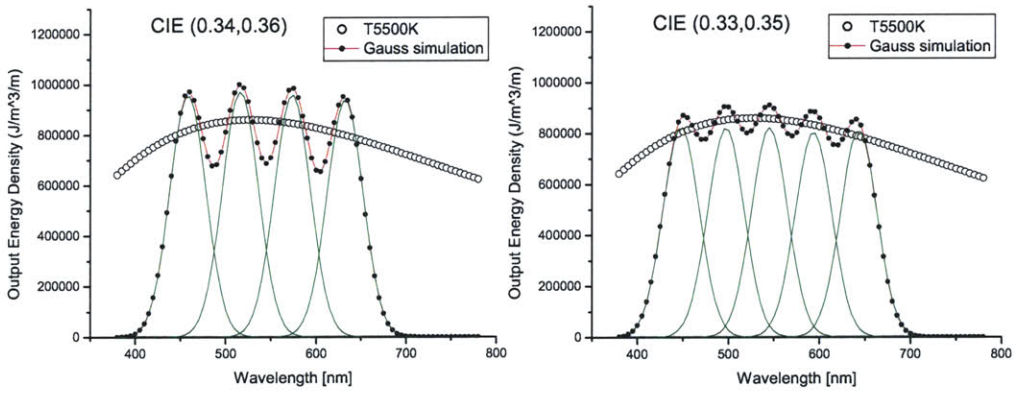

Figure 7-2: Numerical simulation of mixing QD-LED emission to make an ideal white light source for general illumination. Using four different QD samples (left) within one LED will generate white light as defined by the CIE color coordinate system. However, the relatively large deviation from the 5500K color temperature reference spectrum will lead to a color rendering index between 60 and 70. However, if we mix five different QD samples together (right) this deviation from the black body spectrum is greatly reduced, and the CRI approaches 90.

QDs offer the ability to achieve this goal, while emitting no extra photons at wavelengths that are useless to the observer. By utilizing a number of QD samples, synthesized to emit efficiently at different wavelengths, a perfect white emitter could be

achieved. Acceptable CRI can be achieved with as few as four or five different colors (see Figure 7-2). The ease of QD band gap tuning during growth will enable quick development of the appropriate set of samples. In addition, because large area lighting does not require lateral patterning of materials, our phase separation technique can be used as a single step fabrication method for both the HTL and the QD monolayer. This architecture is ideal for a QD-LED based, stable, efficient, low cost, tunable color temperature and high CRI solid state lighting solution.

7.6 QD Photodetectors

While the previous future directions focused on the process of light emission from QD based devices, the opposite process also has applications. Using the QDs as a light absorber and exciton generator, and then subsequently breaking up the exciton into charge resulting in current yields either a photodetector or a solar cell. QD photodetectors have the potential to be wavelength selective and to have very low dark current, due to their insulating nature. This is of particular importance in the infrared, where typical detectors are dominated by thermally generated charge carriers and must be cooled to low temperatures in order to have acceptable noise thresholds. In addition, the high absorption cross-section of a QD could allow for efficient light absorption in very thin layers, leading to either high speed detectors or high efficiency solar cells. Much study has already been completed in this area[129], yielding zero-bias internal quantum efficiencies of 1%. The device structure used to achieve this is shown in Figure 7-3.

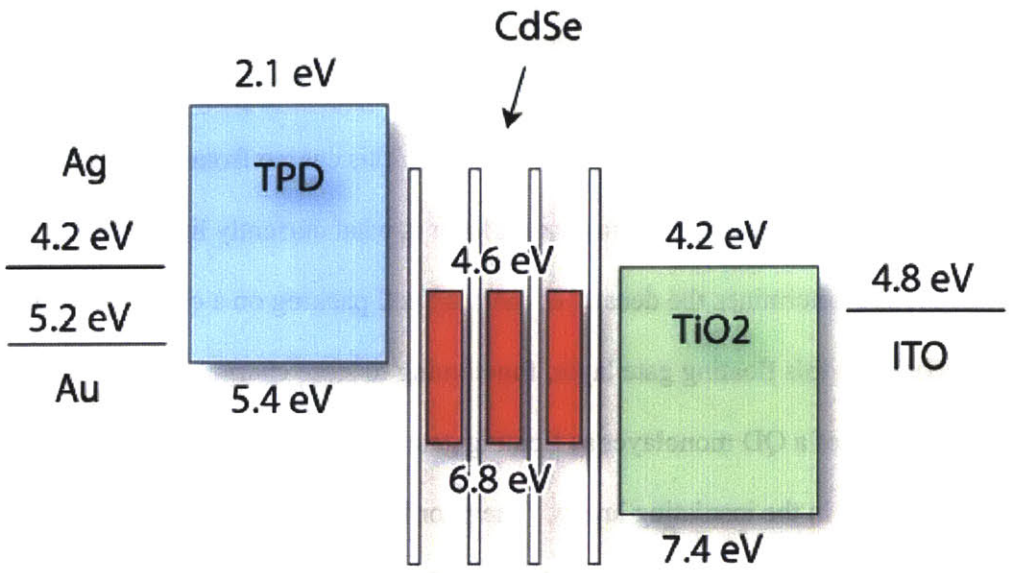

Figure 7-3: Energy level alignment in a three layer QD photodetector device. Photons are absorbed on the QD multilayer only, creating excitons. TPD is used to accept and transport holes to the Ag/Au cathode. Electrons are accepted by the intrinsic TiO_2 layer, and transported to the ITO anode. This device is almost a perfect replica of our QD-LEDs, with charge flowing in the opposite direction to produce electrical current from a light input.

Future work in this area could take advantage of the new fabrication techniques developed in this thesis, though they would likely need to be adapted for thicker film coatings. Additionally, any understanding of charge injection in QD-LEDs will have direct applicability to QD photodetectors in understanding the charge extraction process. Hence, though these two projects have often walked independent paths, it is clear that there is much possibility for cross-fertilization of ideas between them.

7.7 QD Memories

Solid state non-volatile memory devices (NVMs) have gained widespread commercial acceptance in recent years. They are used in applications where light weight, fast access times, and low total storage capacity are required, such as portable MP3

players and storage drives. The floating gate field effect transistor (FET) device is typically used, where charge is stored on a floating electrode buried between insulators. Charge may be written or erased from this floating gate via voltage spikes which tunnel electrons to or from the gate. However, the leakage of this charge from the floating gate to the transistor channel through the insulating layer is what currently limits storage performance, and determines the density of memory cell packing on a chip. QDs could have application to this floating gate layer, functioning to store charge within their cores. The added benefit of a QD monolayer as floating gate is that it can tolerate a high density of pin-hole defects in the insulating layers. The poor lateral conductivity of the QDs will allow each pin-hole defect to discharge only one QD within the floating gate, rather than the entire memory bit.

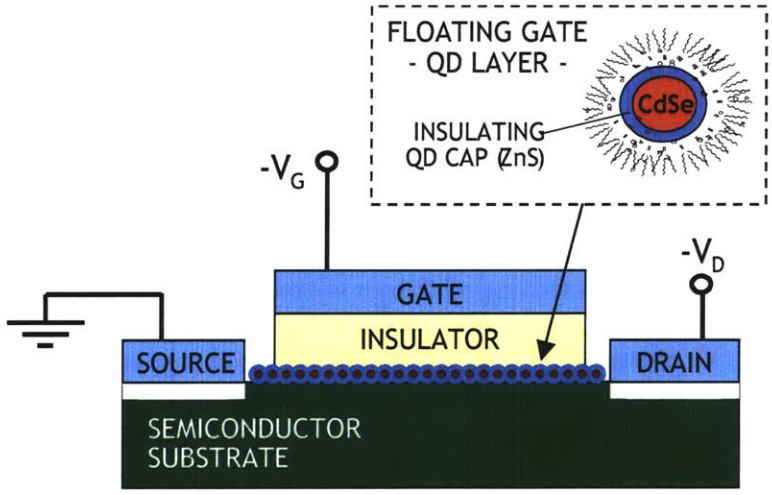

Figure 7-4: Cross-sectional depiction of a QD based floating gate non-volatile memory. The floating gate is comprised of a single monolayer of hexagonally close packed QDs, which are electrically isolated from each other and from the channel by the insulating shell and capping molecule layers of the QD. Charges are stored separately on each QD, and discharging any one QD in the monolayer will not discharge the neighboring QDs, yielding better storage properties as compared to a laterally conducting floating gate material.

7.8 QD Nanopatterning

Another non-light emitting project which follows from this work is the use of QD monolayers as a mask for extremely high resolution (~5nm) nanopatterning. Our ability to create hexagonally close packed (hcp), large area grains of QDs has already been detailed in Section 3. If we consider that this layer is essentially an extremely thin layer of ordered material with alternating inorganic (core) and organic (capping molecules) components, it becomes clear that under the appropriate conditions this may be a highly selective etch mask for the substrate we deposit onto. An example of a process flow which utilizes this approach is shown in Figure 7-5.

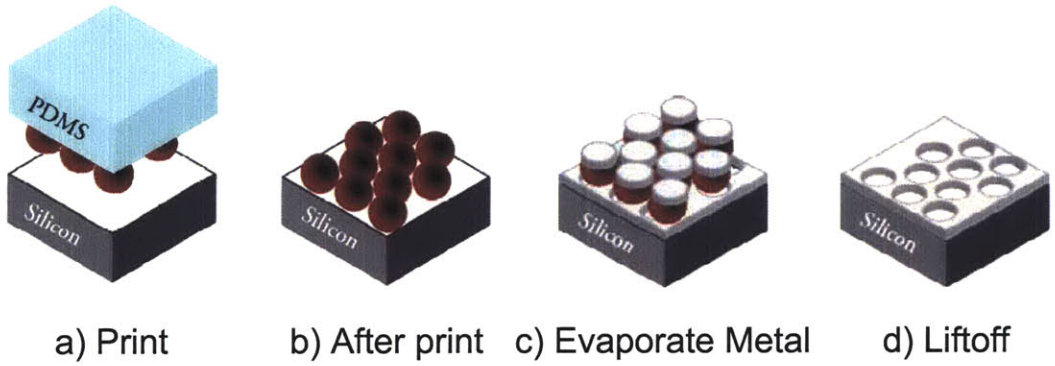

Figure 7-5: One possible process flow utilizing a QD monolayer as a nanopatterning mask. First, a QD monolayer is printed onto the substrate to be patterned (a), resulting in (b). Then a thin film of a different material (in this case metal) is directionally deposited onto and through the QD layer (c). Using a solvent, the QDs can then be lifted off along with the metal that was deposited on top of the QDs, leaving behind a nanopatterned thin film of metal(d). This pattern can then be transferred to the substrate using a variety of selective etching techniques.

This work has been ongoing for over a year since the initial proof of concept was performed. While it was relatively simple to show that a 100nm grain of QDs was an effective oxygen plasma etch mask, finding an etching technique that would preserve the much finer interstitial features of the QD hcp monolayer has been challenging. Both the small feature sizes and the thin film of masking material have to date prevented the

discovery of a process that preserves the 5-10nm periodicity that we can observe of the QD monolayer using AFM.

8 Funding Sources

We are grateful to Universal Display Corporation, the U.S. Army through the Institute for Soldier Nanotechnologies, under Contract DAAD-19-02-0002 with the U.S. Army Research Office, and NSF MRSEC program (DMR 0213282) for their support of this research.

9 Appendices

A Growth Equipment Design

A.1 Integrated Material Growth System

Equipment needs have been central to the successful completion of this project. Starting the work in a new laboratory this was necessarily the case, but was further complicated by the constraints inherent in making QD-LEDs. Furthermore, at the project's onset, we could only guess as to what those constraints might be, and as such may have erred on the side of over designing the system. From prior experience in OLED development, we were aware of the importance of isolating water vapor and oxygen from our devices. We assumed that this would also be the case for the QD-LEDs, since our QD-LEDs would incorporate organic transport layers subject to the same limitations as OLEDs. As such, we set out to develop a complete growth system (see Figure 9-1) that would allow the creation of a multilayer organic and QD device without exposure to air. In addition, it was desirable to have as little exposure to atmospheric pressure as possible.

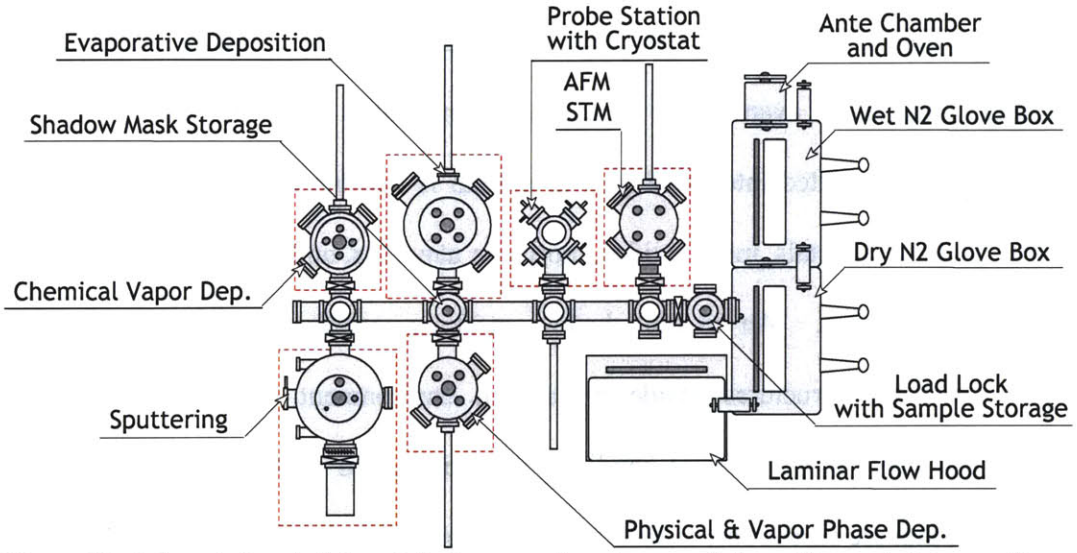

Figure 9-1: Integrated materials and devices growth system consisting of the materials growth chambers based on physical and vapor phase deposition, sputtering, chemical vapor deposition, and evaporative deposition with in-situ shadow masking. Samples are analyzed in the analytical and AFM/STM chambers, and all connected to the central transfer line with load lock and an integrated, nitrogen-filled glove box.

The necessary components of such a system are a solution processing area for spin-coating and any other non-aqueous wet processing techniques, an area for device manipulation, some allowance for shadow masking, and a thermal evaporator. In addition, we anticipated that an ideal system might include a new method of vacuum depositing QDs, a sputtering system for production of transparent cathodes, and a probing station for vacuum testing of our completed devices. Integrating such a large set of chambers into one system was a clear challenge, and led us to spend a significant time designing the backbone of the system, the linear transfer line. In addition, considerable effort has been expended on the creation of a Misted Solution Transport (MiST) deposition chamber that we expected will solve the problem of vacuum deposition of QDs, but this challenge is as yet not completed.

The completed growth system integrates the known methods for physical vapor phase deposition of organic and inorganic thin-films, including a low-pressure RF/DC sputtering chamber, an evaporative growth chamber, and a chemical vapor deposition chamber. The completed integrated growth system is capable of depositing molecular organics, polymers, metals, metal oxides, inorganic nanodots, and colloids in a controlled layer-by-layer fashion. An in-situ shadow masking system enables fabrication of complex patterned structures inside a vacuum environment, while the integrated N_2-filled, dry glove box facilitates handling, measuring, and packaging of organic thin film samples that are susceptible to reactions with atmospheric oxygen and water vapor.

All chambers are connected to the central transfer system that has linear degrees of freedom. Each chamber is isolated form the others by a gate valve resulting in typical base and operating pressures as indicated below. Maximum substrate size is 10 cm with a 5% variation in the thickness and composition of deposited films over the substrate area. Presently the system consists of the double glove box, evaporator, the sputtering system, a Knudson cell thermal evaporator, and the transfer line with the load lock, while chambers for electron beam evaporation, and chemical vapor deposition are in the process of being built and integrated. The operating and base pressure for each chamber on the system are summarized in Table 9-1.

SYSTEM	Base Pressure [Torr]	Operating Pressure [Torr]
Sputtering	10^{-9}	10^{-3} to 10^{1}
Evaporative	10^{-10}	10^{-9}
CVD	10^{-8}	1 to 10
Central Transfer	10^{-9}	10^{-7} to 10^{-9}
Load Lock	10^{-7}	10^{-7} to atmosphere

Table 9-1: Vacuum chamber pressure specifications for linear transfer system.

A.2 Transfer System Design

With our need for a sophisticated transfer system well established, we started to establish its design criterion. The line would need to fit within the space available to us, integrate at least five chambers as well as a loadlock to a glove box, and provide a means for in-situ shadow masking. Finally, the system should be designed for ease of use, and as fool-proof as possible, to maximize up time and minimize the skill level needed to be a user of the facility.

The method of handling the typical fragile shadow masks within stainless steel vacuum chambers was a challenge in and of itself. We will summarize our solution to this challenge with a picture of the end result, Figure 9-2. This two piece stack allows the separate handling and storage of shadow masks, which can then be self-aligned within ultra-high vacuum conditions to contact mask substrates loaded into the substrate holder.

The typical alignment is accurate and repeatable to within 100μm, which is more than adequate for the laboratory pixel masks that are used within the system. This alignment is achieved by the chamfer of two sets of opposing teeth on the shadow mask holder and the substrate holder, ensuring proper rotation relative to each other, as well as allowing for contact between the mask and the substrate. In practice, this system allows the user to grow both patterned and unpatterned layers in succession, without exposure to atmosphere, and without waiting for long vent and pump-down cycles between layers. This is critical to device performance, as even in a Nitrogen environment glove box, oxygen and water molecules are present in low concentration, and can adhere to the surface of an organic thin film within minutes. Inclusion of such reactive impurities into a device is immediately noticeable as reduced quantum efficiency of an OLED.

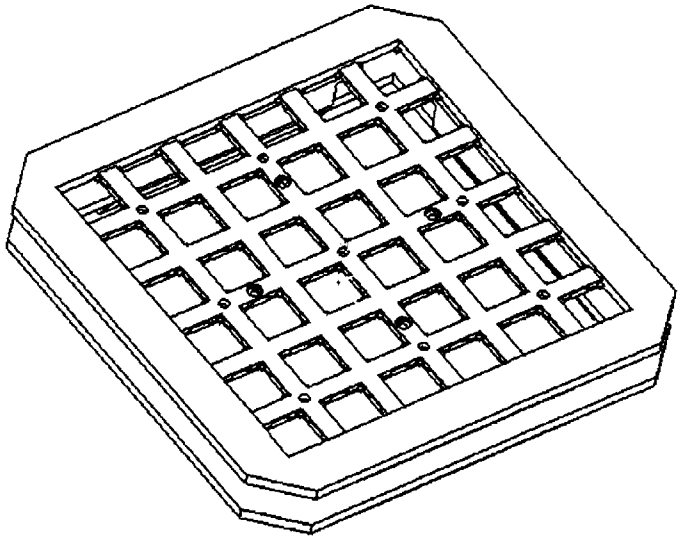

Figure 9-2: Solidworks drawing of the substrate holder and shadow mask holder self-aligned stack. This example holds ½" substrates, our most typical substrate size.

The design of the transfer line and all of its parts and components was done using the computer aided design tool Solidworks. All of the design was performed in house, while the parts were machined and assembled in local machine shops specializing in vacuum equipment. Figure 9-3 and Figure 9-4 show four external views of the finished design as well as a photograph of the actual system installed in the lab. The difficult portion of the transfer line design is in the details of alignment of transfer points. It allows transfer of substrates and shadow masks over distances of 13 feet, and yet the freedom of motion of any of the mating parts is at most 1/8 of an inch. This is so that there can be minimal strain on any given part, which will in turn minimize wear and bending of the precision machined parts. Two good examples of this precision are in the loadlock handoff and in the lateral fork handoff. Exemplary drawings are shown in Figure 9-5 and Figure 9-6. A loadlock enables the loading and unloading of substrate chucks to take place in much less time, as only the first 18" of the chamber must be vented and then restored to vacuum. However, this means that the caboose piece (shown in Figure 9-5) which carries the substrates to the various chambers must be able to cross the 3" gap in the rail system which allows the gate valve to isolate the load lock from the remainder of the transfer line.

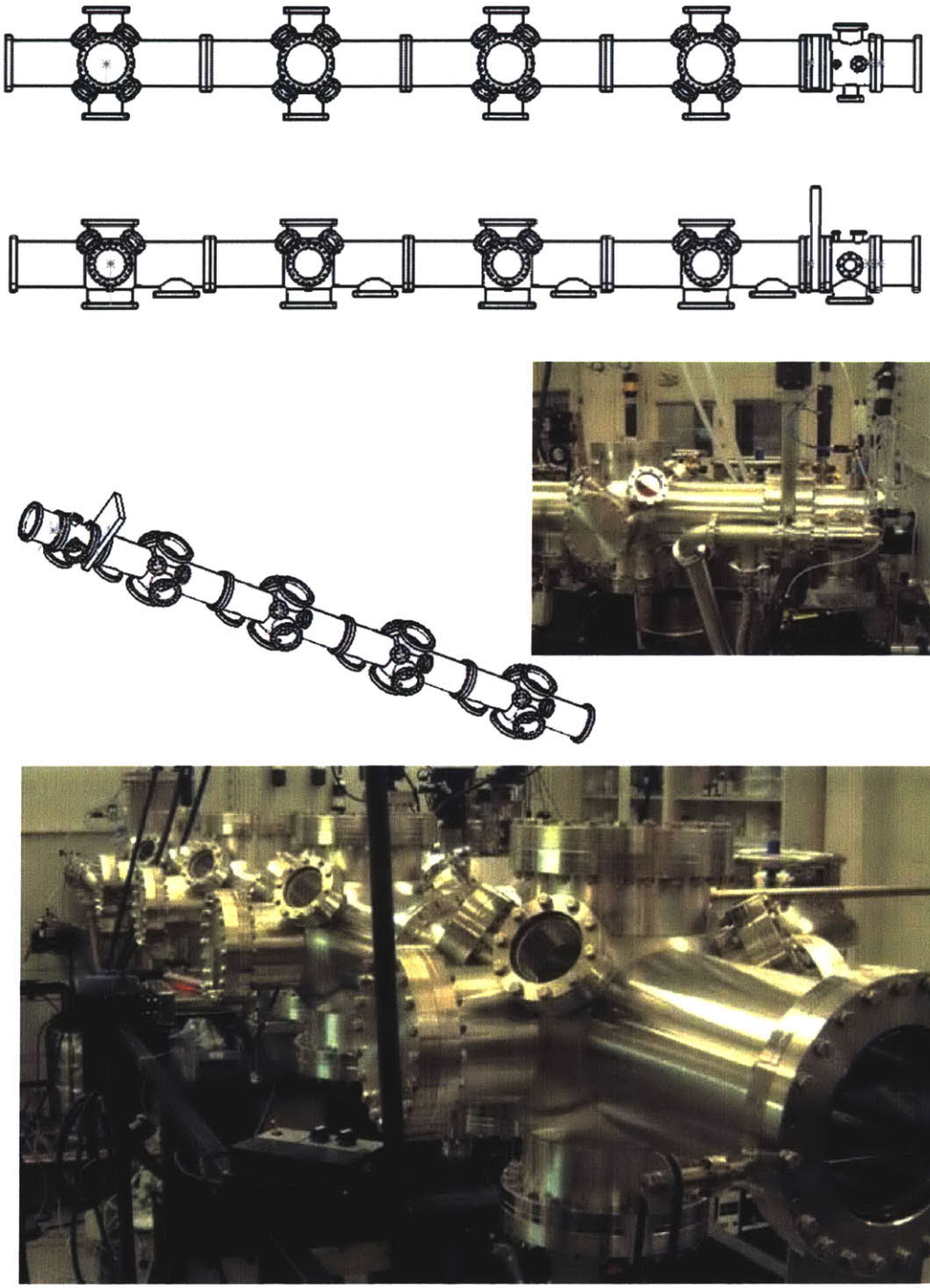

Figure 9-3: Solidworks drawings of the transfer line in various orientations. Two photos showing the actual 12' line in our lab are also included.

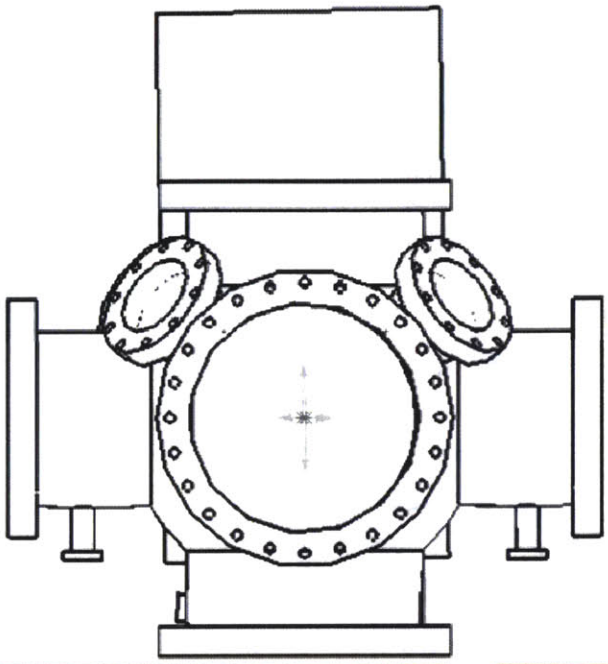

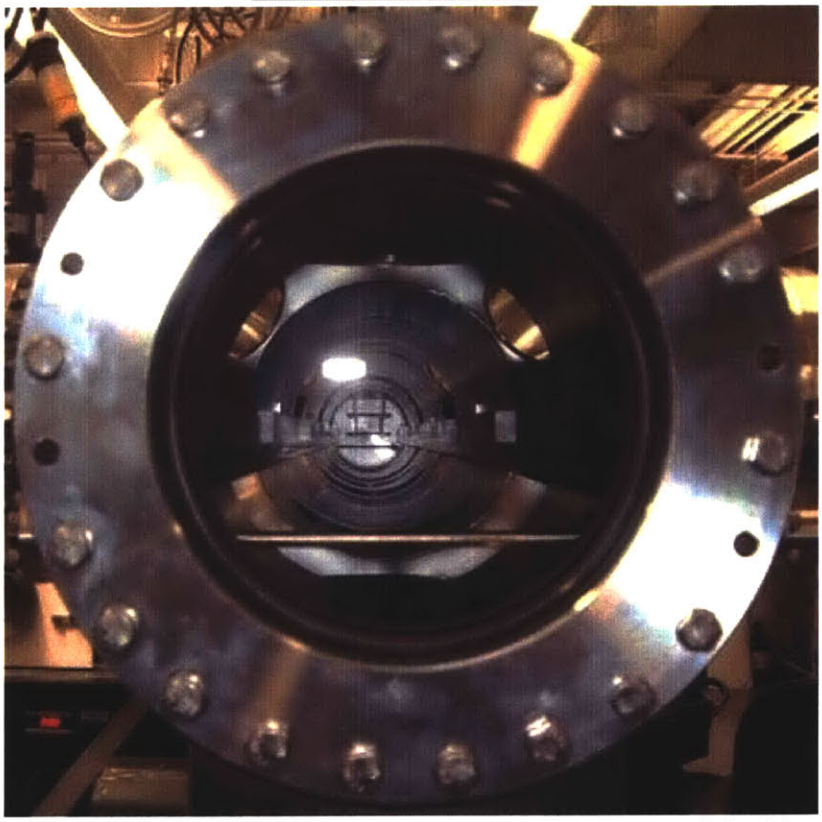

Figure 9-4: Solidworks endview drawing of the transfer line. The photograph is of the system from the same orientation. Note the rails and the shadow mask holder stack that allows for in-situ masking of substrates.

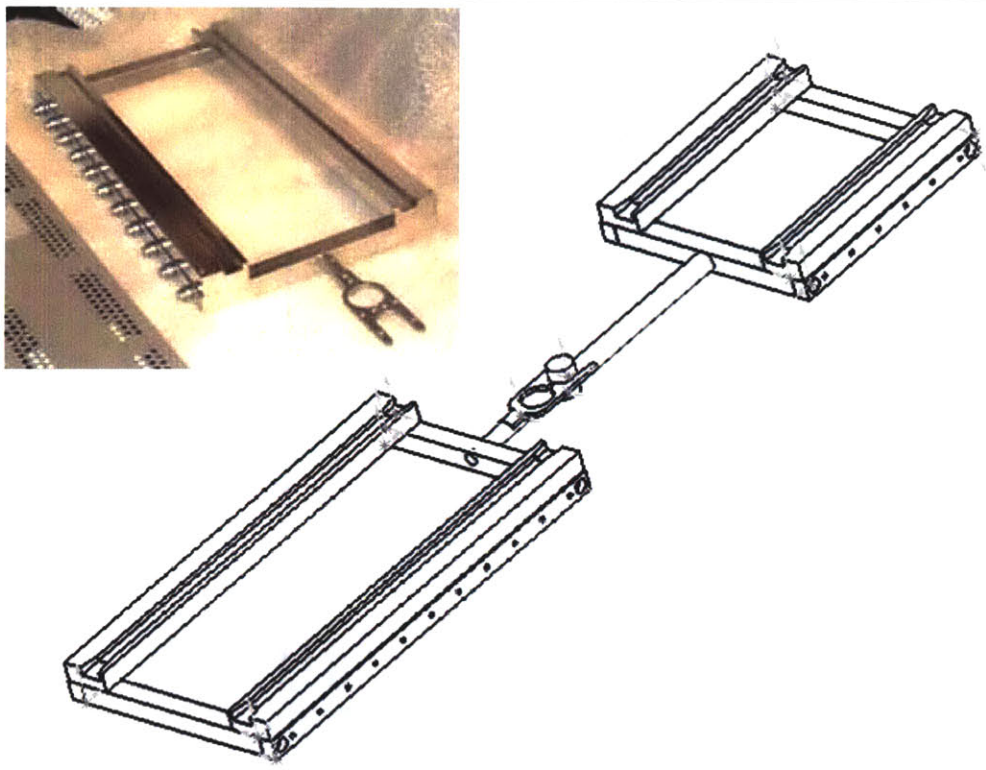

Figure 9-5: Photograph of the caboose that rides the rails of the 13' chamber, and transports the substrate holders and shadow mask holders. Solidworks view of both the engine and the caboose in their ''hand-off' configuration.

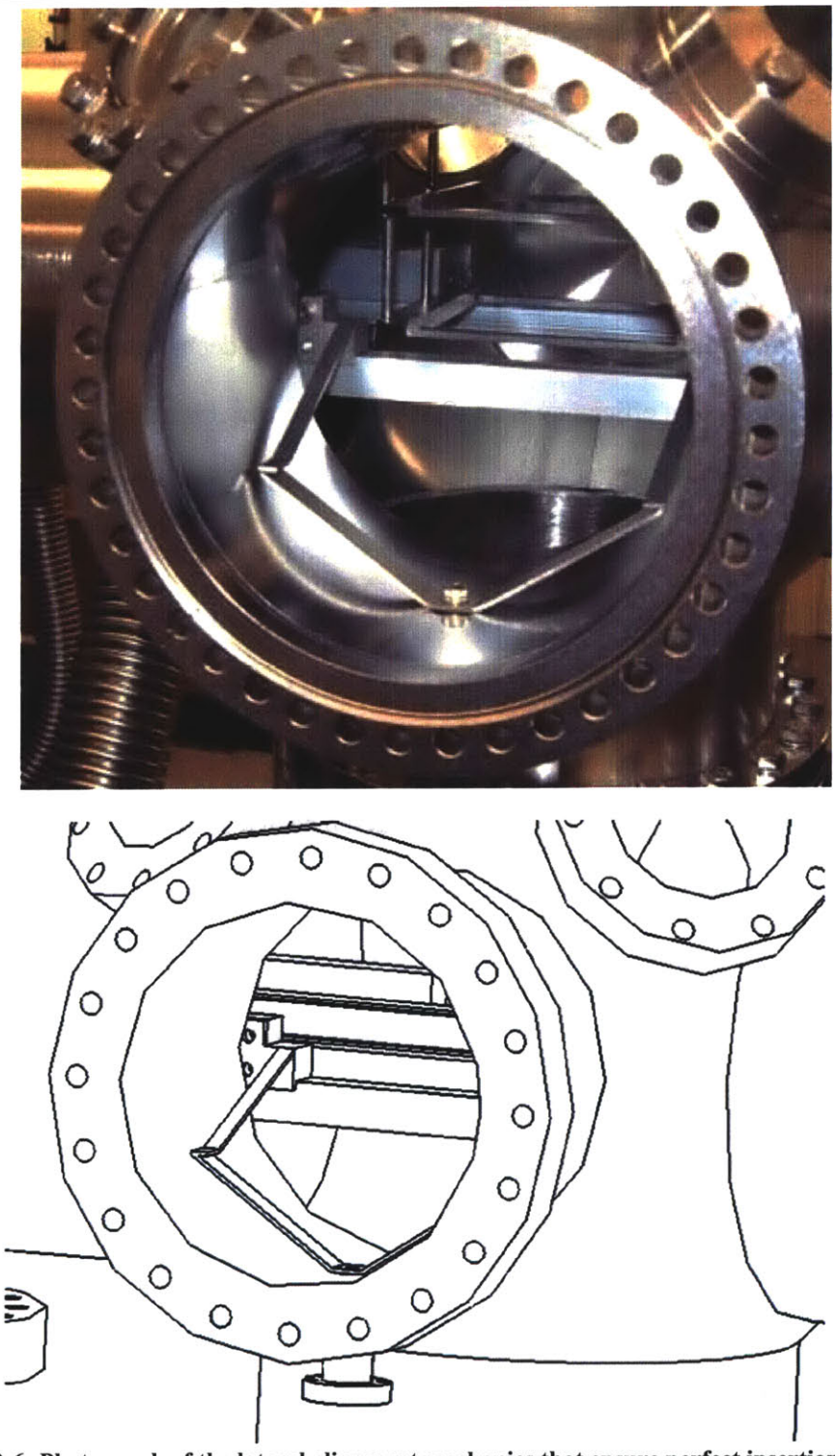

Figure 9-6: Photograph of the lateral alignment mechanics that ensure perfect insertion of the transfer fork into the substrate holder. Solidworks perspective view of the same.

B LED Parameter Calculations

B.1 External Quantum Efficiency

The external quantum efficiency of an LED is defined as the number of photons emitted from the entire device structure per charge carrier injected into the device. This is the metric of choice throughout this work as it most accurately reflects device efficiency with the minimum of assumptions and less relevant dependencies. For example, internal quantum efficiency is an oft cited metric, but it is calculated using external quantum efficiency and a set of assumptions regarding how many of the internally generated photons can escape the device structure. Luminous efficiency (cd/A) is also a useful metric for display applications, but is not relevant in the infrared and has a large color dependence that makes comparing blue LEDs to green LEDs difficult.

To calculate the external quantum efficiency of an LED[111, 130], first involves measuring the luminous intensity, L_0, emitted from the device surface, with units of joules per second. This is done with a calibrated Silicon photodiode purchased from Newport Optics. While it is possible to convert the output of this photodiode into a voltage by means of the vendor supplied amplifier box, it is not desirable to do so as it introduces multiple additional sources of error into the experiment. Without amplification, the output of the photodiode is a photocurrent, I_{det}. Then:

$$L_0 = \frac{I_{\det} \bullet \lambda}{\eta_{\det} \bullet f \bullet 1241}$$ **Equation 9-1**

Where $\eta_{det}(\lambda)$ is the efficiency of the detector at a given wavelength in amps per Watt (provided in a look-up table by the vendor), f is a coupling factor taking into account the fraction of light emitted by the LED that is measured by the photodiode, and λ is the center wavelength of the emission spectrum. The term $(1241/\lambda)$ gives the energy of a

photon of a given wavelength in units eV, and is necessary to convert the light output from units of Watts into a number of (Coulombs of) photons.

It is common to use the assumption that an OLED is a perfect Lambertian emitter, and then use very low values of f for convenience of measurement. However, this assumption can lead to significant errors, as light emission from OLEDs is in fact subject to weak micro-cavity effects[83] that can alter this emission profile. In practice then, it is desirable to use as large a value for f as is possible, which leads to the use of large area photodetectors (1 cm in diameter) that are in close proximity to the device substrate (within a few mm). For the standard half inch test substrate used in this work, our value of f is 0.94.

With L_0 determined, external quantum efficiency (η_{EX}) is simply:

$$\eta_{EX} = \frac{L_0}{I_{OLED}} \qquad \textbf{Equation 9-2}$$

Where I_{OLED} is the current injected into the device as measured by an ammeter (in this case an HP 4156 Parameter Analyzer, simultaneously measuring I_{det}).

Equations 10-1 and 10-2 can be stated more rigorously as:

$$\eta_{EX} = \frac{\int \lambda I_{\det}(\lambda) d\lambda}{f I_{OLED} \int \lambda \eta_{\det}(\lambda) d\lambda} \qquad \textbf{Equation 9-3}$$

Where we take into account the wavelength dependence of the photodiode efficiency. In practice this is not a necessary complication, as the silicon photodiode efficiency versus wavelength is quite linear, and is well-approximated for narrow-band Gaussians by taking the value for the center wavelength of the device spectrum.

B.2 Luminous Efficiency

Converting η_{EX} to units of either lumens (luminous flux, lm) or candelas (1 lumen per steradian, cd) requires taking into account the response of the human eye to light of

various wavelength. The photopic response, g(λ) of the human eye (shown earlier in Figure 1-3) peaks at 555 nm at $\phi_0 = 683$ lm/$W_{optical}$ and falls off sharply in the blue and red. Thus, the luminous power efficiency can be written:

$$\eta_P = \frac{\phi_0 \int g(\lambda) I_{det}(\lambda) / R(\lambda) d\lambda}{f I_{OLED} V} \qquad \textbf{Equation 9-4}$$

Where $R(\lambda) = q\lambda\eta_{det}/hc$ is the photodiode responsivity, and V is the LED drive voltage. For a Lambertian source emitting into the half plane, 1lm = π cd, making conversions to cd/A or cd/m^2 simple mathematical manipulations.

References

1. J. Col. "Enchanted Learning." http://www.EnchantedLearning.com, 2000.

2. C. W. Tang and S. A. Vanslyke, "Organic Electroluminescent Diodes", *Applied Physics Letters*, **51**, 913-915, 1987.

3. N/A. "Television History." http://www.ideafinder.com/history/inventions/story085.htm, 1997.

4. J. Tyson. "How LCDs work." http://electronics.howstuffworks.com/lcd.htm, 1998.

5. M. Pope and C. Swenberg, "Electronic Processes in Organic Crystals and Polymers", Oxford University Press, New York, 1999.

6. B. G. Streetman, "Solid State Electronic Devices: Fourth Edition", Prentice Hall, Upper Saddle River, NJ, 1995.

7. C. W. Tang, "2-Layer Organic Photovoltaic Cell", *Applied Physics Letters*, **48**, 183-185, 1986.

8. V. G. Kozlov, et al., "Laser action in organic semiconductor waveguide and double-heterostructure devices", *Nature*, **389**, 362-364, 1997.

9. P. Peumans, et al., "Efficient, high-bandwidth organic multilayer photodetectors", *Applied Physics Letters*, **76**, 3855-3857, 2000.

10. M. A. Hines and P. Guyot-Sionnest, "Synthesis and characterization of strongly luminescing ZnS-Capped CdSe nanocrystals", *Journal of Physical Chemistry*, **100**, 468-471, 1996.

11. G. Gu, et al., "Vacuum-deposited, nonpolymeric flexible organic light-emitting devices", *Optics Letters*, **22**, 172-174, 1997.

12. G. Parthasarathy, et al., "A metal-free cathode for organic semiconductor devices", *Applied Physics Letters*, **72**, 2138-2140, 1998.

13. M. A. Baldo, et al., "Highly efficient phosphorescent emission from organic electroluminescent devices", *Nature*, **395**, 151-154, 1998.

14. D. Braun, et al., "Improved Efficiency In Semiconducting Polymer Light-Emitting-Diodes", *Journal of Electronic Materials*, **20**, 945-948, 1991.

15. V. Bulovic, et al., "Molecular organic light-emitting devices", *Electroluminescence I*, **64**, 255-306, 2000.

16. C. Adachi, et al., "High-efficiency red electrophosphorescence devices", *Applied Physics Letters*, **78**, 1622-1624, 2001.

17. T. Yamasaki, et al., "Organic light-emitting device with an ordered monolayer of silica microspheres as a scattering medium", *Applied Physics Letters*, **76**, 1243-1245, 2000.

18. S. Moller and S. R. Forrest, "Improved light out-coupling in organic light emitting diodes employing ordered microlens arrays", *Journal of Applied Physics*, **91**, 3324-3327, 2002.

19. S. Dirr, et al., "Organic light emitting diodes with reduced spectral and spacial halfwidths", *Japanese Journal of Applied Physics Part 1-Regular Papers Short Notes & Review Papers*, **37**, 1457-1461, 1998.

20. B. W. D'Andrade, et al., "Controlling exciton diffusion in multilayer white phosphorescent organic light emitting devices", *Advanced Materials*, **14**, 147-+, 2002.

21. Z. N. Bao, et al., "Molecular ordering through molecular design and surface modification and their electrical and optical devices." *Abstracts of Papers of the American Chemical Society*, **220**, U367-U367, 2000.

22. Z. D. Popovic, et al., "Long-term degradation mechanism of tris(8-hydroxyquinoline) aluminum-based organic light-emitting devices", *Synthetic Metals*, **111**, 229-232, 2000.

23. J. J. Ho, "Dramatically improved lifetime operation and luminous efficiency for flexible organic light-emitting devices by oxygen plasma and nitrogen treatments", *Electronics Letters*, **39**, 458-460, 2003.

24. M. Ben Khalifa, et al., "Opposing influence of hole blocking layer and a doped transport layer on the performance of heterostructure OLEDs", *Org Electron*, **5**, 187-198, 2004.

25. G. Parthasarathy, et al., "Lithium doping of semiconducting organic charge transport materials", *J. Appl. Phys.*, **89**, 4986-4992, 2001.

26. C. F. Madigan and V. Bulovic, "Solid state solvation in amorphous organic thin films", *Phys Rev Lett*, **91**, 2003.

27. M. A. Baldo, et al., "Low pressure organic vapor phase deposition of small molecular weight organic light emitting device structures", *Applied Physics Letters*, **71**, 3033-3035, 1997.

28. M. Baldo, et al., "Organic vapor phase deposition", *Applied Physics Letters*, **10**, 1505-+, 1998.

29. M. Shtein, et al., "Material transport regimes and mechanisms for growth of molecular organic thin films using low-pressure organic vapor phase deposition", *J. Appl. Phys.*, **89**, 1470-1476, 2001.

30. M. Shtein, et al., "Micropatterning of small molecular weight organic semiconductor thin films using organic vapor phase deposition", *J. Appl. Phys.*, **93**, 4005-4016, 2003.

31. L. Mizuho Securities Co., "Organic EL Industry", 2004.

32. L. Ke, et al., "Organic light emitting devices performance improvement by inserting thin parylene layer", *Synthetic Metals*, **140**, 295-299, 2004.

33. E. I. Mal'tsev, et al., "Electroluminescence of polymer/J-aggregate composites", *Applied Physics Letters*, **75**, 1896-1898, 1999.

34. Y. Shirota, et al., "Thermally stable organic light-emitting diodes using new families of hole-transporting amorphous molecular materials", *Synthetic Metals*, **111**, 387-391, 2000.

35. C. W. Tang, et al., "Electroluminescence of Doped Organic Thin-Films", *Journal of Applied Physics*, **65**, 3610-3616, 1989.

36. C. W. Tang, *Society for Information Display, International Symposium, Digest of Technical Papers*, **27**, 181, 1996.

37. V. Bulovic, et al., "Transform-limited, narrow-linewidth lasing action in organic semiconductor microcavities", *Science*, **279**, 553-555, 1998.

38. Y. Yang, et al., "Organic/polymeric electroluminescent devices processed by hybrid ink-jet printing", *Journal of Materials Science: Materials in Electronics*, **11**, 89-96, 2000.

39. R. Rossetti, et al., "Quantum Size Effects in the Redox Potentials, Resonance Raman Spectra, and Electronic Spectra of CdS Crystallites in Aqueous Solution", *J Chem Phys*, **79**, 1086-1088, 1983.

40. C. B. Murray, et al., "Synthesis and Characterization of Nearly Monodisperse Cde (E = S, Se, Te) Semiconductor Nanocrystallites", *J Am Chem Soc*, **115**, 8706-8715, 1993.

41. R. Dettmer, "The Quest for the Quantum Dot", *IEEE Review*, **34**, 395-397, 1988.

42. B. O. Dabbousi, et al., "(CdSe)ZnS core-shell quantum dots: Synthesis and characterization of a size series of highly luminescent nanocrystallites", *Journal of Physical Chemistry B*, **101**, 9463-9475, 1997.

43. S. Rosenthal, "A Quantum Dot Nanoconjugate Tollbox", *MRS Symposium, Spring 2004*, **M7.2**, 2004.

44. A. Efros and M. Rosen, "The Electronic Structure of Semiconductor Nanocrystals", *Annu Rev Mater Sci*, **30**, 475-521, 2000.

45. A. Efros and A. Efros, *Sov. Phys. Semicond.*, **16**, 772-778, 1982.

46. L. E. Brus, *J Chem Phys*, **79**, 5566-5571, 1983.

47. C. MURRAY, et al., "SYNTHESIS AND CHARACTERIZATION OF NEARLY MONODISPERSE CDE (E = S, SE, TE) SEMICONDUCTOR NANOCRYSTALLITES", *J Am Chem Soc*, **115**, 8706-8715, 1993.

48. A. I. Ekimov, et al., *SOLID STATE COMMUN*, **56**, 921-924, 1985.

49. J. M. Luttinger and W. Kohn, *Physical Review*, **97**, 869-883, 1955.

50. G. B. Grigoryan, et al., *Sov. Phys. Solid State*, **32**, 1031-1035, 1990.

51. C. R. Pidgeon and R. N. Brown, *Physical Review*, **146**, 575-583, 1966.

52. A. Efros, *Physical Review B*, **46**, 7448-7458, 1992.

53. A. Efros and A. V. Rodina, *Physical Review B*, **47**, 10005-10007, 1993.

54. A. Efros, et al., "Band-edge exciton in quantum dots of semiconductors with a degenerate valence band: Dark and bright exciton states", *PHYSICAL REVIEW B*, **54**, 4843-4856, 1996.

55. M. Nirmal, et al., "Fluorescence intermittency in single cadmium selenide nanocrystals", *NATURE*, **383**, 802-804, 1996.

56. R. Neuhauser, et al., "Correlation between fluorescence intermittency and spectral diffusion in single semiconductor quantum dots", *Phys Rev Lett*, **85**, 3301-3304, 2000.

57. K. Shimizu, et al., "Blinking statistics in single semiconductor nanocrystal quantum dots", *PHYSICAL REVIEW B*, **6320**, art. no.-205316, 2001.

58. V. Klimov, et al., "Quantization of multiparticle Auger rates in semiconductor quantum dots", *Science*, **287**, 1011-1013, 2000.

59. V. L. Colvin, et al., "Light-Emitting-Diodes Made from Cadmium Selenide Nanocrystals and a Semiconducting Polymer", *Nature*, **370**, 354-357, 1994.

60. M. C. Schlamp, et al., "Improved efficiencies in light emitting diodes made with CdSe(CdS) core/shell type nanocrystals and a semiconducting polymer", *J. Appl. Phys.*, **82**, 5837-5842, 1997.

61. E. H. Sargent, *Nature Materials*, 2005.

62. X. M. Lin, et al., "Formation of long-range-ordered nanocrystal superlattices on silicon nitride substrates", *J Phys Chem B*, **105**, 3353-3357, 2001.

63. F. Redl, et al., "Three-dimensional binary superlattices of magnetic nanocrystals and semiconductor quantum dots", *NATURE*, **423**, 968-971, 2003.

64. V. Santhanam, et al., "Self-assembly of uniform monolayer arrays of nanoparticles", *Langmuir*, **19**, 7881-7887, 2003.

65. M. Islam and I. Herman, "Electrodeposition of patterned CdSe nanocrystal films using thermally charged nanocrystals", *APPLIED PHYSICS LETTERS*, **80**, 3823-3825, 2002.

66. V. Santhanam and R. P. Andres, "Microcontact printing of uniform nanoparticle arrays", *Nano Lett*, **4**, 41-44, 2004.

67. S. Bae, et al., "Selectively assembled Co nanoparticle stripes prepared by covalent linkage and microcontact printing", *J Phys Chem B*, **108**, 2575-2579, 2004.

68. B. O. Dabbousi, et al., "Electroluminescence from CdSe Quantum-Dot Polymer Composites", *Applied Physics Letters*, **66**, 1316-1318, 1995.

69. H. Mattoussi, et al., "Electroluminescence from heterostructures of poly(phenylene vinylene) and inorganic CdSe nanocrystals", *J. Appl. Phys.*, **83**, 7965-7974, 1998.

70. H. Mattoussi, et al., "Composite thin films of CdSe nanocrystals and a surface passivating/electron transporting block copolymer: Correlations between film microstructure by transmission electron microscopy and electroluminescence", *J. Appl. Phys.*, **86**, 4390-4399, 1999.

71. N. Tessler, et al., "Efficient near-infrared polymer nanocrystat light-emitting diodes", *Science*, **295**, 1506-1508, 2002.

72. S. Coe, et al., "Electroluminescence from single monolayers of nanocrystals in molecular organic devices", *NATURE*, **420**, 800-803, 2002.

73. S. Coe-Sullivan, et al., "Tuning the performance of hybrid organic/inorganic quantum dot light-emitting devices", *Org Electron*, **4**, 123-130, 2003.

74. H. Mattoussi, et al., "Composite thin films of CdSe nanocrystals and a surface passivating/electron transporting block copolymer: Correlations between film microstructure by transmission electron microscopy and electroluminescence", *Journal of Applied Physics*, **86**, 4390-4399, 1999.

75. H. Mattoussi, et al., "Electroluminescence from heterostructures of poly(phenylene vinylene) and inorganic CdSe nanocrystals", *Journal of Applied Physics*, **83**, 7965-7974, 1998.

76. S. Coe, et al., "Electroluminescence from single monolayers of nanocrystals in molecular organic devices", *Nature*, **420**, 800-803, 2002.

77. S. Coe-Sullivan, et al., "Tuning the performance of hybrid organic/inorganic quantum dot light-emitting devices", *Org Electron*, **4**, 123-130, 2003.

78. S. Coe-Sullivan, et al., "Large Area Ordered Quantum Dot Monolayers via Phase Separation During Spin-Casting ", *Advanced Functional Materials*, **in press**, 2005.

79. C. TANG and S. VANSLYKE, "ORGANIC ELECTROLUMINESCENT DIODES", *APPLIED PHYSICS LETTERS*, **51**, 913-915, 1987.

80. C. A. Leatherdale, et al., "Photoconductivity in CdSe quantum dot solids", *Physical Review B*, **62**, 2669-2680, 2000.

81. V. I. Klimov and D. W. McBranch, "Femtosecond 1P-to-1S electron relaxation in strongly confined semiconductor nanocrystals", *Physical Review Letters*, **80**, 4028-4031, 1998.

82. C. Adachi, et al., "Architectures for efficient electrophosphorescent organic light-emitting devices", *IEEE J SEL TOP QUANT*, **8**, 372-377, 2002.

83. V. Bulovic, et al., "Weak microcavity effects in organic light-emitting devices", *PHYSICAL REVIEW B*, **58**, 3730-3740, 1998.

84. C. TANG, et al., "ELECTROLUMINESCENCE OF DOPED ORGANIC THIN-FILMS", *J. Appl. Phys.*, **65**, 3610-3616, 1989.

85. C. Adachi, et al., "Electroluminescent mechanism of organic multilayer thin film devices", *Optoelectronic - Devices and Technologies*, **6**, 25-36, 1991.

86. V. Bulovic, et al., "Molecular organic light-emitting devices", *ELECTROLUMINESCENCE I*, **64**, 255-306, 2000.

87. Forster, *Ann. Phys.*, **2**, 55, 1949.

88. V. Bulovic and S. R. Forrest, "Polymeric and molecular organic light emitting devices: A comparison", *Semiconduct Semimet*, **65**, 1-26, 2000.

89. C. E. Finlayson, et al., "Enhanced Forster energy transfer in organic/inorganic bilayer optical microcavities", *Chem Phys Lett*, **338**, 83-87, 2001.

90. D. Norris, et al., "Size dependence of exciton fine structure in CdSe quantum dots", *PHYSICAL REVIEW B*, **53**, 16347-16354, 1996.

91. L. Manna, et al., "Synthesis of soluble and processable rod-, arrow-, teardrop-, and tetrapod-shaped CdSe nanocrystals", *J Am Chem Soc*, **122**, 12700-12706, 2000.

92. C. B. Murray, et al., "Self-Organization of CdSe Nanocrystallites into Three-Dimensional Quantum Dot Superlattices", *Science*, **270**, 1335-1338, 1995.

93. B. O. Dabbousi, et al., "Langmuir-Blodgett Manipulation of Size-Selected Cdse Nanocrystallites", *Chem Mater*, **6**, 216-219, 1994.

94. C. P. Collier, et al., "Reversible tuning of silver quantum dot monolayers through the metal-insulator transition", *Science*, **277**, 1978-1981, 1997.

95. J. S. Steckel, et al., "1.3 mu m to 1.55 mu m tunable electroluminescence from PbSe quantum dots embedded within an organic device", *Adv Mater*, **15**, 1862-1866, 2003.

96. J. Tang, et al., "Gas-liquid-solid phase transition model for two-dimensional nanocrystal self-assembly on graphite", *J Phys Chem B*, **106**, 5653-5658, 2002.

97. A. Lo and R. T. Skodje, "Kinetic and Monte Carlo models of thin film coarsening: Cross over from diffusion-coalescence to Ostwald growth modes", *J Chem Phys*, **112**, 1966-1974, 2000.

98. N. Jana, "Shape Effect in Nanoparticle Self-Assembly", *Angew. Chem. Int. Ed.*, **43**, 1536-1540, 2004.

99. S. Connolly, et al., "Time-resolved small-angle X-ray scattering studies of nanocrystal superlattice self-assembly", *J Am Chem Soc*, **120**, 2969-2970, 1998.

100. E. Rabani, et al., "Drying-mediated self-assembly of nanoparticles", *Nature*, **426**, 271-274, 2003.

101. H. Tanaka, "Viscoelastic phase separation", *J Phys-Condens Mat*, **12**, R207-R264, 2000.

102. M. Maillard, et al., "Rings and hexagons made of nanocrystals", *Adv Mater*, **13**, 200-204, 2001.

103. B. A. Korgel and D. Fitzmaurice, "Condensation of ordered nanocrystal thin films", *Phys Rev Lett*, **80**, 3531-3534, 1998.

104. K. Morgenstern, et al., "Decay of two-dimensional Ag islands on Ag(111)", *Phys Rev Lett*, **76**, 2113-2116, 1996.

105. J. M. Wen, et al., "Coarsening mechanisms in a metal film: From cluster diffusion to vacancy ripening", *Phys Rev Lett*, **76**, 652-655, 1996.

106. G. L. Ge and L. E. Brus, "Fast surface diffusion of large disk-shaped nanocrystal aggregates", *Nano Lett*, **1**, 219-222, 2001.

107. R. Curry, et al., "1.5 mu m electroluminescence from organic light emitting diodes integrated on silicon substrates", *OPT MATER*, **17**, 161-163, 2001.

108. Y. Kawamura, et al., "Near-infrared electroluminescence from ytterbium(III) complex", *CHEM LETT*, 280-281, 2000.

109. R. CHANCE, et al., "LIFETIME OF AN EMITTING MOLECULE NEAR A PARTIALLY REFLECTING SURFACE", *J Chem Phys*, **60**, 2744-2748, 1974.

110. C. Leatherdale, et al., "Photoconductivity in CdSe quantum dot solids", *PHYSICAL REVIEW B*, **62**, 2669-2680, 2000.

111. S. Forrest, et al., "Measuring the Efficiency of Organic Light Emitting Devices", *Adv Mater*, **15**, 1043-1048, 2005.

112. J. Sturm, et al., "Thermal effects and scaling in organic light-emitting flat-panel displays", *IEEE J SEL TOP QUANT*, **4**, 75-82, 1998.

113. D. O'Brien, et al., "Hole transporting materials with high glass transition temperatures for use in organic light-emitting devices", *Adv Mater*, **10**, 1108-+, 1998.

114. C. R. Barry, et al., "Printing nanoparticle building blocks from the gas phase using nanoxerography", *Applied Physics Letters*, **83**, 5527-5529, 2003.

115. X. Lin, et al., "Direct patterning of self-assembled nanocrystal monolayers by electron beams", *APPLIED PHYSICS LETTERS*, **78**, 1915-1917, 2001.

116. S. Tokito, et al., "Confinement of triplet energy on phosphorescent molecules for highly-efficient organic blue-light-emitting devices", *Applied Physics Letters*, **83**, 569-571, 2003.

117. C. Adachi, et al., "Endothermic energy transfer: A mechanism for generating very efficient high-energy phosphorescent emission in organic materials", *APPLIED PHYSICS LETTERS*, **79**, 2082-2084, 2001.

118. I. G. Hill and A. Kahn, "Organic semiconductor interfaces containing bathocuproine", *J. Appl. Phys.*, **86**, 4515-4519, 1999.

119. C. R. Kagan, et al., "Long-range resonance transfer of electronic excitations in close-packed CdSe quantum-dot solids", *Physical Review B*, **54**, 8633-8643, 1996.

120. V. Bulovic, et al., "Weak microcavity effects in organic light-emitting devices", *Physical Review B*, **58**, 3730-3740, 1998.

121. M. Baldo and S. Forrest, "Transient analysis of organic electrophosphorescence. I. Transient analysis of triplet energy transfer", *PHYSICAL REVIEW B*, **62**, 10958-10967, 2000.

122. M. Baldo, et al., "Transient analysis of organic electrophosphorescence. II. Transient analysis of triplet-triplet annihilation", *PHYSICAL REVIEW B*, **62**, 10967-10977, 2000.

123. H. Kuhn, "Classical Aspects of Energy Transfer in Molecular Systems", *J Chem Phys*, **53**, 101, 1970.

124. V. Bulovic, et al., "Bright, saturated, red-to-yellow organic light-emitting devices based on polarization-induced spectral shifts", *CHEM PHYS LETT*, **287**, 455-460, 1998.

125. M. Anni, et al., "Förster energy transfer from blue-emitting polymers to colloidal CdSe/ZnS core shell quantum dots", *Applied Physics Letters*, **85**, 4169-4171, 2004.

126. V. Bulovic, Ph.D. Thesis, Princeton University, 1998.

127. V. Klimov, et al., "Optical gain and stimulated emission in nanocrystal quantum dots", *SCIENCE*, **290**, 314-317, 2000.

128. R. Konenkamp, "Photoelectric Properties and Applications of Low-Mobility Semiconductors", Springer, 2000.

129. A. C. Arango, Master's Thesis, Massachusetts Institute of Technology, 2005.

130. N. C. Greenham, et al., "Angular Dependence of the Emission from a Conjugated Polymer Light-Emitting Diode: Implications for efficiency calculations", *Adv Mater*, **6**, 491-494, 1994.